

OPERANDO CHARACTERIZATION OF BATTERY
MATERIALS

A Dissertation

Presented to the Faculty of the Graduate School

of Cornell University

in Partial Fulfillment of the Requirements for the Degree of

Doctor of Philosophy

by

Xinran Feng

December 2021

© 2021 Xinran Feng

OPERANDO CHARACTERIZATION OF BATTERY MATERIALS

Xinran Feng, Ph.D.

Cornell University 2021

As the energy demand has grown exceptionally in the past several decades, the need to develop battery materials with higher energy and power density is on the table. To further push the capacity limit of next-generation battery material, a deeper insight into the reaction mechanisms and degradation processes is required. Operando characterization fills in this gap perfectly. It traces the behavior of active materials while the battery is running in its native environment, making it an excellent method to understand the origin of electrodes capacity and the cause of the deprivation.

The broad purpose of this dissertation work is to uncover the reaction mechanisms and degradation processes of the battery material, including both electrode and electrolytes, using operando methods such as the high-energy synchrotron X-ray techniques and differential electrochemical mass spectrometry (DEMS). Synchrotron X-ray diffraction and X-ray absorption spectroscopy have made it possible to study the atomic structure transformations and electrochemical reactions of the electrode materials in a non-destructive way. DEMS combines the electrochemical cell with a mass spectrometer, enabling concurrent data collection from both electrochemistry and corresponding gas evolution reactions. Three projects were discussed herein to

demonstrate the importance of operando characterization methods. First, the reaction pathways and activation reaction of Cu_2S anode in two electrolyte systems were investigated using operando X-ray and electrochemical techniques. Second, the interaction between the CoS_2 host and sulfur cathode in the lithium-sulfur battery was revealed by X-ray absorption spectroscopy. Finally, a coin cell-based DEMS cell was developed, allowing operando gas evolution analysis of lithium-ion batteries at room temperature and elevated temperature. These studies provide valuable insights into the degradation pathways of battery materials, facilitating the rational design of next-generation high-performance battery materials.

BIOGRAPHICAL SKETCH

Xinran Feng was born in Beijing, China. Growing up closely with her pharmacologist grandmother, she had a childhood filled with fascinating and colorful chemistry experiments. After completing high school in 2010 in Beijing, she moved to the United State and attended the Pennsylvania State University-University Park campus. She selected the chemistry major in the first semester because of the amazing memories she had with her grandmother, and her strong interest in science, which started to grow when she was a little girl.

Halfway through her undergraduate study, she decided to work with Prof. Dan Sykes, in area of analytical chemistry. During undergraduate research, she successfully developed new HPLC stationary phases designed to evaluate the separation of explosives and drug residues.

After graduated from Penn State, she spent a year in Baltimore, working in a water chemistry company, before attending graduate school at Cornell University. Since joining Cornell University, she was benefited tremendously from the interaction with Professors Héctor Abruña, Frank DiSalvo, and Joel Brock, as well as the great researcher in the community.

The majority of her Ph.D. work has been focused on using operando characterization methods to investigate various lithium-based battery material. Outside the lab, Xinran

enjoys visiting museums and art galleries around the country, and spending time with friends.

Dedicated to my Mom, Dad, and Paternal Grandmother

ACKNOWLEDGEMENTS

There are several people without whom the work presented in this dissertation would not be possible. I would like to thank:

- Prof. Abruña for allowing me to join his group and continues supports he provided in the past six years.
- My committee members, Profs. Brock and DiSalvo, for the intellectual discussions
- Prof. Phillip Milner for being the proxy for prof. DiSalvo and attending my B-exam.
- Drs. Jacob Ruff, Rong Huang, Ken Finkelstein, and Chris Pollock for beamline support at CHESS;
- Dr. Hongsen Wang for helping me get start on the DEMS project
- Dr. Katie and James Pastore for teaching me run experiments at the synchrotron.
- My collaborators on the Cu₂S project, Prof. Peng Zhang, and Dr. Yunhui Wang.
- All the Abruña group members and Alumni

TABLE OF CONTENTS

ABSTRACT	ii
BIOGRAPHICAL SKETCH.....	iv
ACKNOWLEDGEMENTS	vii
TABLE OF CONTENTS	viii
TABLE OF FIGURES	xi
TABLE OF TABLES	xix
CHAPTER 1	1
INTRODUCTION TO DISSERTATION	1
1-1. Motivation for Lithium-Ion Battery Research:	1
1.2. State of Art Battery Materials.....	3
1.2.1 Layered transition metal oxide cathodes	3
1.2.2 Sulfur cathode material.....	5
1.2.3 Graphite and silicon anode materials	7
1-3. Operando Characterization Methods.....	8
1-4. Dissertation Overview.....	9
CHAPTER 2.....	13
EXPERIMENTAL METHODS	13
2-1. Introduction	13
2-2 Coin cell battery	13
2-2-1. Battery electrode preparation.....	13
2-2-2. Battery Coin Cell Assembly and in-situ cell modification	14
2-3. Battery electrochemical measurement	16
2-4. Synchrotron X-ray Absorption Spectroscopy	16
2-5. Operando X-ray diffraction measurements	17
2-6. Differential Electrochemical Mass Spectrometry	20
2-6-1. Design of coin cell battery-based DEMS electrochemical cell:	20
CHAPTER 3.....	23
AN INNOVATIVE LITHIUM-ION BATTERY SYSTEM BASED ON A Cu_2S	
ANODE MATERIAL	23
3-1. Introduction	23
3-2. Experimental Section	27
3-2-1 Materials	27

3-2-2 Preparation of Cu ₂ S/C and Cu ₂ S.....	27
3-2-3 Physical characterization	28
3-2-4 Electrochemical measurements.....	28
3-2-5 <i>Operando</i> X-ray absorption spectroscopy measurements	30
3-2-6 <i>Operando</i> X-ray diffraction measurements	30
3-3. Results and Discussions	32
3-3-1 Physical properties and electrochemical performances of Cu ₂ S/C	32
3-3-2 <i>Operando</i> XAS investigation of the Cu ₂ S mechanism in ether-/carbonate-based electrolytes.....	44
3-3-3 Evolution in the crystal structure of Cu ₂ S in DOL/DEM and EC/DEC electrolytes.....	57
3-3-4 Structural evolution and activation processes of Cu ₂ S/C in EC/DEC electrolyte	69
3-3-5 Electrochemical performance of a (-) Cu ₂ S/C 1 M LiPF ₆ in EC/DEC LiCoO ₂ (+) pouch cell	77
3-4. Conclusions	79
CHAPTER 4.....	86
AN OPERANDO X-RAY ABSORPTION SPECTROMETRY STUDY OF THE INTERACTION BETWEEN CO ₂ HOST AND SULFUR CATHODE IN LITHIUM-SULFUR BATTERIES	86
4-1 Introduction	86
4-2 Experimental Methods	88
4-2-1. Li-S battery preparation with MOF-derived CoS ₂ /S composite.....	88
4-2-2. Electrochemical methods.....	88
4-2-3. <i>Operando</i> X-ray absorption spectroscopy measurements.....	89
4-3. Results And Discussion.....	90
4-4 Conclusions	99
CHAPTER 5	102
A COIN-CELL BASED DIFFERENTIAL ELECTROCHEMICAL MASS SPECTROMETRY (DEMS) CELL FOR GAS GENERATION EVALUATION OF LITHIUM-ION BATTERIES	102
5-1. Introduction	102
5-2. Experimental Section	105
5-2-1 Chemicals.....	105
5-2-2 Synthesis of LiNi _{0.6} Mn _{0.2} Co _{0.2} O ₂ (NMC622).....	105
5-2-3 Battery preparation	106

5-2-4 Differential Electrochemical Mass Spectrometry	106
5-2-5. The design of coin cell battery-based DEMS electrochemical cell	107
5-2-6 Design of DEMS modified coin cell case.....	108
5-2-7 Electrochemical measurements:	110
5-3. Results and Discussion.....	110
5-3-1. Choice of electrode materials	110
5-3-2. Gas evolution at room temperature.....	116
5-3-4. Gas evolution at elevated temperature.....	130
5-4. Conclusions	139
CHAPTER 6.....	148
CONCLUSIONS AND FUTURE OUTLOOK.....	148
6-1. Overview	148
6-2. Future Research Directions	148

TABLE OF FIGURES

Figure 1-1, The total US greenhouse gas emissions by economic sector in 2019.	2
Figure 1-2. Outlook for annual global passenger car and light-duty vehicle sales, to 2030.	3
Figure 1-3. A schematic diagram of a rechargeable lithium-ion battery. The pale blue background is a representation of liquid electrolyte.....	5
Figure 2-1 Schematic diagram of an operando coin cell for synchrotron X-ray measurements.	15
Figure 2-2. Flowchart of XRD data workup	19
Figure 2-3 Schematic diagram of coin cell-based DEMS holder.....	21
Figure 3-1 Schematic illustration of the Cu ₂ S/C composite synthesis procedure.	33
Figure 3-3. (a) TEM and (b) HR-TEM images of the Cu ₂ S/C composite.....	34
Figure 3-4. XRD patterns of Cu ₂ S, Cu ₂ S/C composite, and Cu ₂ S reference	35
Figure 3-5. (a), (b) SEM images, (c) TEM and (d) HRTEM images of Cu ₂ S.	36
Figure 3-6. Raman spectra of Cu ₂ S and Cu ₂ S/C	37
Figure 3-7. TGA weight loss profile of Cu ₂ S/C.	38
Figure 3-8. Cycling performances of Cu ₂ S and Cu ₂ S/C in EC/DEC at 200 mA/g. The specific capacity of Cu ₂ S/C was calculated based on the mass of the Cu ₂ S/C composite.....	39
Figure 3-9 Coulombic efficiency of Cu ₂ S and Cu ₂ S/C in EC/DEC at 200 mA/g.....	40
Figure 3-10. Cycling performances of Cu ₂ S and Cu ₂ S/C in DOL/DME at 200 mA/g.	41
Figure 3-11. Charge and discharge profiles of Cu ₂ S in (a) DOL/DME and (b) EC/DEC electrolytes, Cu ₂ S/C in (c) DOL/DME and (d) EC/DEC electrolytes at 200 mA g ⁻¹ .	

The specific capacity of Cu₂S/C was calculated based on the mass of the Cu₂S/C composite..... 42

Figure 3-12. Long-term cycling performance of Cu₂S/C in EC/DEC at 20 mA g⁻¹. The specific capacity of Cu₂S/C was calculated based on the mass of the Cu₂S/C composite..... 43

Figure 3-13. Cu K-edge XANES powder spectra of c-Cu₂O, c-Cu₂S, Cu₂S, and Cu₂S/C 44

Figure 3-14 XANES patterns of Cu₂S discharge in DOL/DME 46

Figure 3-15 XANES patterns of Cu₂S discharge in DOL/DME 47

Figure 3-16. Charge/discharge profile of Cu₂S in DOL/DME..... 47

Figure 3-17 XANES patterns of Cu₂S discharge in EC/DEC 48

Figure 3-18 XANES patterns of Cu₂S charge in EC/DEC..... 48

Figure 3-19. Charge/discharge profile of Cu₂S in EC/DEC..... 49

Figure 3-20 EXAFS patterns of Cu₂S discharge in DOL/DME..... 49

Figure 3-21 EXAFS patterns of Cu₂S charge in DOL/DME 50

Figure 3-22 EXAFS patterns of Cu₂S discharge in EC/DEC..... 50

Figure 3-23 EXAFS patterns of Cu₂S charge in EC/DEC 51

Figure 3-24 (a) EXAFS spectra of Cu K-edge for pristine sample scan and (b) fully discharged scan with the corresponding fit and fitting window in DOL/DME electrolyte. 52

Figure 3-25. Charge/discharge profile of Cu₂S in DOL/DME and the percent of Cu₂S reacted at the selected states of charge. 54

Figure 3-26. Charge/discharge profile of Cu ₂ S in EC/DEC and the percent of Cu ₂ S reacted at the selected states of charge.	55
Figure 3-27. TEM and HR-TEM images of Cu ₂ S in (a, b) DOL/DME and (c, d) EC/DEC electrolytes after 10 cycles.	56
Figure 3-28. <i>Operando</i> XRD measurements and corresponding initial (dis)charge curves of Cu ₂ S in DOL/DME 1M LiPF ₆ at 0.2 C. (a) contour plot, and (b) waterfall Plot.....	58
Figure 3-29. Standard patterns of Cu ₂ S (PDF 00-003-1071), Cu _{1.96} S (PDF 00-012-0224), Li ₂ S (PDF 01-077-2145) and Cu.....	59
Figure 3-30. Rietveld refinement of the fully recharged copper sulfide in DOL/DME electrolyte. The XRD pattern was taken at an incident energy of 19.82 keV ($\lambda = 0.6246 \text{ \AA}$).....	60
Figure 3-31. Waterfall operando XRD plots of Cu ₂ S in the 10th cycle in DOL/DME: (a)discharge and (b) charge processes.....	61
Figure 3-32. <i>Operando</i> XRD measurements and corresponding initial (dis)charge curves of Cu ₂ S in DOL/DME 1M LiPF ₆ at 0.2 C. (a) contour plot, and (b) waterfall plot.....	63
Figure 3-33. Waterfall operando XRD plots of Cu ₂ S in the 2nd cycle in EC/DEC: (a) discharge and (b) charge processes.	64
Figure 3-34. XRD pattern of the Cu ₂ S electrode from the 'dead' cell (after 10 cycles, fully charged to 3V, EC/DEC electrolyte).	64
Figure 3-35. <i>In situ</i> EIS measurements and the corresponding (dis)charge profiles of Cu ₂ S in (a-c) the 1st and (d-f) the 10 th cycle in DOL/DME.....	66

Figure 3-36. <i>In situ</i> EIS measurements and the corresponding (dis)charge profiles of Cu ₂ S in (a-c) the 1st and (d) the 10th cycle in EC/DEC.	67
Figure 3-36. <i>Operando</i> XRD measurements and corresponding (dis)charge curves of Cu ₂ S/C in the (a) 1st cycle and (b) 10th cycle in EC/DEC electrolytes with 1M LiPF ₆	69
Figure 3-37. <i>Operando</i> XRD of Cu ₂ S/C in (a)the 1st and (b) the 10th cycle in the EC/DEC electrolyte.	70
Figure 3-38. <i>Operando</i> XANES spectra of Cu ₂ S/C (a) discharge and (b) charge in EC/DEC.	71
Figure 3-39. <i>Operando</i> EXAFS spectra of Cu ₂ S/C (a) discharge and (b) charge in EC/DEC.	71
Figure 3-40. Charge/discharge profile of Cu ₂ S/C in EC/DEC.	72
Figure 3-41. TEM images of Cu ₂ S/C (a) before cycling, (c) after cycling, and (c) corresponding schematic.	73
Figure 3-42. CV profiles of Cu ₂ S/C in EC/DEC.	74
Figure 3-43. <i>In situ</i> EIS measurements and the corresponding (dis)charge profiles of Cu ₂ S/C in (a-c) the 1st and (d-f) the 10th cycle in DOL/DME.	75
Figure 3-45. <i>In situ</i> EIS measurements and the corresponding (dis)charge profiles of Cu ₂ S/C in (a-c) the 1st and (d-f) the 10th cycle in EC/DEC.	76
Figure 3-46. (a) Charge and discharge profiles and (b) cycling performance of the LiCoO ₂ -Cu ₂ S/C full cell at 100 mA g ⁻¹ (the capacity was calculated based on the mass of Cu ₂ S).	77

Figure 4-1. The 1st charge/discharge profile fo the pristine cell. XAS spectra used in the EXAFS analysis were chosen at the stated state of charge. 90

Figure 4-2, EXAFS profile and fitting results for S/Z-CoO₂ electrode in the pristine state. The fitting was performed within a Hanning window between 1.25 and 4.8 Å. 92

Figure 4-3. Crystal structure of CoS₂. The theoretical atomic distances between the core Co atom and its neighboring atom are listed next to the corresponding bonds.... 93

Figure 4-4. Changes in atomic distances between core Co atom and the specified neighboring atom at different states of charge. 94

Figure 4-5, (a) Cycling performance of S/Z-CoS₂, S/H-CoS₂, and S/ZIF-67 at 0.2 C for 200 cycles. (b) Long-term cycling of S/Z-CoS₂, S/H-CoS₂, and S/ZIF-67 at 1 C for 1000 cycles 95

Figure 4-6. The 5th charge/discharge profile from the S/Z-CoS₂ cell. XAS spectra used in the EXAFS analysis were chosen at the stated state of charge..... 96

Figure 4-7. The changes in atomic distances between the core Co atom and the specified neighboring atoms, at different states of charge after 5 cycles at 0.1C. 96

Figure 4-8. XANES spectra of the MOF-CoS₂/S cell at Co k-edge, at the pristine state, after 5 cycles and after 50 cycles..... 98

Figure 5-1. Schematic diagram of the coin cell-based DEMS measurement cell. The cell was placed in an argon environment. For measurements at 45°C, a heating tape was used to wrap the cell, and a voltage controller was used to control the temperature. 108

Figure 5-2. (a) Schematic diagram of the modified coin cell cathode case. (b) Diagram of cell components in the DEMS coin cell. 109

Figure 5-3. Picture of the DEMS coin cell cathode case.....	110
Figure 5-4. XRD pattern of the synthesized NMC 622 cathode and the corresponding reference	112
Figure 5-5. SEM image of the synthesized NMC622 particles with a size distribution of 0.2-0.5 μm size.....	112
Figure 5-6. Decomposition mechanism of DEC in lithium-ion batteries.....	113
Figure 5-7. Decomposition mechanism of EC in lithium-ion batteries.....	113
Figure 5-8. Decomposition mechanism of linear carbonate catalyzed by lithium titanate.	115
Figure 5-9. CV profile of LiCoO_2 measured using a coin cell-based DEMS cell. The cell voltage was scanned from 3V to 5V at a scan rate of 0.5mV/s.	117
Figure 5-10. CV profile of NMC 622 measured using a coin cell-based DEMS cell. The cell was scanned from 3V to 5V at a scan rate of 0.5mV/s.....	118
Figure 5-11. Hydrogen evolution data for LiCoO_2 electrode in 1 M LiPF_6 EC/DEC at a scan rate of 0.5 mV/s.....	119
Figure 5-12. Hydrogen evolution data for NMC622 electrode in 1 M LiPF_6 EC/DEC at a scan rate of 0.5 mV/s.	119
Figure 5-13. Reaction mechanisms of EC decomposition occurring at the anode.....	120
Figure 5-14. CO_2 evolution data for a LiCoO_2 electrode in 1 M LiPF_6 EC/DEC at a scan rate of 0.5 mV/s.....	121
Figure 5-15. CO_2 evolution data for NMC622 electrode in 1 M LiPF_6 EC/DEC at a scan rate of 0.5 mV/s.....	122

Figure 5-16. O ₂ evolution data for LiCoO ₂ electrode in 1 M LiPF ₆ EC/DEC at a scan rate of 0.5 mV/s.	123
Figure 5-17. O ₂ evolution data for NMC622 electrode in 1 M LiPF ₆ EC/DEC at a scan rate of 0.5 mV/s.	124
Figure 5-18. Ethylene evolution data for LiCoO ₂ electrode in 1 M LiPF ₆ EC/DEC at a scan rate of 0.5 mV/s.	124
Figure 5-19. Ethylene evolution data for NMC622 electrode in 1 M LiPF ₆ EC/DEC at a scan rate of 0.5 mV/s.	125
Figure 5-20. CV profile from Li ₄ Ti ₅ O ₁₂ measured using a coin cell-based DEMS cell. The cell was scanned from 3V to 0.2V with a scan rate of 0.5mV/s.	126
Figure 5-21. Hydrogen evolution data for Li ₄ Ti ₅ O ₁₂ electrode in 1 M LiPF ₆ EC/DEC at a scan rate of 0.5 mV/s.	127
Figure 5-22. Ethylene evolution data for Li ₄ Ti ₅ O ₁₂ electrode in 1 M LiPF ₆ EC/DEC at a scan rate of 0.5 mV/s.	128
Figure 5-23. CO evolution data for Li ₄ Ti ₅ O ₁₂ electrode in 1 M LiPF ₆ EC/DEC at a scan rate of 0.5 mV/s.	129
Figure 5-24. CV profile of LiCoO ₂ measured using a coin cell-based DEMS cell. The cell was scanned from 3V to 5V with a scan rate of 0.5mV/s at a temperature of 45°C.	130
Figure 5-25. CV profile from NMC measured using a coin cell-based DEMS cell. The cell was scanned from 3V to 5V with a scan rate of 0.5mV/s, at a temperature of 45°C	131

Figure 5-26. Hydrogen evolution data for LiCoO ₂ electrode in 1 M LiPF ₆ EC/DEC at a scan rate of 0.5 mV/s, at a temperature of 45°C	132
Figure 5-27. Hydrogen evolution data for NMC622 electrode in 1 M LiPF ₆ EC/DEC at a scan rate of 0.5 mV/s, at a temperature of 45°C	132
Figure 5-28. Ethylene evolution data for LiCoO ₂ electrode in 1 M LiPF ₆ EC/DEC at a scan rate of 0.5 mV/s, at a temperature of 45°C	134
Figure 5-29. Ethylene evolution data for NMC622 electrode in 1 M LiPF ₆ EC/DEC at a scan rate of 0.5 mV/s, at a temperature of 45°C	135
Figure 5-30. Oxygen evolution data for LiCoO ₂ electrode in 1 M LiPF ₆ EC/DEC at a scan rate of 0.5 mV/s, at a temperature of 45°C	136
Figure 5-31. oxygen evolution data for NMC622 electrode in 1 M LiPF ₆ EC/DEC at a scan rate of 0.5 mV/s, at a temperature of 45°C	137
Figure 5-32. CO ₂ evolution data for LiCoO ₂ electrode in 1 M LiPF ₆ EC/DEC at a scan rate of 0.5 mV/s, at a temperature of 45°C	137
Figure 5-33. CO ₂ evolution data for NMC622 electrode in 1 M LiPF ₆ EC/DEC at a scan rate of 0.5 mV/s, at a temperature of 45°C	138

TABLE OF TABLES

Table 3-1. EXAFS fitting results of the pristine and fully discharged Cu ₂ S in DOL/DME electrolyte	52
Table 3-2. Apparent Li ⁺ diffusion coefficients (D _{Li+}) of Cu ₂ S calculated from EIS (at fully charged state).	67
Table 4-1. EXAFS fitting results of the pristine MOF-CoS ₂ /S in DOL/DME electrolyte	93

CHAPTER 1

INTRODUCTION TO DISSERTATION

1-1. Motivation for Lithium-Ion Battery Research:

Our world has been experiencing a dangerous level of climate change in the past few decades. According to climate central, an independent organization of environment researchers and journalists, the concentration of CO₂ in the atmosphere has increased by almost a third, rising from 290 ppm to 410 ppm, since the late 19th century.

Moreover, in 2019, the methane and nitrous oxide levels in the atmosphere reached historical highs at 1866 ppm and 332 ppm, respectively. It is evident that human activities unambiguously contribute the majority of this observed increase in greenhouse gas concentrations.

Summarized by the United States Environmental Protection Agency in 2019, 29% of the greenhouse gas emissions in the US are from transportation, followed by electricity production (25%), industry (23%), commercial and residential (13%), and agriculture (10%). ¹(Fig. 1-1). Among all the greenhouse gas emission sources, fossil fuels represent the majority, accounting for over 90% of transportation emissions and 62% of electricity production. Thus, a global energy transition from burning fossil fuels to renewable energies is urgently needed to reduce greenhouse gas emissions and alleviate/mitigate the current climate change situation.

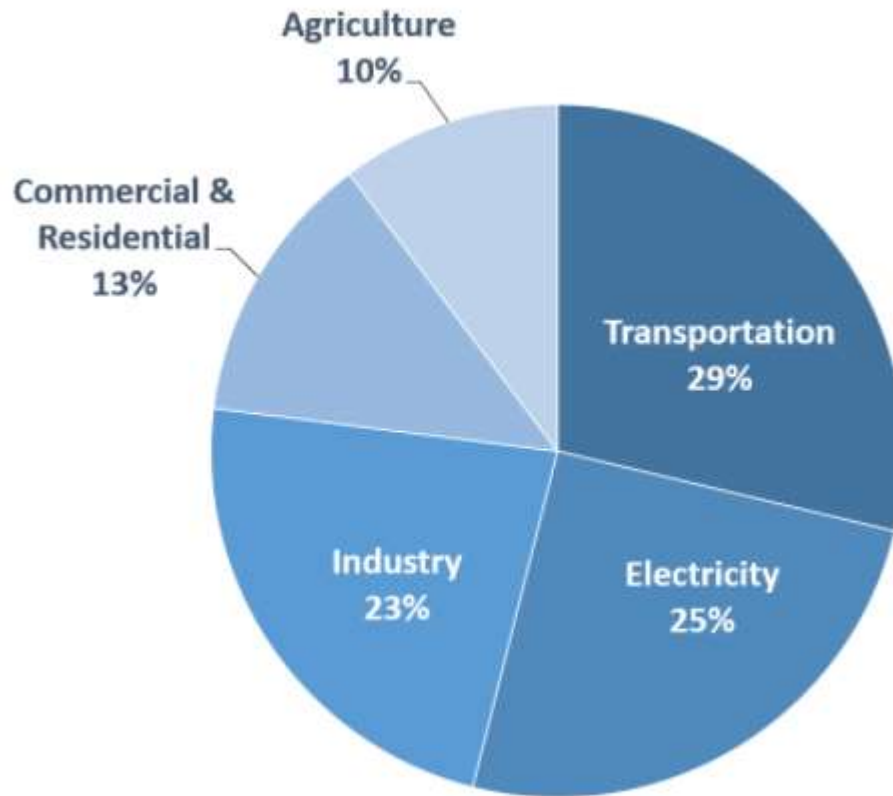
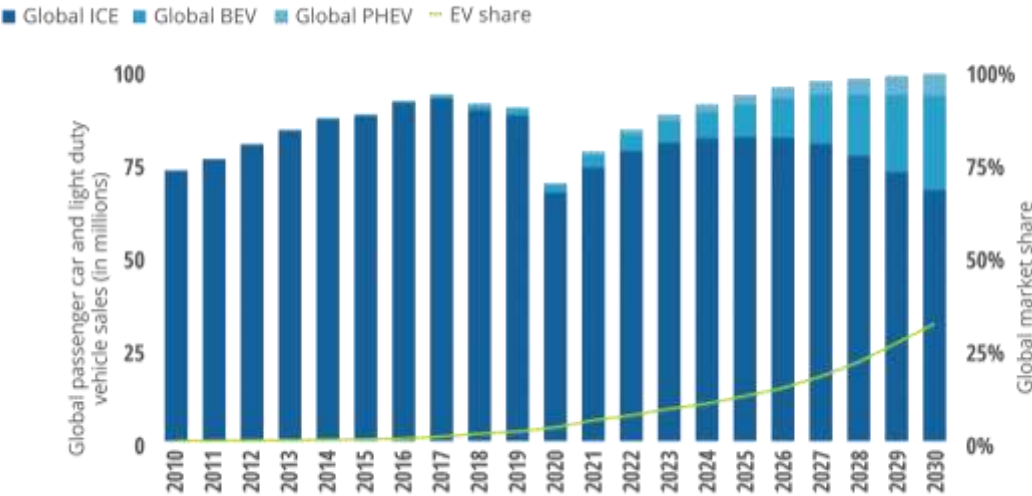


Figure 1-1, The total US greenhouse gas emissions by economic sector in 2019. ¹

Lithium-ion batteries, being one of the most versatile and reliable energy storage devices and the top choices to power electric vehicles (EVs), are a key contributor to the decarbonization of the transportation and electricity sectors. In 2019, battery-based electric cars represented about 2.5% of the total automobile market share. This number is expected to grow to 32% in 2030 as predicted by Deloitte. (Figure 1-2). ² Overall, battery electric vehicles (BEVs) will take 81% of the total EVs sales (25.3 million) and plug-in hybrid electric vehicles (PHEVs) will take the rest 19% (5.8 million). This increasing demand for electric vehicles also puts pressure on battery scientists to

develop battery materials with higher capacity and energy density, better cyclability, and higher safety standards.

Outlook for annual global passenger-car and light-duty vehicle sales, to 2030



Source: Deloitte analysis, IHS Markit, EV-Volumes.com¹⁶

Figure 1-2. Outlook for annual global passenger car and light-duty vehicle sales, to 2030. ²

1.2. State of Art Battery Materials

1.2.1 Layered transition metal oxide cathodes

A typical rechargeable lithium-ion battery consists of a cathode and an anode separated by a separator and electrolyte. A schematic diagram of a lithium-ion battery system is shown in Figure 1-3. Due to its high energy and power density, the lithium-ion battery has become the top candidate in EVs. Currently, layered lithium transition metal oxides are the most widely used high-capacity cathode materials in all battery based EVs and most of the portable electronic applications. Among all the electrode

materials previously investigated, lithium cobalt oxide (LiCoO_2 , LCO) is the most commercially successful model and has dominated the battery market for three decades. LCO has a theoretical capacity of 274 mAh/g. However, the capacity of LCO cannot be fully accessed (~ 150 mAh/g in practical devices). At a potential above 4.2V, the capacity of LCO fades quickly due to its poor thermal and structural stability. To tackle this issue and accompany the demand for the extended driving range of electric vehicles, Mn, Ni, and Al have been introduced to the layered structure, enabling higher capacity and good cycling performance at 4.5 V or higher. Incorporating these elements into the structure can increase the material electrochemical capacity and thermal stability, and a practical capacity above 200 mAh/g can be achieved. Among these four elements, nickel contributes to the overall capacity by increasing the cutoff voltage, manganese and aluminum enhance the structural and thermal stability, and cobalt ensures the conductivity. In recent years, Ni-rich layered oxides NMC, $\text{LiNi}_{1-x-y}\text{Co}_x\text{Mn}_y\text{O}_2$ ($1-x-y>0.5$), have been gradually popularized in new EVs manufactured, and NCA ($\text{Li}_{1-x}\text{Ni}_{0.8}\text{Co}_{0.15}\text{Al}_{0.05}\text{O}_2$) is specially used in Tesla models or portable electronic devices from Panasonic and Sony. Researchers are continuing to investigate cathode materials with higher nickel contents. Up until now, NMC materials with over 95% nickel have been developed, achieving a practical capacity of 238mAh/g.³

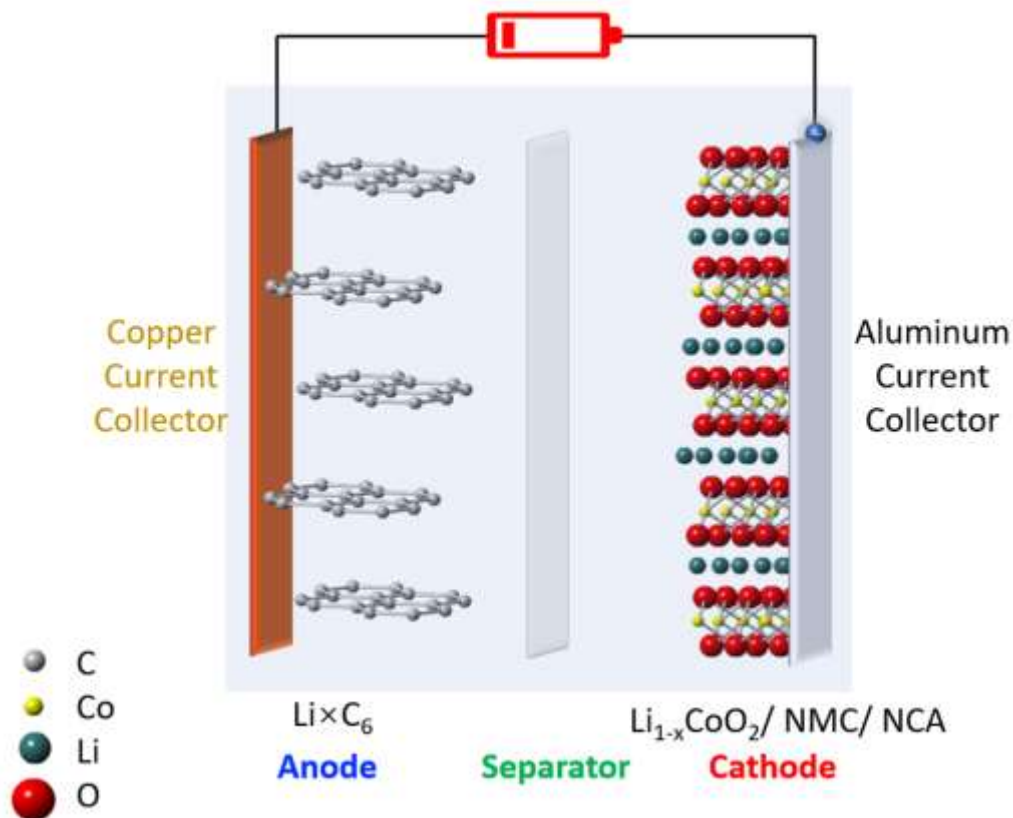


Figure 1-3. A schematic diagram of a rechargeable lithium-ion battery. The pale blue background is a representation of liquid electrolyte.

1.2.2 Sulfur cathode material

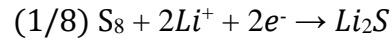
Exploring electrode materials beyond intercalation chemistry is another research direction to increase battery capacity. Sulfur is a great cathode candidate because of its 2600 Wh/kg power density, 1,675 mAh/g theoretical capacity, and financially friendly cost. Sulfur undergoes a conversion reaction during battery charge and discharge processes, as both structural and chemical changes are involved. This type of battery reaction provides much more capacity than a regular intercalation reaction, but it suffers from low cyclability due to its complex nature. Lithium sulfur (Li-S)

batteries use elemental sulfur as the cathode, and lithium metal as the anode. The redox reactions occurring during battery discharge are listed as follows:

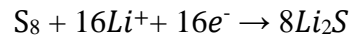
Anode:



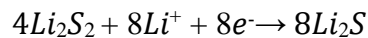
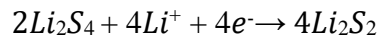
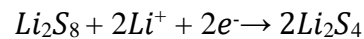
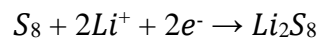
Cathode:



Overall reaction:



The current challenge of Li-S batteries is the low electronic conductivity of S and the lithium polysulfide shuttling effect. The sulfur eight-atom rings dissociate into lithium sulfide through a multiple-step reduction process when accepting lithium ions from the lithium anode. During this process, various lithium polysulfides species are formed as intermediates, as shown below.



These lithium polysulfides are prone to dissolve into the electrolyte solution, causing a loss of active material and decay in capacity. This phenomenon is called the lithium polysulfide shuttling effect. To alleviate the polysulfide dissolution phenomena, metal

oxides and sulfides are commonly used as the sulfur hosts in the cathode matrix. The polarity of these metal oxide/sulfide hosts has proven to reduce polysulfide dissolution through the polar-polar interaction. Moreover, host materials such as MnO_2 , TiO_2 , and FeS_2 have additional chemical interactions with lithium polysulfides.⁴⁻⁷ Thus, they bind to polysulfides more efficiently by forming intermediate complexes.

1.2.3 Graphite and silicon anode materials

Graphite has been the dominant lithium-ion battery anode material for the past 30 years. Its 2D layered structure and relatively weak van der Waals forces between each layer combine well with the layered transition metal oxide cathode materials, facilitate the lithium-ion diffusion during charging and discharging. It has a specific capacity of 372 mAh/g, higher than the common cathode materials and suitable for the current commercial lithium-ion battery systems. However, this capacity is relatively low to pair with conversion cathode materials (i.e. sulfur cathode) whose capacity is well over 1000 mAh/g. Graphite also has intrinsic limitations of low-rate capability and the irreversible capacity lost in the first cycle due to the side reactions with electrolytes and SEI (solid electrolyte interface) formation. Good alternatives to the graphite anode are silicon and metallic lithium.

Silicon has a theoretical capacity of 3578 mAh/g. It can be used either as a stand alone anode or as an additive to graphite anodes. By incorporating a small amount of silicon into the graphite anode matrix, the energy density of current LIBs can be increased by 10-20%.⁸ Another promising anode candidate is metallic lithium, which is considered

to be the ultimate anode that provides unlimited Li^+ and high capacity (3860 mAh/g). However, silicon suffers from severe volume changes while charging and discharging which lead to pulverization, and metallic lithium is severely hampered by dendrite formation. All of these issues limit their application in commercial lithium-ion batteries.

To design better performing electrode materials, a detailed understanding of the battery materials reaction mechanism is required. In this context operando studies enable characterization of the active materials, non-destructively under operating conditions.

1-3. Operando Characterization Methods

Operando is the Latin word for working. *Operando* characterization thus refers to the measurement of materials under actual working conditions. It eliminates the uncertainty caused by the post-treatment process, which is essential for battery materials, as the state of samples is highly affected by the applied voltage and is sensitive to air exposure. In my past six years at Cornell, performing operando characterization on energy storage and conversion materials has been the emphasis of my research work, taking advantage of the excellent research resources at Cornell.

The synchrotron lab at Cornell, The Cornell High Energy Synchrotron Source (CHESS), can generate high-energy, high intensity X-rays, with sub-angstrom wavelength, which can be used to interrogate the electrode electrochemical reactions

within lithium-ion batteries. By employing synchrotron X-ray absorption spectroscopy (XAS) and X-ray diffraction (XRD), the inorganic electrode phase transitions and reaction intermediates were tracked in real-time as the battery cycled, providing detailed insights into the working mechanisms of the materials

Differential electrochemical mass spectrometer (DEMS) is another powerful tool to track the reactions within a battery system. It combines an electrochemical cell (lithium-ion batteries) with a mass spectrometer and records the gas signals generated from electrochemical reactions. DEMS has been widely applied to analyze the gaseous volatile reaction intermediates generated from batteries, deciphering the decomposition mechanisms of electrolytes and electrodes. Using our unique battery cell design, gas evolutions from a lithium-ion battery could be precisely correlated with either electrode redox reactions, potential induced electrolyte decomposition, as well as temperature-related side reactions.

1-4. Dissertation Overview

The following chapters will cover various aspects of my graduate work:

- This chapter (Chapter 1) provides a brief introduction to the motivation of my graduate research and the current status of lithium-ion battery materials.
- Chapter 2 summarizes the experimental methods used throughout the dissertation, except noted otherwise.
- Chapter 3 presents a synchrotron X-ray study on the Cu_2S battery anode in two electrolyte systems.

- Chapter 4 presents the interactions between a CoS₂ host and lithium polysulfides using operando X-ray absorption spectroscopy.
- Chapter 5 describes a newly designed coin cell-based DEMS set-up that allows *operando* characterization of gas evolution from lithium-ion coin cells.
- Chapter 6 summarize the dissertation and proposes future research directions.

References

- (1) The United States Environmental Protection Agency. *Inventory of U.S. Greenhouse Gas Emissions and Sinks*; 2021.
- (2) Walton, B.; Hamilton, J.; Alberts, G.; Fullerton-Smith, S.; Day, E.; Ringrow, J. *Electric Vehicles: Setting a Course for 2030*; 2020.
- (3) Yoon, C. S.; Ryu, H.; Park, G.; Kim, J.; Kim, K.; Sun, Y. Extracting Maximum Capacity from Ni-Rich Li. **2018**, 4126–4132.
- (4) Liang, X.; Hart, C.; Pang, Q.; Garsuch, A.; Weiss, T.; Nazar, L. F. A Highly Efficient Polysulfide Mediator for Lithium–Sulfur Batteries. *Nature Communications* **2015**, *6*, 5682.
- (5) Seh, Z. W.; Li, W.; Cha, J. J.; Zheng, G.; Yang, Y.; McDowell, M. T.; Hsu, P. C.; Cui, Y. Sulphur-TiO₂ Yolk-Shell Nanoarchitecture with Internal Void Space for Long-Cycle Lithium-Sulphur Batteries. *Nature Communications* **2013**, *4*.
- (6) He, X.; Hou, H.; Yuan, X.; Huang, L.; Hu, J.; Liu, B.; Xu, J.; Xie, J.; Yang, J.; Liang, S.; Wu, X. Electrocatalytic Activity of Lithium Polysulfides Adsorbed into Porous TiO₂ Coated MWCNTs Hybrid Structure for Lithium-Sulfur Batteries. *Scientific Reports* **2017**, *7* (January), 1–9.
- (7) Mwizerwa, J. P.; Zhang, Q.; Han, F.; Wan, H.; Cai, L.; Wang, C.; Yao, X. Sulfur-Embedded FeS₂ as a High-Performance Cathode for Room Temperature All-Solid-State Lithium-Sulfur Batteries. *ACS Applied Materials and Interfaces* **2020**, *12* (16), 18519–18525.
- (8) Asenbauer, J.; Eisenmann, T.; Kuenzel, M.; Kazzazi, A.; Chen, Z.; Bresser, D. The Success Story of Graphite as a Lithium-Ion Anode Material-Fundamentals,

Remaining Challenges, and Recent Developments Including Silicon (Oxide)
Composites. *Sustainable Energy and Fuels* **2020**, 4 (11), 5387–5416.

CHAPTER 2

EXPERIMENTAL METHODS

2-1. Introduction

This chapter describes the general experimental procedures, apparatus, and instrumentation used in the experiments. In the first section, the battery electrode and cell preparation protocol are described. The second section details the standard electrochemical testing methods and procedures. The third section describes the operando X-ray scattering/absorption apparatus and testing methods. And the last section presents the differential electrochemical mass spectrometer battery cell design

2-2 Coin cell battery

2-2-1. Battery electrode preparation

In general, a battery electrode is prepared by tape casting the electrode slurry on a current collector using a doctor blade. The electrode slurry is prepared by first weighing out the electrode material, activated carbon, and binder in the desired ratio and finely ground with a mortar and pestle. N-Methyl-2-pyrrolidone was added dropwise into the mortar and evenly mixed with the powder. The solid to liquid ratio was generally kept at 50 mg solid to 1 ml liquid. The cast film was then transferred into a vacuum oven at 70 C for 1 hr and at 120 C overnight. Copper foil was used as the current collector for the cathode, and aluminum foil was used for the anode.

2-2-2. Battery Coin Cell Assembly and in-situ cell modification

All battery testing in this dissertation was conducted using the CR2032 coin cell. Each coin cell consists of a cathode case, an anode case, a separator (diameter, ϕ , 3/4 inch), a spacer, a spring, and two electrodes (ϕ 1/2 inch). In-situ battery cells for X-ray measurements were prepared by drilling holes (ϕ 3mm) in the center of the coin cell casings and sealing with a 0.05'' thick Kapton disk (ϕ 0.5 inch) on the outer side. Epoxy (Torr Seal) was evenly distributed around the hole with flat tip needles, and the Kapton disk was then pressed on top, uniformly covering the entire cofacial area. The finished coin cell casings were then dried overnight before use. Either nickel foams or springs were used as spacers in cell assembly. A schematic diagram is presented in Fig 2-1. Battery cells were prepared with either 40 μ L (Copper(I) sulfide and lithium-sulfur battery) or 200 μ L (differential electrochemical mass spectrometry) electrolyte solutions. Half the amount of electrolyte was dropped on the working electrode and the other half on the separator. All experiments with coin cells were performed with either 1 M lithium hexafluorophosphate (LiPF_6) dissolved in a 1:1 mixture of ethylene carbonate (EC) and diethyl carbonate (DEC), or 1 M lithium bis(trifluoromethanesulfon)imide (LiTFSI) dissolved in a 1:1 mixture of 1,3-dioxolane (DOL) and dimethyl ether (DME).

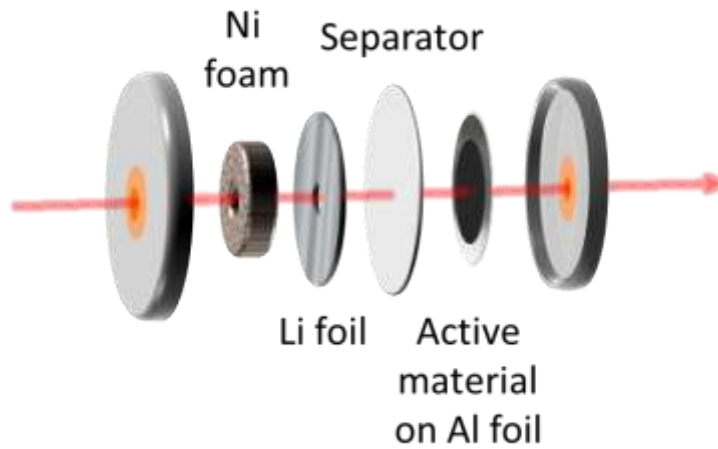


Figure 2-1 Schematic diagram of an operando coin cell for synchrotron X-ray measurements.

During operando X-ray measurements, the operando cell was placed in a holder made by two aluminum disks pressed against the anode and cathode casing, secured in a Teflon body.

2-3. Battery electrochemical measurement

1. Galvanostatic cycling. Galvanostatic charge-discharge measurements conducted in this work were done in CR 2032 coin cells, using either an Arbin battery test system and/or Neware battery testers. A constant current density, calculated from the electrode loading, was applied to the battery during measurements. The potential response (versus Li/Li⁺) from the applied current was recorded as a function of time. Potential windows were imposed specifically to each battery system to fully encompass all electrochemical reactions while preventing deleterious side reactions.
2. Cyclic voltammetry. Cyclic voltammetry (CV) was conducted using a Biologic potentiostat and/or an EG&G Princeton Applied Research potentiostat. The CVs presented in this work were measured using CR 2032 coin cells. A constant potential scan rate was applied, and the response current was collected.
3. Electrochemical impedance spectroscopy: Electrochemical impedance spectra (EIS) over the frequency range from 100 kHz, and 100 mHz at different states of charge were measured with a Biologic SP-150 potentiostat.

2-4. Synchrotron X-ray Absorption Spectroscopy

X-ray absorption spectroscopy (XAS) data collection was performed at beamline F-3 of the Cornell High Energy Synchrotron Source (CHESS). In a typical battery XAS measurement, the spectrum was collected in transmission mode from 150 eV below the

corresponding metal K-edge to 550 eV above the edge with N₂-filled ion chambers. An energy step of 5 eV was applied 20 eV before the edge energy, followed by a step size of 0.5 eV until 30 eV past the edge, and 50 eV after 30 eV past the edge energy. A metal foil spectrum was collected simultaneously to calibrate the incident X-ray energy and served as a reference spectrum. XANES (X-ray Absorption Near-Edge Structure) spectra were calibrated and normalized with the ATHENA software package. Fourier transformed EXAFS (Extended X-ray Absorption Fine Structure) spectra were obtained by applying a Hanning window from 3 to 12 Å⁻¹ with k²-weighting in ATHENA and fitted with standard path calculated using the ARTEMIS package.¹

2-5. Operando X-ray diffraction measurements

Operando powder X-ray Diffraction (XRD) patterns were collected at beamline A-1 of the Cornell High Energy Synchrotron Source (CHESS) at an incident energy of 19.82 keV ($\lambda = 0.6246 \text{ \AA}$) using an ADSC Quantum-210 CCD detector. A dark current correction was applied to the collected 2D XRD patterns. A baseline diffraction pattern (snapshot) was collected for an empty operational coin cell containing all parts, except for the working electrode slurry, to determine peaks from cell components and impurities. This background diffraction pattern was subtracted from the operando patterns during data analysis. The Kapton film and epoxy have minimal contributions to the diffracted signal. Each sample was exposed to the X-ray beam for 40 s every 4 mins to minimize potential beam-induced damage. A dark image was also collected after each X-ray exposure and later on subtracted from the sample snapshot to eliminate image hangover from the detector. The obtained operando 2D XRD snapshots were

reduced to 1D diffraction patterns by azimuthal integration using the GSAS-II software package.² To facilitate interpretation of the resulting 1D XRD patterns, the radial coordinate (representing the modulus of the X-ray momentum transfer) was converted to the 2θ scattering angle corresponding to the wavelength $\lambda = 1.05406 \text{ \AA}$ of the commonly used Cu $K\alpha$ X-ray source. The processed 1D XRD patterns were plotted against applied potential in the form of a contour plot.

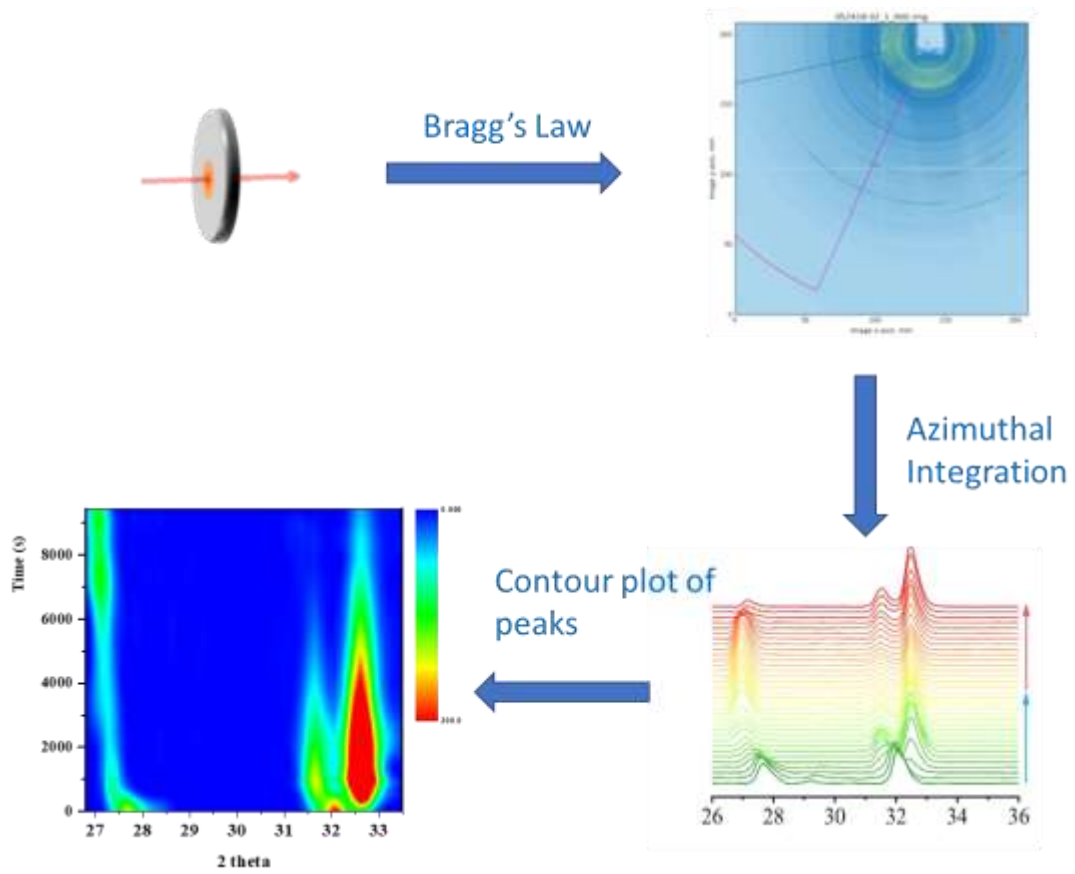


Figure 2-2. Flowchart of XRD data workup

2-6. Differential Electrochemical Mass Spectrometry

A differential electrochemical mass spectroscopy system with a quadrupole mass spectrometer, two differentially pumped chambers, an RF generator, a controller, and a secondary electron multiplier SEM detector was used in this work. The primary mass spectrometer analysis chambers were pumped by two individually controlled turbopumps, to which a rotary vane vacuum pump was attached as a backup vacuum system.

2-6-1. Design of coin cell battery-based DEMS electrochemical cell:

The detailed cell design is described in Chapter 5. Briefly, the DEMS coin cell design was inspired by the operando X-ray coin cell. Unlike X-ray cells, the DEMS cell has a hole only on the cathode casing, filled with nickel foam as a mechanical support and a porous Teflon film.

The coin cell battery-based DEMS cell holder consisted of a Kel-F (Polychlorotrifluoroethylene) top, a rubber gasket, two layers of Teflon film, and one layer of FEP film and a stainless-steel base with a frit. Two pieces of copper tape were used as the current collectors. The entire setup was placed under an argon environment and allowed to rest for 1 hour before each DEMS experiment. In the case of elevated temperature measurements, a heating belt and a voltage controller were used to adjust the temperature.

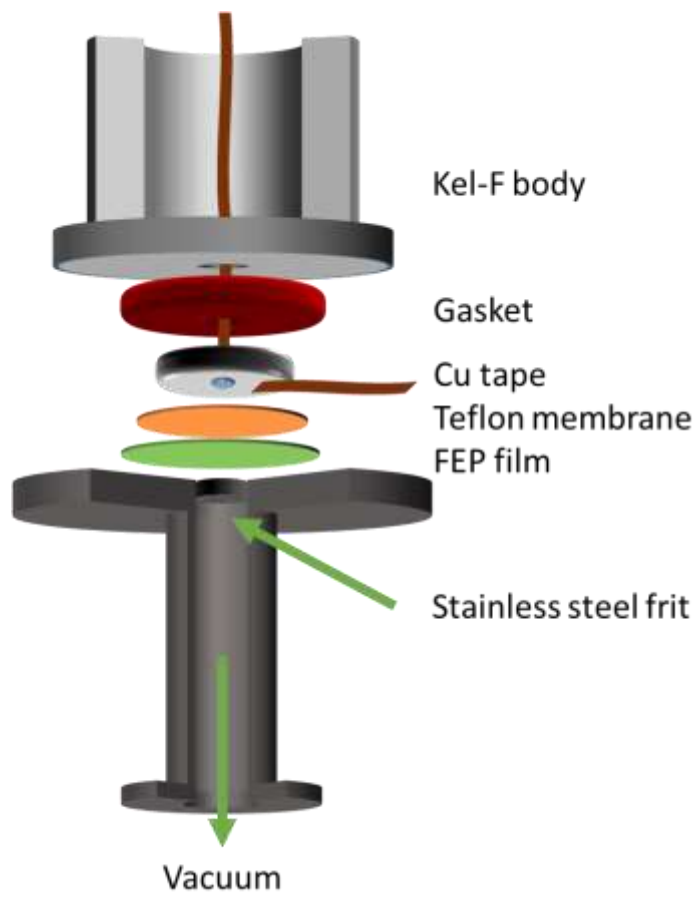


Figure 2-3 Schematic diagram of coin cell-based DEMS holder

References

- (1) Ravel, B.; Newville, M. ATHENA, ARTEMIS, HEPHAESTUS: Data Analysis for X-Ray Absorption Spectroscopy Using IFEFFIT. *Journal of Synchrotron Radiation* **2005**, *12* (4), 537–541.
- (2) Toby, B. H.; von Dreele, R. B. GSAS-II: The Genesis of a Modern Open-Source All Purpose Crystallography Software Package. *Journal of Applied Crystallography* **2013**, *46* (2), 544–549.

CHAPTER 3

AN INNOVATIVE LITHIUM-ION BATTERY SYSTEM BASED ON A CU₂S ANODE MATERIAL

The majority of this chapter was published in ACS applied materials & interfaces

An Innovative Lithium Ion Battery System Based on a Cu₂S Anode Material

Yunhui Wang[#], Xinran Feng[#], Yin Xiong, Stanislav Stoupin, Rong Huang, Min Zhao, Mingsheng Xu, Peng Zhang*, Jinbao Zhao*, and Héctor D. Abruña*

ACS Appl. Mater. Interfaces 2020, 12, 15, 17396–17405

co-first authors

3-1. Introduction

The growing threats of global climate changes have made rechargeable batteries one of the dominant energy storage technologies. Benefiting from their long cycle life and high energy/power densities, lithium-ion batteries (LIBs) have surpassed other battery systems, becoming the most commonly used power device in portable electronics and electric vehicles.¹ However, concerns about their cost and safety remain, requiring alternative materials/systems to be developed²⁻³.

Copper-based sulfides (CuS and Cu₂S) are promising electrode materials for lithium-ion batteries. They have gained a high level of interest due to their abundance, low cost, environmental friendliness, and excellent intrinsic functional properties, including their charge carrier mobility.⁴⁻⁵ According to previous publications, Cu₂S

has better cycling and rate performance capabilities resulting from its higher conductivities and the displacement reaction between Cu_2S and Li_2S . This unique reaction is enabled by the similar crystal structures between Cu_2S and Li_2S and high Cu^+ mobility⁶.

Different from other conversion-reaction based metal sulfides, Tarascon and Adelhelm et al. pointed out that copper sulfides exhibit a unique displacement reaction, involving a process of highly reversible lithium/copper ions insertion/extrusion in the stable sulfur matrix based on the structural similarities between Cu_2S and its lithiated product (Li_2S), as well as the high mobility of Cu^+ within the Cu_2S lattice.⁷⁻⁹ Upon discharge, micron-scale long Cu dendrites were observed, in which the Cu atoms were extruded out of the sulfur matrix. This unique mechanism could promote stable cycling performance (in the hundreds of cycles without noticeable capacity fade) and excellent rate capability (up to 10 C).¹⁰ Similar to $\text{Li}_4\text{Ti}_5\text{O}_{12}$, the high charge/discharge plateaus of Cu_2S (~1.7 V vs. Li^+/Li) preclude the formation of hazardous lithium dendrites, making Cu_2S an exceptionally safe anode material. Compare with $\text{Li}_4\text{Ti}_5\text{O}_{12}$, Cu_2S has a much higher theoretical capacity (~335 $\text{mAh}\cdot\text{g}^{-1}$), which would yield a high energy density device when coupled to high voltage cathodes in state-of-the-art LIBs¹¹. These properties have made Cu_2S attractive for designing advanced rechargeable batteries, especially for large-scale electrical energy storage applications. However, electrolyte matching remains a critical factor affecting the electrochemical behavior of Cu_2S and therefore has precluded its commercialization⁸.

Cu₂S only exhibits stable cycling performance in ether-based electrolytes, which are not suitable for high voltage cathodes owing to their limited electrochemical stability. On the other hand, carbonate-based electrolytes commonly used in commercial LIBs are detrimental to Cu₂S, leading to dramatic capacity fade in less than ten cycles. Shi et al. investigated the failure mechanism of Cu₂S in carbonate-based electrolytes. They found that the Cu₂S reacted with cyclic carbonates, in which the side reaction products covered on the surface of the electrode, preventing it from further cycling¹². Although Cu₂S electrodes have better performance in pure linear carbonates, the capacity of the Cu₂S cell continuously fades, no need to say it is impractical to solely use the linear carbonates as the solvent for lithium-ion batteries. Cu₂S is often listed as a 'promising' cathode material in most publications when paired with a lithium metal anode and cycled in ether-based electrolytes. However, it remains far from practical applications due to the very challenging constraints of employing a lithium metal anode¹³⁻¹⁵.

Thus, it is crucial to understand the failure mechanism of Cu₂S in carbonate-based electrolytes and identify potential solutions, which could enable its commercialization as an anode in LIBs. In this chapter, we present an investigation on the electrochemical responses of Cu₂S in both ether- and carbonate-based electrolytes under *operando* conditions, aiming to fundamentally understand their origins. *Operando* measurements enable the study of sensitive reaction intermediates, which is key to achieving a fundamental understanding of the actual electrochemical process under the battery's native environment¹⁶. We have developed a composite material with a uniform carbon coating capable of suppressing the surface reactions between

Cu₂S and carbonate-based electrolytes to maintain its structural integrity and displacement mechanism, achieving stable electrochemical cycling performance in carbonate-based electrolytes. Furthermore, we assembled a full cell by coupling a Cu₂S/C composite as the anode with a LiCoO₂ cathode for the first time. It provided the basis for transferring Cu₂S to industrial-scale applications and battery systems for large-scale electrical energy storage applications.

3-2. Experimental Section

3-2-1 Materials

$\text{CuSO}_4 \cdot 5\text{H}_2\text{O}$, $\text{Na}_2\text{S}_2\text{O}_3 \cdot 5\text{H}_2\text{O}$, CuCl , $\text{CH}_4\text{N}_2\text{S}$ (TA, thiourea), $(\text{CH}_2\text{OH})_2$ (EG, ethylene glycol) and glucose were purchased from Sinopharm Chemical Reagent Corporation (Analytically pure). CuO and Cu_2O (99+ %, A.C.S. reagent) used as X-ray absorption spectroscopy standards were purchased from Aldrich Chemical Company, Inc. Cu_2S (99.5 %) standard was from Alfa Aesar Chemicals.

3-2-2 Preparation of $\text{Cu}_2\text{S}/\text{C}$ and Cu_2S

$\text{Cu}_2\text{S}/\text{C}$: $\text{CuSO}_4 \cdot 5\text{H}_2\text{O}$ (0.005 mol), $\text{Na}_2\text{S}_2\text{O}_3 \cdot 5\text{H}_2\text{O}$ (0.005 mol), and 1.2 g glucose were sequentially added into deionized water (100 mL) with magnetic stirring for 20 minutes. The resulting mixture was spray-dried (Buchi mini-spray drier B-290) with nitrogen as the carrier gas. The inlet temperature and the rotameter settings were 200°C and 40 mm, respectively. The aspirator and pump rates were 100% and 15%, respectively. The spray-dried precursors were transferred to a tube furnace and calcined at 500°C under the protection of Ar gas for 8 h. The calcined products were washed in deionized water several times, followed by vacuum drying overnight.

Cu_2S : A modified microwave (MW) method was used¹⁷. 0.02 mol CuCl and 0.01 mol thiourea were added to 50 mL EG and stirred for 20 min. The mixture was loaded into a microwave reactor (Model: LWMC-201, microwave frequency: 2450 MHz, output power: 650 W) and radiated by cyclic microwave treatment (18 s on, 42 s off) for 1 h. The resulting precipitate was washed in deionized water and absolute ethanol several

times, followed by drying in vacuum. The dried precursor was calcined at 350°C for 6 h under an Ar atmosphere, followed by cooling down to room temperature.

3-2-3 Physical characterization

The morphologies of Cu₂S and the Cu₂S/C composites were characterized using scanning electron microscopy (SEM, Hitachi S-4800) and transmission electron microscopy (TEM, JEM-2100). Raman spectra (Renishaw plc., UK) were recorded using a laser wavelength of 532 nm excitation with a resolution of 1 cm⁻¹.

Thermogravimetric analysis (TGA) was performed on an SDT Q600 (TA Instruments) analyzer, while TGA measurements were carried out under an airflow from room temperature to 800 °C, at a heating rate of 10 °C min⁻¹.

3-2-4 Electrochemical measurements

Cu₂S/C half cells: An electrode slurry was prepared by mixing the as-prepared Cu₂S/C (Cu₂S), acetylene black (AB), and polyvinylidene fluoride (PVDF) in weight ratios of 7: 1.5: 1.5 and stirring in N-methyl-2-pyrrolidinone (NMP) for 3 h, followed by coating onto a copper foil current collector with a doctor blade. The electrode was dried at 60°C under vacuum for 24 h. CR2016-type coin cells were assembled in an Ar-filled glovebox with lithium metal as the counter electrode and Celgard 2400 as the separator. Two different types of electrolytes were used. The first was 1 M LiPF₆ dissolved in a 1:1 mixture of ethylene carbonate (EC) and diethyl carbonate (DEC). The other was 1 M lithium bis(trifluoromethanesulfon)imide (LiTFSI) dissolved in a 1:1 mixture of 1,3-dioxolane (DOL) and dimethyl ether (DME). Constant current and

voltage (CC/CV protocol with a Neware battery program-control system) charge and constant current discharge measurements were performed at different current densities over the voltage range from 1.0 to 3.0 V versus Li^+/Li at room temperature (The cell was charged at a constant current to 3.0 V, then kept charging at 3.0 V until the current decreased to 1/10 of that constant current). Cyclic voltammetry tests were conducted on a CHI 1030C electrochemical workstation (Chenhua, Shanghai) at a scan rate of 0.2 mV s^{-1} . Electrochemical impedance spectra (EIS) over the frequency range from 10^{-1} to 10^5 Hz at different states of discharge/charge were conducted with a Metrohm Autolab PGSTAT 302N electrochemical workstation. Mass loadings of $\text{Cu}_2\text{S}/\text{C}$ in the coin cells ranged from 1.2 to 1.5 mg cm^{-2} . The specific capacity of $\text{Cu}_2\text{S}/\text{C}$ was calculated based on the total mass of the $\text{Cu}_2\text{S}/\text{C}$ composite. All electrochemical measurements were conducted at room temperature.

LiCoO₂/Cu₂S/C pouch cell: The positive electrode consisted of a single-sided 32 mm x 32 mm LiCoO_2 -coated Al foil with a mass loading (LiCoO_2) of 3.1 mg cm^{-2} on one side of the foil (the weight ratio of LiCoO_2 : AB: PVDF was 8 : 1: 1). The $\text{Cu}_2\text{S}/\text{C}$ electrode consisted of a single-sided 30 mm x 30 mm $\text{Cu}_2\text{S}/\text{C}$ coated Cu foil with a mass loading of 1.5 mg cm^{-2} on one side of the foil. The pouch cell was assembled in a dried ambient environment, followed by injection of the electrolyte (1 M LiPF_6 in EC/DEC) in an Ar-filled glovebox.

Operando cells: The *operando* coin cells were made from CR2032-type coin cell casings. A 3 mm diameter hole was drilled in the center and sealed with Kapton

polyimide film (0.13 mm thick) using Torr Seal epoxy. A schematic diagram of the *operando* cell is shown in Chapter 2 (Fig. 2-1). Aluminum foil was used as the current collector. *Operando* coin cells were cycled at 0.2 C with a Biologics SP-200 potentiostat.

3-2-5 *Operando* X-ray absorption spectroscopy measurements

Cu K-edge X-ray absorption spectroscopy (XAS) data collection was performed at beamline F-3 of the Cornell High Energy Synchrotron Source (CHESS). The measurements were done in transmission mode from 150 eV below the metal K-edge to 550 eV above the edge with N₂-filled ion chambers. A Cu metal foil spectrum was collected simultaneously to calibrate the incident X-ray energy and served as a reference spectrum. XANES (X-ray Absorption Near-Edge Structure) spectra were calibrated and normalized with the ATHENA software package. Fourier transformed EXAFS (Extended X-ray Absorption Fine Structure) spectra were obtained by applying a Hanning window from 3 to 11 Å⁻¹ with *k*²-weighting in ATHENA and fitted with standard Cu₂S and Cu crystal structures using the ARTEMIS package¹⁸.

3-2-6 *Operando* X-ray diffraction measurements

Operando powder X-ray Diffraction (XRD) patterns were collected at beamline A-1 of the Cornell High Energy Synchrotron Source (CHESS) at an incident energy of 19.82 keV ($\lambda = 0.6246$ Å) using an ADSC Quantum-210 CCD detector. A dark current correction was applied to the collected 2D XRD patterns. A baseline

diffraction pattern (snapshot) was collected for an empty *operando* coin cell containing all parts, except for the Cu₂S/C electrode slurry, to determine peaks from cell components and impurities. This background diffraction pattern was subtracted from the *operando* patterns during data analysis. The Kapton film and epoxy have minimal contributions to the diffracted signal. Each sample was exposed to the X-ray beam for 40 s every 4 mins to minimize potential beam-induced damage. The obtained *operando* 2D XRD snapshots were reduced to 1D diffraction patterns by azimuthal integration using the GSAS-II software package¹⁹. To facilitate interpretation of the resulting 1D XRD patterns, the radial coordinate (representing the modulus of the X-ray momentum transfer) was converted to the 2 theta scattering angle corresponding to the wavelength $\lambda = 1.05406 \text{ \AA}$ of the commonly used Cu K $_{\alpha}$ X-ray source.

3-3. Results and Discussions

3-3-1 Physical properties and electrochemical performances of Cu₂S/C

To prevent the side reactions between Cu₂S and carbonate-based electrolytes, it is crucial to create a protective layer on the Cu₂S surface. Carbon coating, a common strategy for enhancing the performances of cathodes and anodes in LIBs, is an excellent choice due to its superior electrical conductivity, chemical/electrochemical stability, and mechanical strength. An ordinary carbon coating strategy cannot meet the requirement considering the reactive sensitivity with carbonates and the volume change during cycling. Here, we propose an in-situ carbon coating method to fabricate the Cu₂S/C composite.

The synthesis procedure is illustrated in Fig. 3-1. A CuSO₄ and glucose aqueous dispersion was sprayed at 200 °C to obtain precursor-1. As the aqueous solution evaporated while spraying at high temperature, the concentration of precursor-1 gradually increased²⁰. When sprayed at 200 °C, S₂O₃²⁻ ions dissociate to SO₄²⁻ and HS⁻. The latter reacts with Cu(II) ions to form cuprous sulfide and Na₂SO₄ as a byproduct, accompanied by the dehydration of glucose, which acted as the carbon source²¹. Precursor-1 was then transferred to a tube furnace and calcined at 500 °C under the protection of Ar gas to produce precursor-2, while the dehydrated glucose was carbonized into amorphous carbon. The byproducts were later removed by washing with H₂O, and the Cu₂S/C composite was obtained. Different from the conventional synthetic method, the in-situ carbon coating method owns the following advantages: (1) carbon coating and copper sulfides synthesis were completed

simultaneously; (2) Cu_2S particles in nano-scale was obtained, which reduces the volume effect during cycling; (3) the Cu_2S nanoparticles were entirely protected by the carbon layer, preventing their contact with the carbonate-based electrolytes.

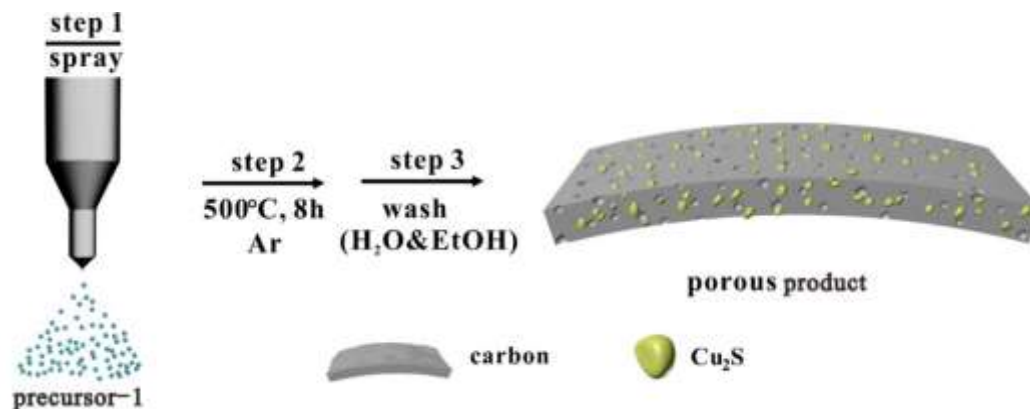


Figure 3-1 Schematic illustration of the $\text{Cu}_2\text{S}/\text{C}$ composite synthesis procedure.

The morphology and structure of the $\text{Cu}_2\text{S}/\text{C}$ composite and Cu_2S were confirmed by SEM, TEM, and XRD. The SEM image of the $\text{Cu}_2\text{S}/\text{C}$ composite (Fig. 3-2) showed Cu_2S nanocrystals are interconnected by carbon matrix and uniformly dispersed in the composite structure. The in-situ formed connected carbon matrix could construct a uniform wrap to prevent interaction between the electrolyte and Cu_2S . The TEM (Fig. 3-3) images then presented that Cu_2S nanoparticles, which have higher intensity in the image, were embedded in the carbon matrix with an amorphous structure. The lattice spacing of 0.324 nm was indexed to the (111) plane of Cu_2S (Fig. 3-3b).

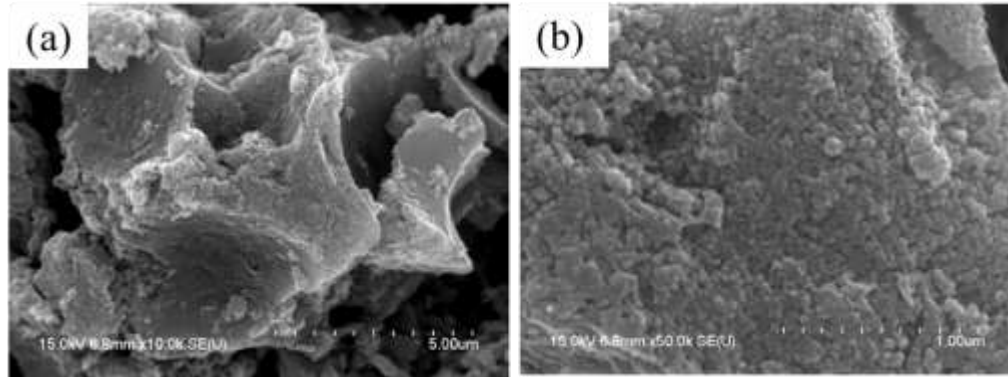


Figure 3-2. SEM images of Cu₂S/C composite

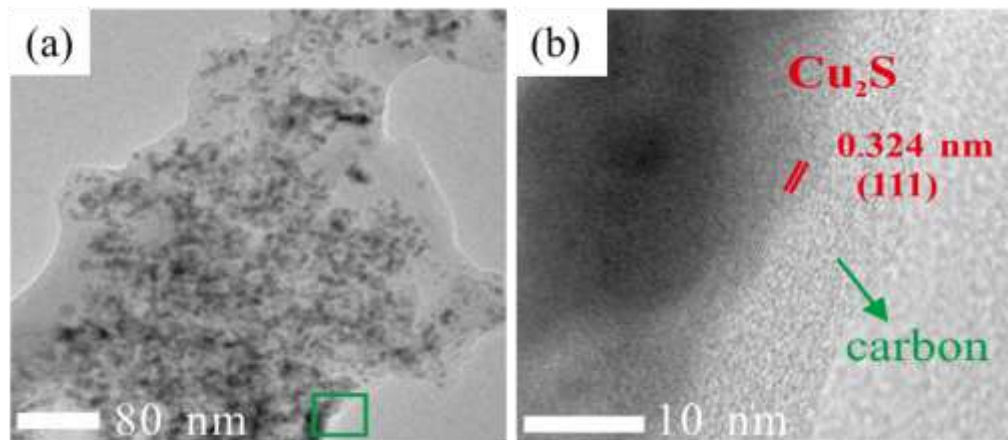


Figure 3-3. (a) TEM and (b) HR-TEM images of the Cu₂S/C composite

The XRD patterns (Fig. 3-4) of Cu₂S and Cu₂S/C are well indexed to the standard card of Cu₂S (JCPDS: 003-1071). The high background signal and broad peak width of the Cu₂S/C XRD pattern were attributed to the amorphous carbon and small Cu₂S particle size in the composite, respectively.

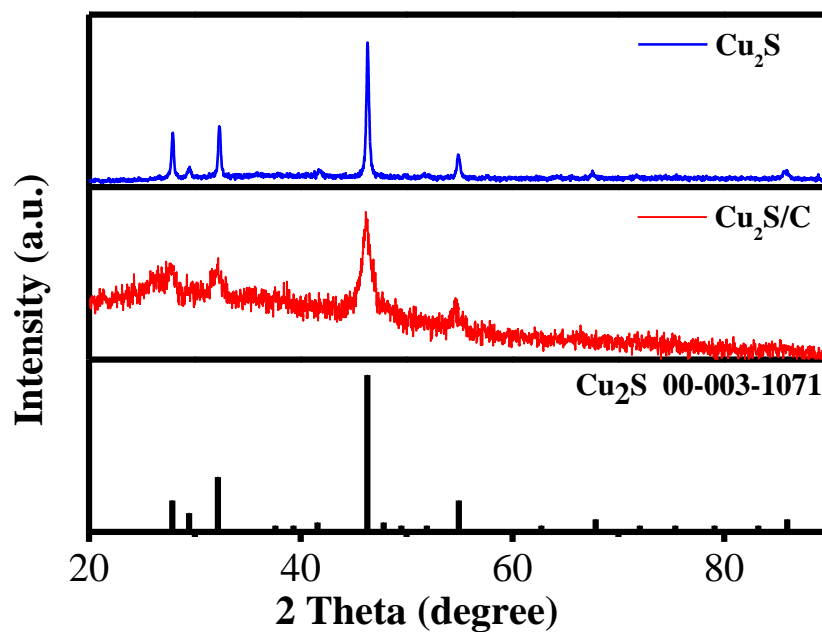


Figure 3-4. XRD patterns of Cu₂S, Cu₂S/C composite, and Cu₂S reference

The prepared Cu₂S had a flake morphology with a thickness of about 50 nm (Figs. 3-5a and 3-5b). The HRTEM (Fig. 3-5d) confirmed the lattice spacing of 0.278 nm, ascribed to the (200) plane of Cu₂S.

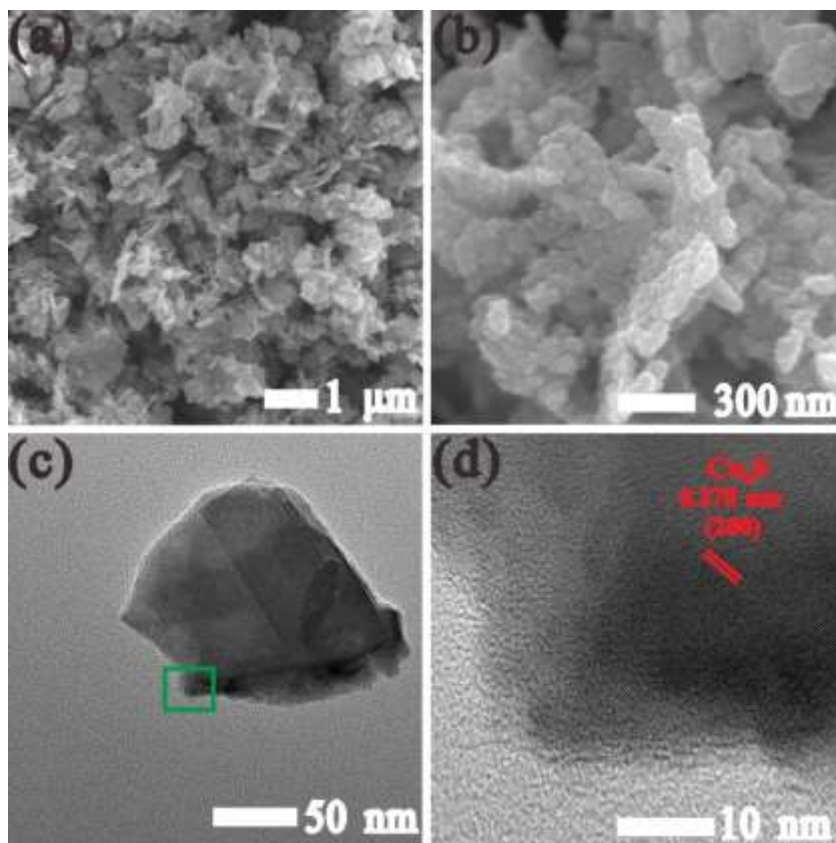


Figure 3-5. (a), (b) SEM images, (c) TEM and (d) HRTEM images of Cu_2S .

Raman spectroscopy measurements were performed for Cu_2S and $\text{Cu}_2\text{S}/\text{C}$. In Fig. 3-6, the peaks at 1360 and 1594 cm^{-1} correspond, respectively, to the D band and G bands of the carbon matrix²²⁻²³. The typical S-S peak at near $\sim 470\text{ cm}^{-1}$ was observed for the Cu_2S but not for $\text{Cu}_2\text{S}/\text{C}$. This may be related to the intense light-absorbing ability of the wrapping carbon matrix²⁴⁻²⁵.

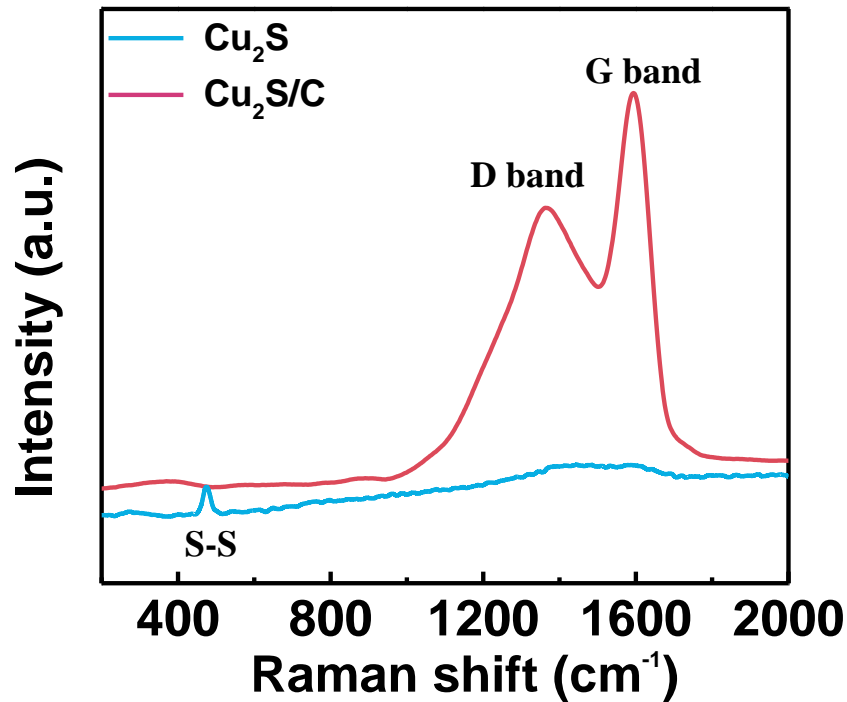


Figure 3-6. Raman spectra of Cu_2S and $\text{Cu}_2\text{S}/\text{C}$

TGA measurement of the $\text{Cu}_2\text{S}/\text{C}$ was conducted to determine its carbon content. Fig. 3-7 shows the TGA weight loss profile of $\text{Cu}_2\text{S}/\text{C}$. In an air atmosphere, Cu_2S experiences different oxidation and decomposition reactions. According to the phase diagram, Cu_2S oxidizes to Cu_2O above 700°C after carbon was consumed entirely.¹³ In the profile, the initial mass drop at around 100°C arises from water evaporation. It then exhibited a pronounced mass loss corresponding to carbon loss in the composite via CO_2 formation. The later mass increase (starting at around 300°C) comes from the oxidation of Cu_2S to CuO (and perhaps CuSO_4), eventually forming Cu_2O at temperatures above 700°C .

Based on this analysis, we calculated the amount of Cu_2S in the $\text{Cu}_2\text{S}/\text{C}$ composite using the weight percent of Cu_2O at 800 °C (final product), assuming that all of the Cu_2S was completely converted Cu_2O . The molar mass ratio of Cu_2O to Cu_2S is 0.899 (molecular weight: Cu_2S -159 g/mol, Cu_2O -143 g/mol). Therefore, a final Cu_2O weight % of 52.1 % converts to the theoretical weight % of Cu_2S in the composite, which yields a value of 57.9 wt%. Therefore, the weight percentage of carbon in the composite is 39.9% (97.8%-57.9%).

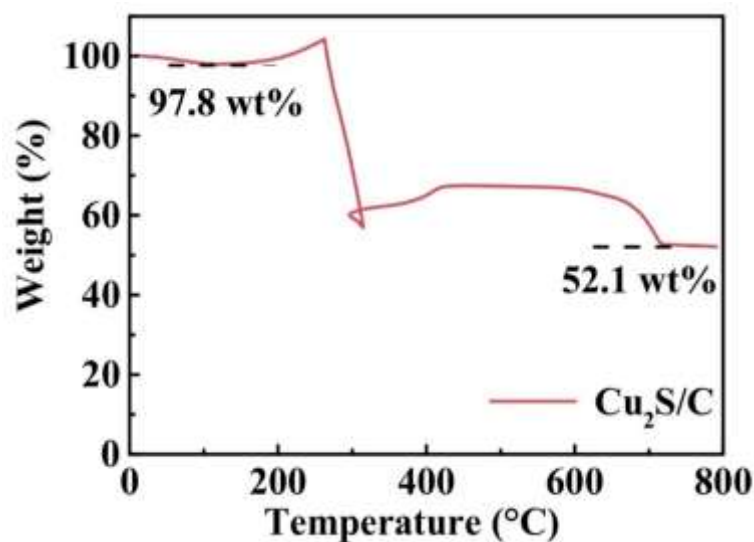


Figure 3-7. TGA weight loss profile of $\text{Cu}_2\text{S}/\text{C}$.

As previously reported, the choice of electrolyte is the determining factor for the cycling performance of Cu_2S . Jache et al. have shown that Cu_2S exhibits excellent cycling performance in an ether-based electrolyte (DOL/DME), whereas it failed within several cycles in a carbonate-based electrolyte (EC/DEC)⁸. It was also proven that the cyclic carbonate electrolyte (EC) was disastrous to the cycling performance of

Cu₂S, in a way that was similar to the incompatibility between carbonate-based electrolytes and Li-S batteries^{12, 26-27}. Cu₂S/C composites overcame this limitation by surviving in carbonate-based EC/DEC electrolytes and achieving stable reversibility and cycling. It achieved a reversible capacity of 123 mAh g⁻¹ (corresponding to a capacity of 192 mAh g⁻¹ based on the mass of Cu₂S) after 100 cycles, while the capacity of the Cu₂S quickly decayed to 0 within 10 cycles (Fig. 3-8).

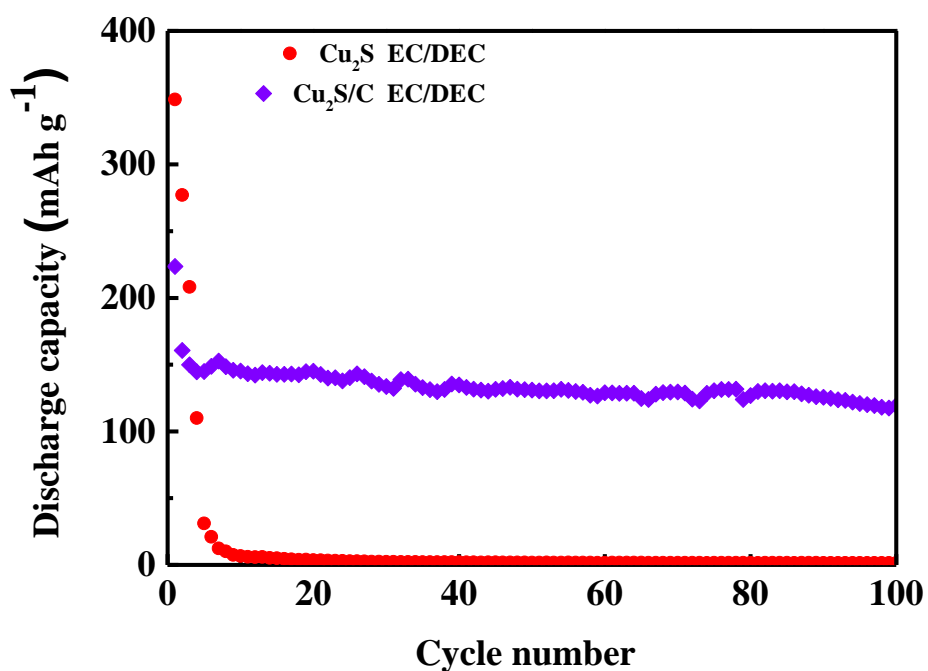


Figure 3-8. Cycling performances of Cu₂S and Cu₂S/C in EC/DEC at 200 mA/g. The specific capacity of Cu₂S/C was calculated based on the mass of the Cu₂S/C composite.

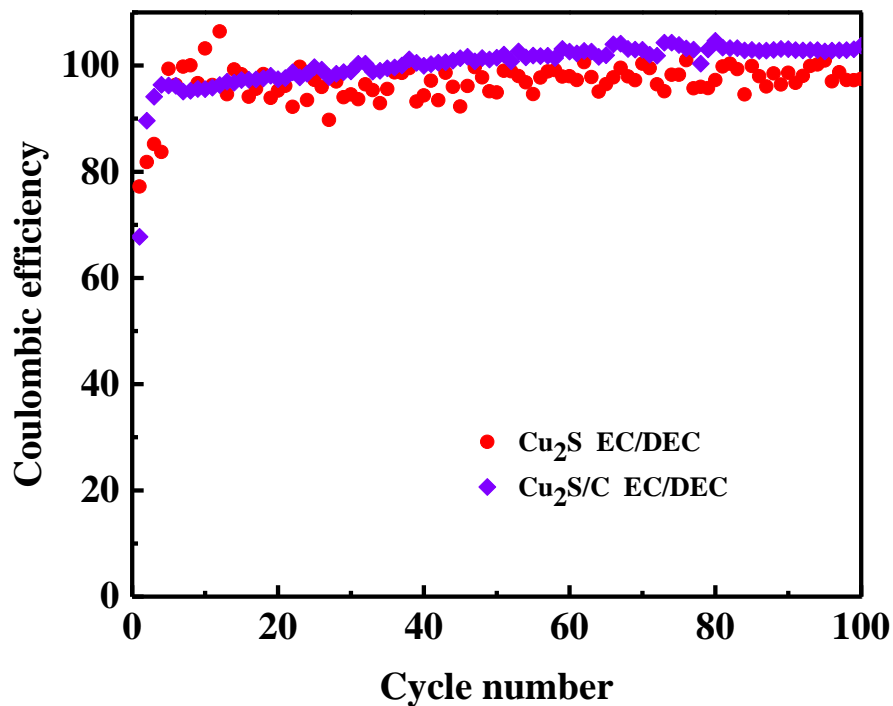


Figure 3-9 Coulombic efficiency of Cu₂S and Cu₂S/C in EC/DEC at 200 mA/g

Since the main point in this work is to provide a strategy to address the incompatibility between Cu₂S and carbonate-based electrolytes, the carbon content was not optimized. The capacity of Cu₂S/C could be further improved by lowering the carbon content on the premise that the protection layer is still effective. The increase in coulombic efficiency during the extended cycling may be artificially caused by parasitic reactions. The cycling performances of Cu₂S and Cu₂S/C in DOL/DME electrolytes were also tested (Fig. 3-10). Agreeing with previous reports, both exhibited excellent cycling stability^{8, 10, 28}. After 100 cycles, the discharge capacities of Cu₂S and Cu₂S/C were 333 and 250 mAh g⁻¹ (based on the mass of the Cu₂S/C composite), respectively.

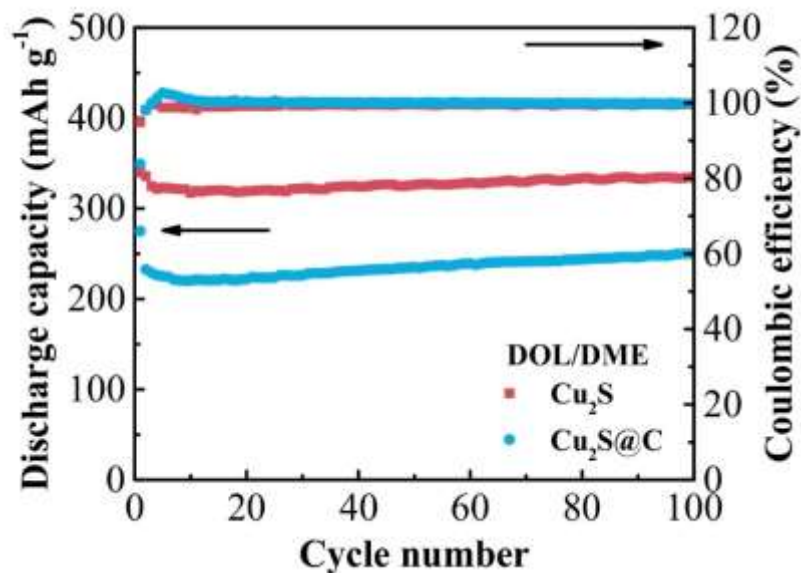


Figure 3-10. Cycling performances of Cu₂S and Cu₂S/C in DOL/DME at 200 mA/g.

It has been reported that the excellent cycling performance of Cu₂S can be ascribed to its unique displacement reaction. The sulfur ions can be considered as an array (sulfur array), in which both Cu(I) and Li(I) ions, with similar ionic radii, can insert/extrude reciprocally during charge and discharge processes, thus maintaining the structural integrity of the sulfur array⁷⁻⁹. The 2.1 V discharge plateau is related to the lithiation of nonstoichiometric cuprous sulfide, explained in the later section. The charge plateau at 2.3 V (which decays on subsequent cycles) of Cu₂S (Figs. 3-11a and 3-11b) was ascribed to the electrochemical reactions associated with Li₂S, which were also observed in the previous works⁸. Upon subsequent cycling, a pair of flat (dis)charge plateaus at 1.8 V emerged (Figs. S-11a and 3-11c), ascribed to the highly reversible reaction between Cu₂S and Cu/Li₂S^{8,29-30}. On the other hand, in EC/DEC electrolytes, Cu₂S exhibits poor cycling performance. The (dis)charge profiles decay after 5 cycles, while those of Cu₂S/C can be observed after 100 cycles (Fig. 3-11d).

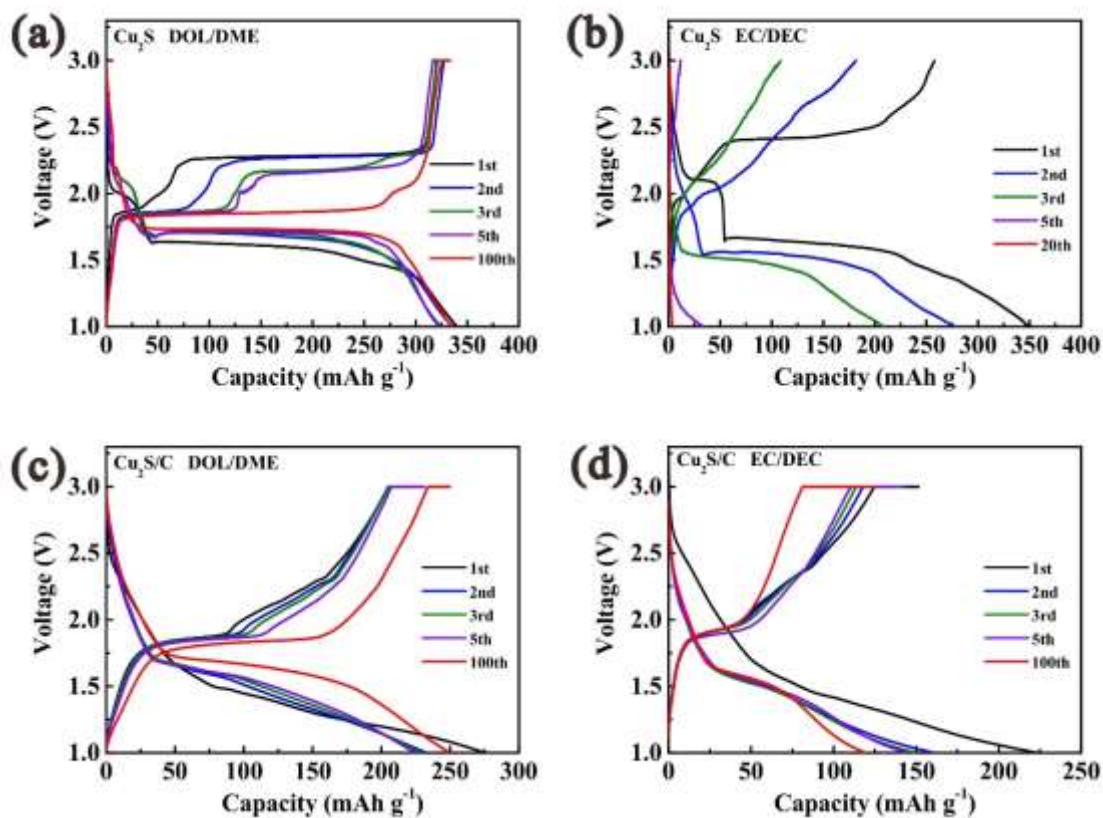


Figure 3-11. Charge and discharge profiles of Cu₂S in (a) DOL/DME and (b) EC/DEC electrolytes, Cu₂S/C in (c) DOL/DME and (d) EC/DEC electrolytes at 200 mA g⁻¹.

The specific capacity of Cu₂S/C was calculated based on the mass of the Cu₂S/C composite.

Furthermore, the long-term cycling performance of Cu₂S/C was tested at 20 mA g⁻¹.

After 200 cycles, a reversible capacity of 118 mAh g⁻¹ was obtained (corresponding to a capacity of 197 mAh g⁻¹ based on the mass of Cu₂S) (Fig. 3-12). The improved cycling performance is closely related to the carbon matrix protection of the Cu₂S active material, also suggesting the possibility of making carbonate-based electrolytes compatible with Cu₂S.

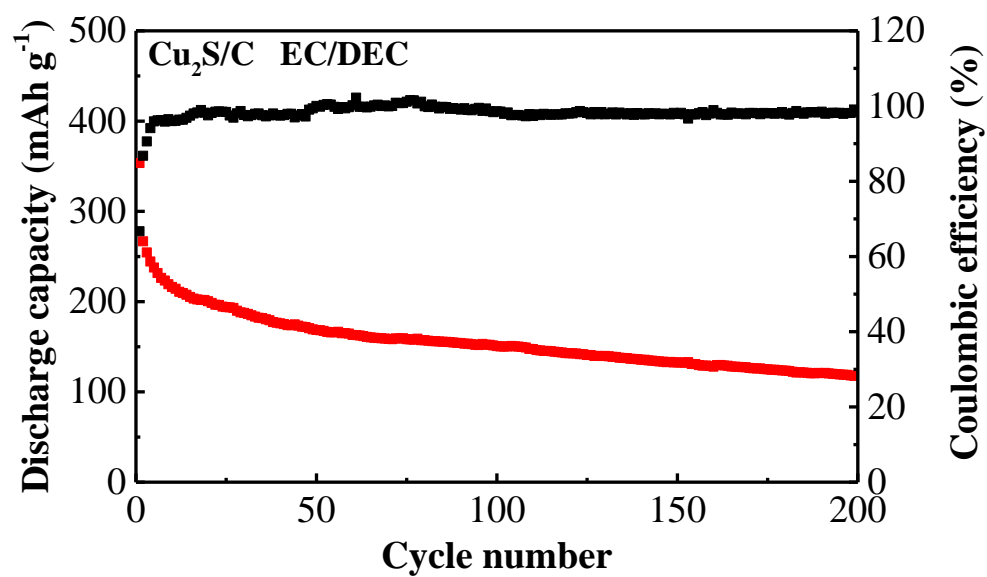


Figure 3-12. Long-term cycling performance of Cu₂S/C in EC/DEC at 20 mA g⁻¹. The specific capacity of Cu₂S/C was calculated based on the mass of the Cu₂S/C composite.

3-3-2 Operando XAS investigation of the Cu₂S mechanism in ether-/carbonate-based electrolytes

Intrigued by the behavioral difference of Cu₂S in carbonate- and ether-based electrolytes, *operando* X-ray absorption spectroscopy (XAS) measurements were performed for Cu₂S in the two electrolytes mentioned above. The XAS spectra for powder samples (Cu₂S synthesized with microwave (MW) method, Cu₂S/C, commercial Cu₂S, and Cu₂O) are shown in Fig. 3-13. The very similar spectral shapes of the synthesized Cu₂S and the commercial Cu₂S (c-Cu₂S) and Cu₂O (c-Cu₂O) samples again demonstrated that Cu₂S and Cu₂S/C had been successfully synthesized.

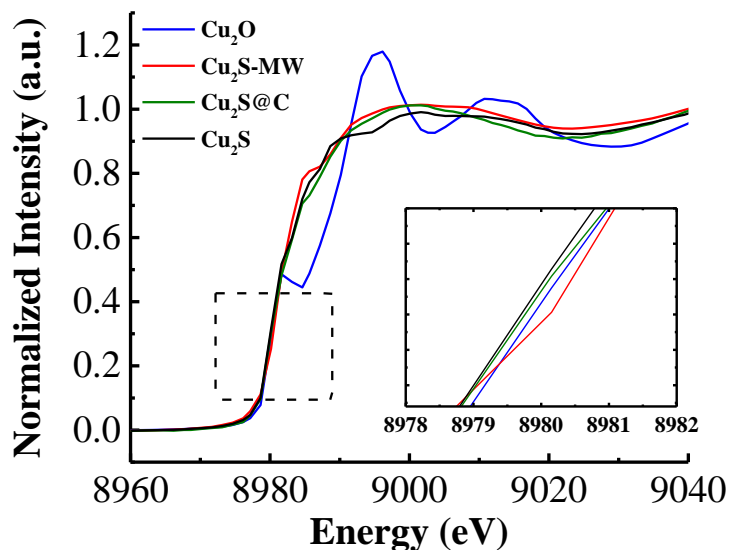


Figure 3-13. Cu K-edge XANES powder spectra of c-Cu₂O, c-Cu₂S, Cu₂S, and Cu₂S/C

The powder spectra were also in accordance with the XRD and TEM data showed previously. The Cu valence states of synthesized Cu₂S (Cu₂S and Cu₂S/C) were first analyzed, with c-Cu₂S and c-Cu₂O used as standards. The edge energies of c-Cu₂S and

c-Cu₂O were 8979.98 and 8980.26 eV, respectively. The slightly lower edge energy of c-Cu₂S resulted from the higher covalency between Cu-S bonds when compared to Cu-O bonds. The Cu₂S/C (8980.13 eV) edge energy was close to those of c-Cu₂S and c-Cu₂O, indicating a +1-oxidation state of Cu in Cu₂S/C. However, the synthesized Cu₂S exhibited higher edge energy of 8981.21 eV and thus has a higher oxidation state of Cu compared with the others. This could come from a small amount of Cu₂S readily oxidized in air, leading to the emergence of nonstoichiometric cuprous sulfide. Such a trace amount of nonstoichiometric cuprous sulfide could also explain the presence of a discharge voltage plateau at 2.1 V (Fig. 3-11b)^{17,31}. Moreover, the edge energy differences between Cu₂S and Cu₂S/C also indicate that the carbon wrapping serves as a protective layer and prevents the oxidation of Cu³².

The *operando* XANES spectra of Cu₂S and their corresponding voltage/time profiles are presented in Figs. 3-14,15,16 and 3-17,18,19, for experiments in DOL/DME and EC/DEC electrolytes, respectively. Shown in Figs. 3-14 and 3-17, Cu₂S experiences a similar transition during the discharge process in both electrolytes, gradually reduced to elemental copper. This was evident from a comparison of the edge energy at the end of the discharge (pt. 6) with that of the Cu foil and the similar oscillations above the white line. The isosbestic points in the spectra are consistent with a single redox reaction of Cu₂S during the electrochemical processes without any interferences or side reactions³³. Comparing the fully discharged XANES spectra (pt. 6) in both electrolyte systems with the Cu foil spectrum, the edge feature and the overall oscillations of the *operando* spectra exhibit a more smeared appearance. It is likely

due to the smaller size of the metallic copper formed during the discharge process than the bulk, which was previously shown by both experimental methods and multiple scattering calculations³⁴⁻³⁶.

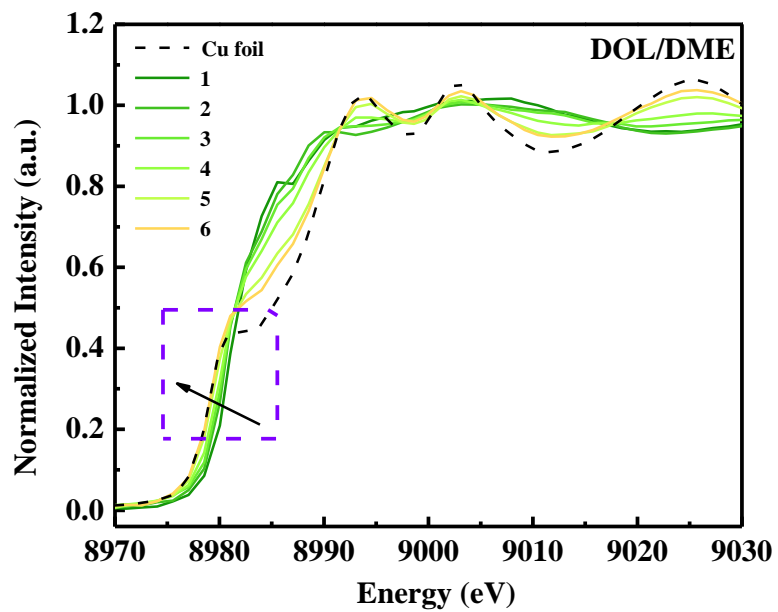


Figure 3-14 XANES patterns of Cu_2S discharge in DOL/DME

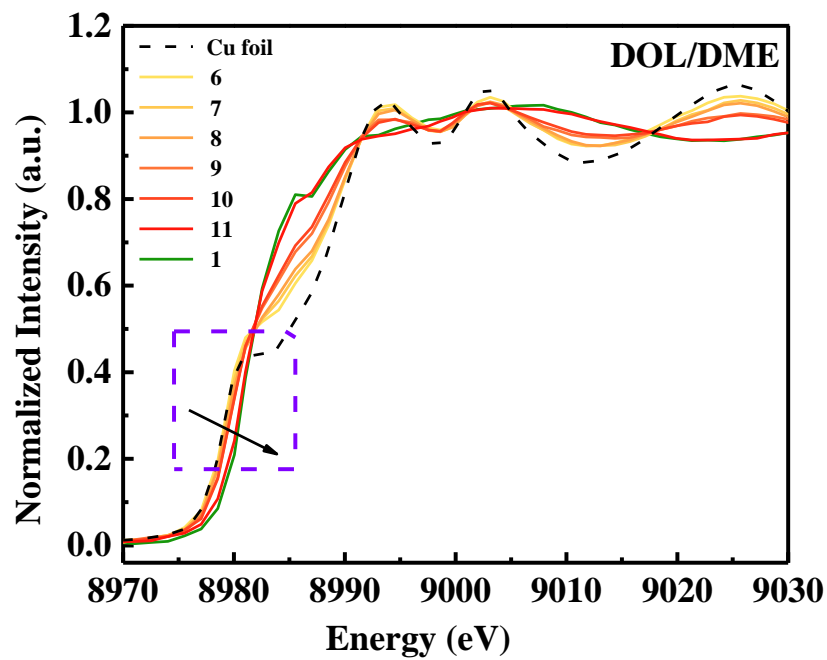


Figure 3-15 XANES patterns of Cu₂S discharge in DOL/DME

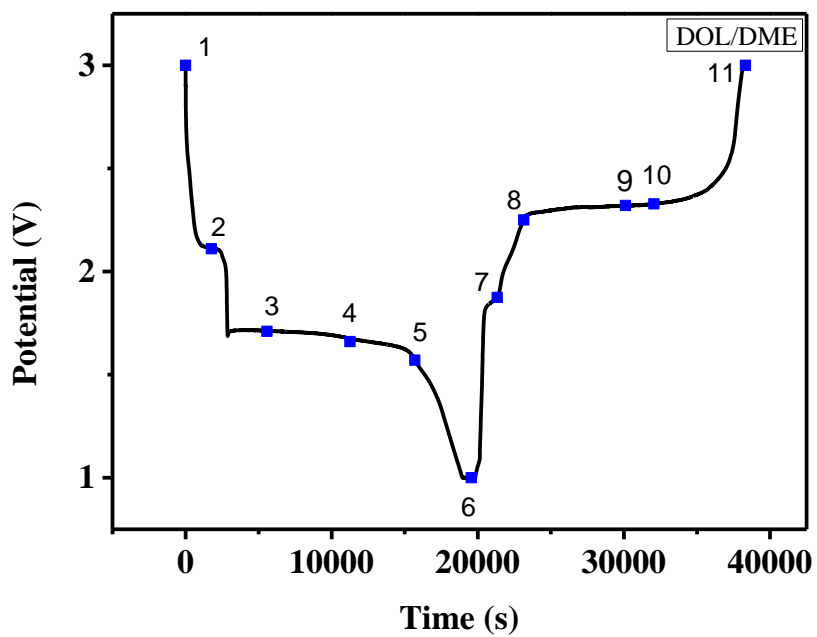


Figure 3-16. Charge/discharge profile of Cu₂S in DOL/DME

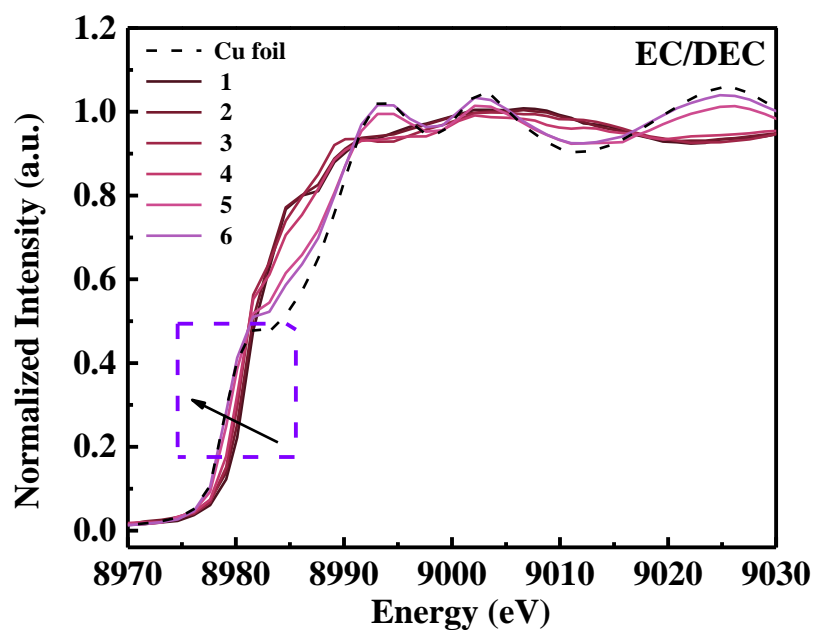


Figure 3-17 XANES patterns of Cu_2S discharge in EC/DEC

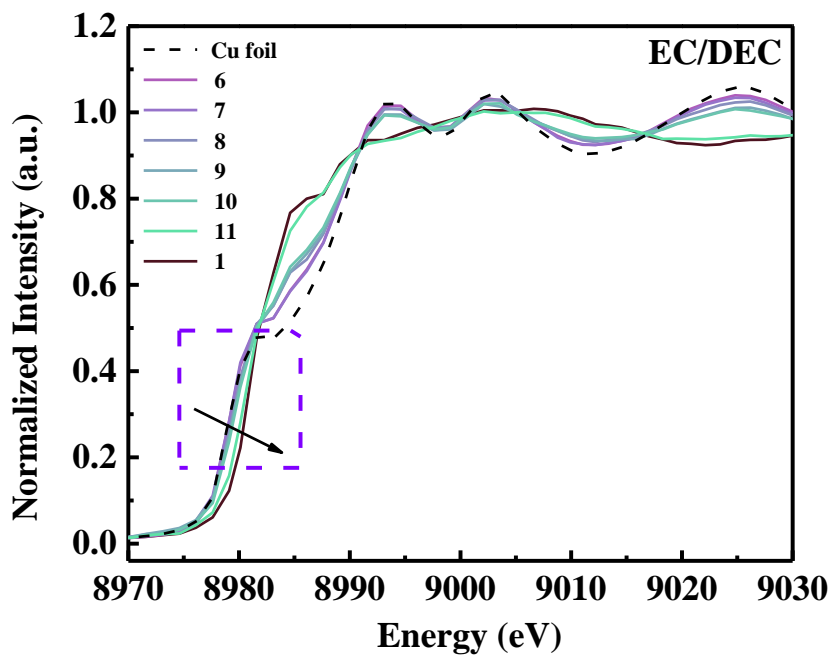


Figure 3-18 XANES patterns of Cu_2S charge in EC/DEC

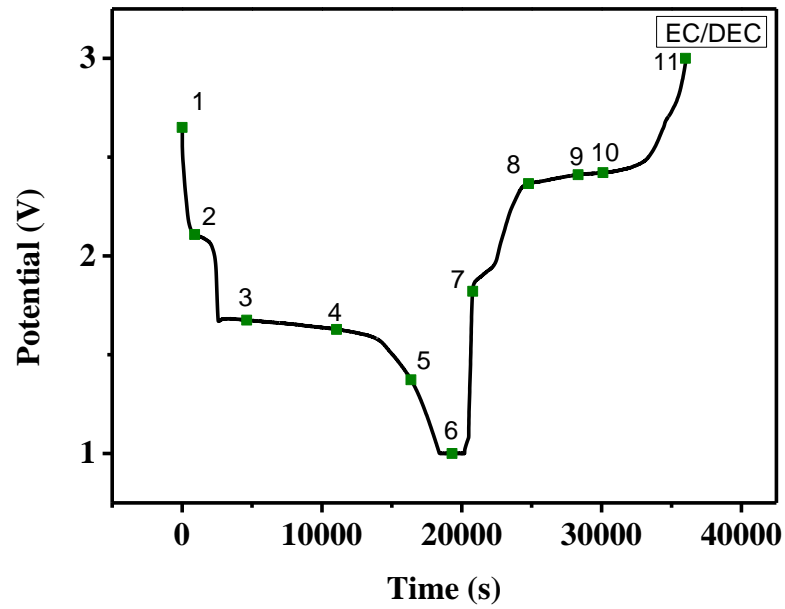


Figure 3-19. Charge/discharge profile of Cu₂S in EC/DEC

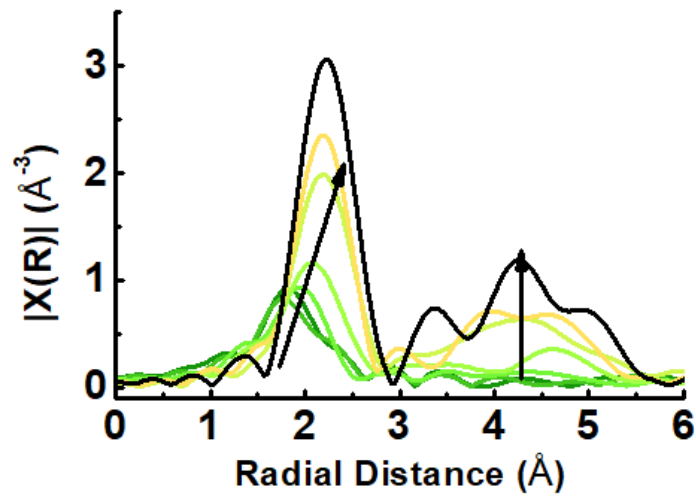


Figure 3-20 EXAFS patterns of Cu₂S discharge in DOL/DME

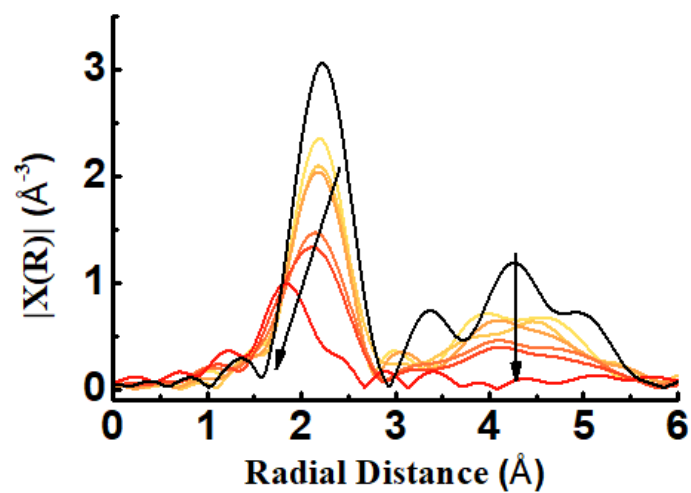


Figure 3-21 EXAFS patterns of Cu₂S charge in DOL/DME

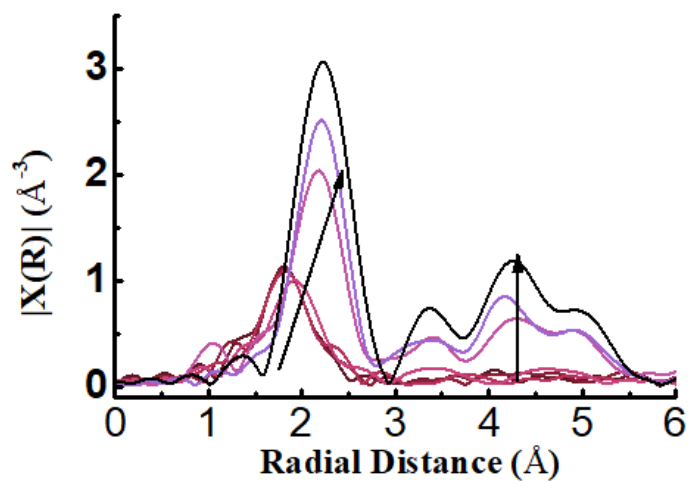


Figure 3-22 EXAFS patterns of Cu₂S discharge in EC/DEC

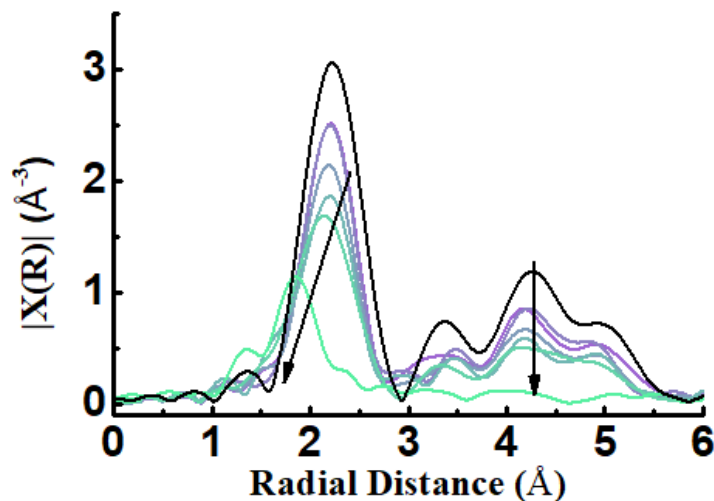


Figure 3-23 EXAFS patterns of Cu_2S charge in EC/DEC

The transition from Cu_2S to Cu can also be observed through the EXAFS spectra (Fig. 3-20 to 23). The peaks in the spectra reflect the bond distances between Cu and its surrounding S and Cu. In all EXAFS figures, the peak at around 1.9 Å in the pristine or fully recharged state represents the Cu-S bond distance in Cu_2S while the peaks at 2.2 Å, in the fully discharged state (pt. 6), represent the Cu-Cu bonds. The three connected humps from 3 to 5.5 Å in the fully discharged scan are from both single and multiple electron scatterings between the center Cu and the second and third shell Cu atoms. The appearance of outer shell peaks is strong evidence of the formation of Cu clusters. The peak fitting results are presented in the supplemental information (Fig. 3-24).

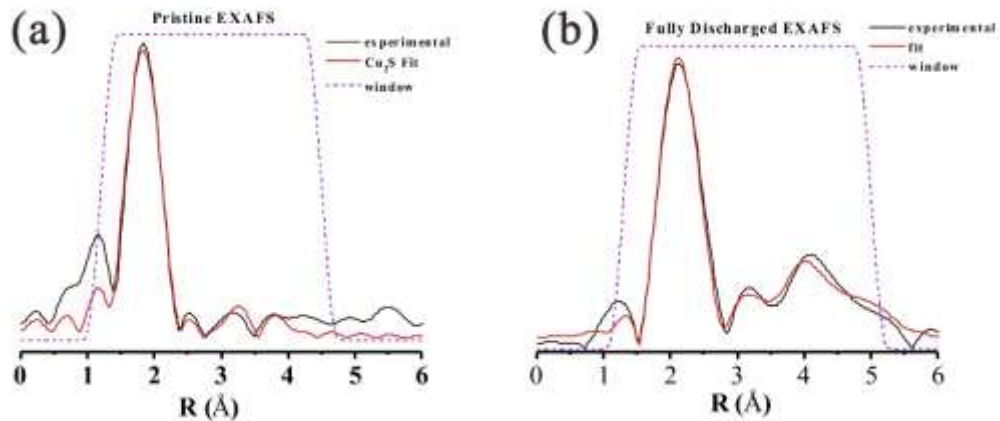


Figure 3-24 (a) EXAFS spectra of Cu K-edge for pristine sample scan and (b) fully discharged scan with the corresponding fit and fitting window in DOL/DME electrolyte.

Table 3-1. EXAFS fitting results of the pristine and fully discharged Cu₂S in DOL/DME electrolyte

Sample/Reference	Cu-S distance (Å)*/ Debye-Waller factor	Cu-Cu distance (Å)*/ Debye-Waller factor
Pristine/Cu ₂ S	2.28465±0.00443/ 0.00572±0.00071	2.67964±0.00071/ 0.03509±0.00614
Fully Discharged/Cu	N/A	2.52829±0.00310 /0.00843±0.00041

*Atomic distances shown here are before phase correction.

Unlike the XANES spectra, EXAFS changes show that, in the DOL/DME electrolyte (Fig. 3-20), the sulfur atoms change gradually, in contrast to the sudden structure transition from Cu-S to Cu-Cu in EC/DEC (Fig. 3-22). Moreover, the EXAFS spectra also confirm the formation of copper clusters from the emergence of the first coordination Cu-Cu shell at 2.1 Å, as well as the second and third copper shell

multiple scatterings from 3 to 5.5 Å, before phase correction. For the charging process, Cu (0) is re-oxidized to Cu (I) in both electrolytes, during which the Cu is oxidized slowly at the beginning of the charging process and rapidly shifts to the Cu₂S edge energy at the end of the charge (Figs. 3-15 and 3-18). However, after closely comparing the spectra, it is observed that at the end of charge (pt. 11), the rising edge energy in DOL/DME is closer to the pristine scan (pt. 1), compared with the one in the EC/DEC system (highlighted in the purple dash line box). It suggests a more reversible chemical reaction in the ether-based electrolyte.

Similarly, the EXAFS spectra for the charging process show more prominent differences between the two electrolyte systems. In DOL/DME (Fig. 3-21), the Cu-S bonds gradually reform by slowly consuming the Cu clusters, according to the shift in the first Cu-Cu shell to Cu-S and the disappearance of Cu-Cu scattering from the second/third shells at 3-5.5 Å. In EC/DEC (Fig. 3-23), it is apparent that the Cu atoms prefer to stay in the form of Cu clusters through most of the charging process and only switch to Cu₂S at the end of the recharge. It is supported by the EXAFS spectra that, except for the last scan (pt. 11), largely resemble the one at the end of discharge (pt. 6). The decrease in peak intensity can be explained by the loss in Cu₂S crystallinity as the Li₂S/Cu is converted to Cu₂S.

The amount of reacted Cu₂S throughout the entire cycle can be calculated using linear combination analysis. The pristine spectrum (scan 1) and the most discharged spectrum (scan 6) were used as references. The results are plotted in Figs. 3-25 and 26.

After comparing these two figures, it is evident that Cu_2S , in the carbonate electrolyte, was oxidized slower during the charging process. This uneven speed may arise because diffused sulfide species formed byproducts with carbonate-based electrolyte during discharge, making it harder for Cu to recapture sulfur ions during the charge process²⁶. In addition, in EC/DEC, most Cu atoms prefer to remain as Cu (0) through the charging process, indicating a higher reaction barrier for the reformation of Cu_2S , in accordance with the larger overpotentials in EC/DEC.

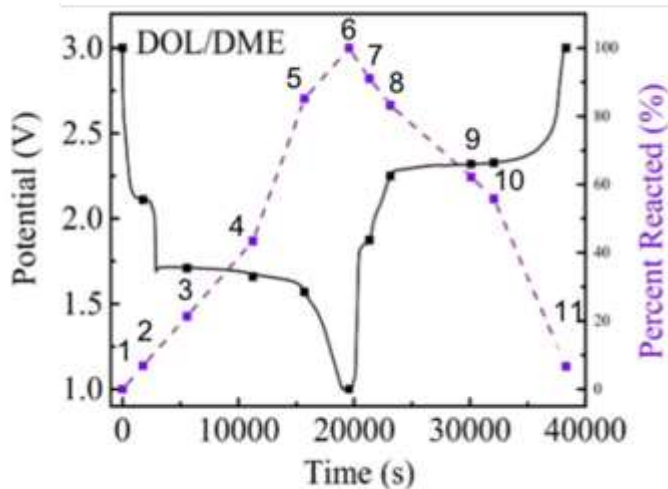


Figure 3-25. Charge/discharge profile of Cu_2S in DOL/DME and the percent of Cu_2S reacted at the selected states of charge.

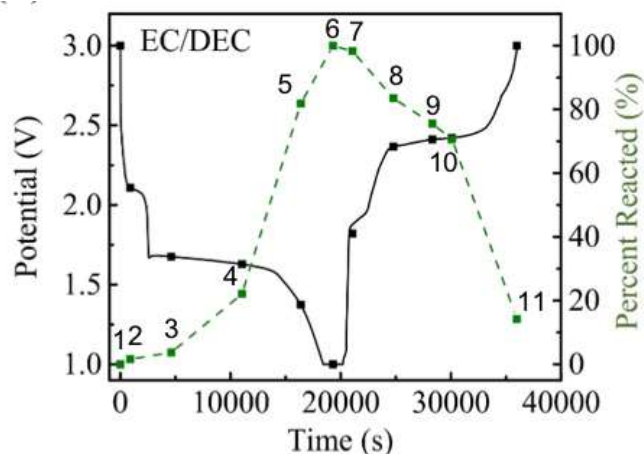


Figure 3-26. Charge/discharge profile of Cu_2S in EC/DEC and the percent of Cu_2S reacted at the selected states of charge.

TEM analysis of Cu_2S electrodes after 10 cycles in both electrolytes was carried out (Figs. 3-27). Compared to the pristine Cu_2S with fine crystallinity (Figs. 3-3), cycled Cu_2S in both electrolytes turned polycrystalline. In DOL/DME, $\text{Cu}_{1.96}\text{S}$ (the reason for choosing this phase will be articulated in the next section) with a highly similar crystalline orientation to Li_2S , with a lattice spacing of 0.327 nm, ascribed to the (102) face of $\text{Cu}_{1.96}\text{S}$.⁵ On the other hand, the crystalline orientation of products in EC/DEC is disordered, though the lattices ascribed to Cu and $\text{Cu}_{1.96}\text{S}$ can still be observed.

Based on the results discussed above, the performance of Cu_2S in carbonate-based electrolytes is inferior, relative to ether electrolytes, for the following reasons: (1) the abruptness of the crystal structure transition is detrimental to maintaining the sulfur backbone structure; (2) the higher energy barrier of the Cu_2S reformation results in a higher overpotential; (3) sulfide species dissolution is severe due to side reactions with carbonate-based electrolytes, resulting in a significant sulfur loss.²⁶⁻²⁷

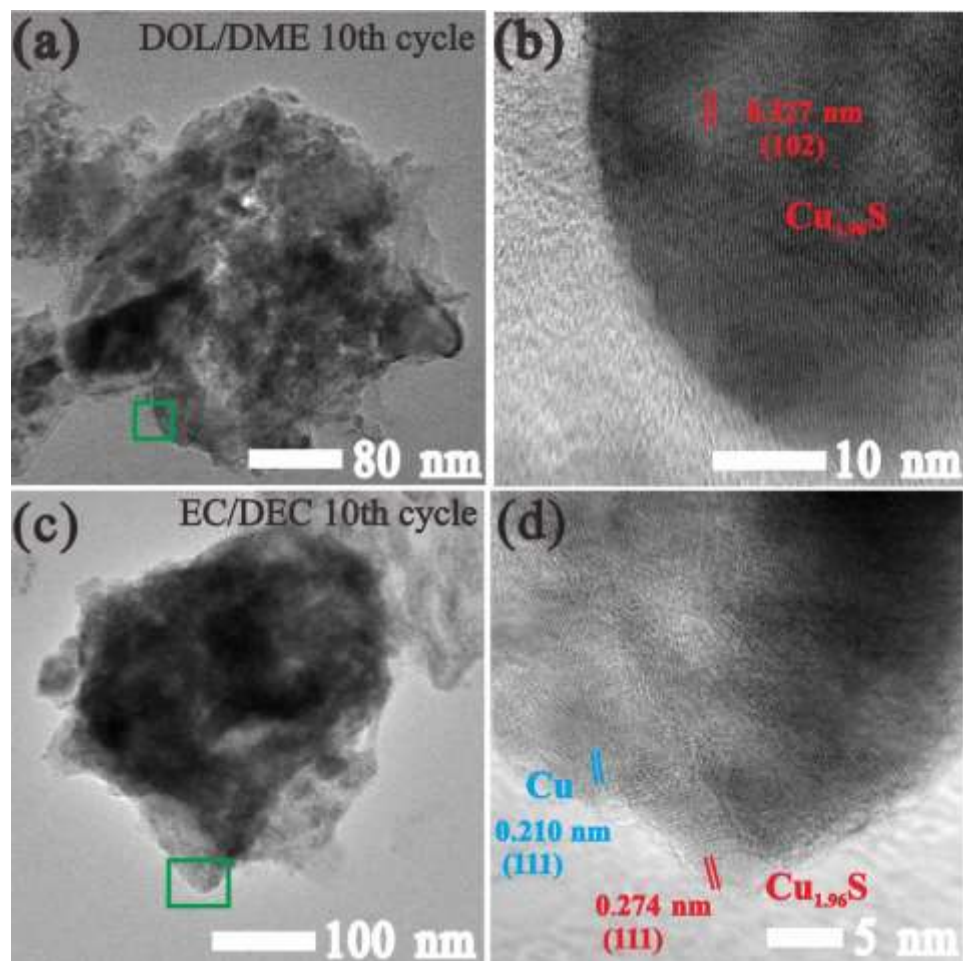


Figure 3-27. TEM and HR-TEM images of Cu_2S in (a, b) DOL/DME and (c, d) EC/DEC electrolytes after 10 cycles.

3-3-3 Evolution in the crystal structure of Cu₂S in DOL/DEM and EC/DEC electrolytes

Fig. 3-28 presents the *operando* XRD evolution of the Cu₂S crystal structure during the 1st cycle in DOL/DME. The diffraction peaks (27.7°, 32.1°, 46.2°, and 54.9°) of pristine Cu₂S shift to lower angles, followed by the emergence of a new phase. The small peak shifts (~ 2.1 V) are attributed to the lattice expansion resulting from the lithiation of nonstoichiometric cuprous sulfide. The diffraction peaks of the new phase are well indexed to the standard pattern of tetragonal Cu_{1.96}S (PDF 00-012-0224) (Fig. 3-29), which is the electrochemically active intermediate reported by others³⁷⁻³⁹.

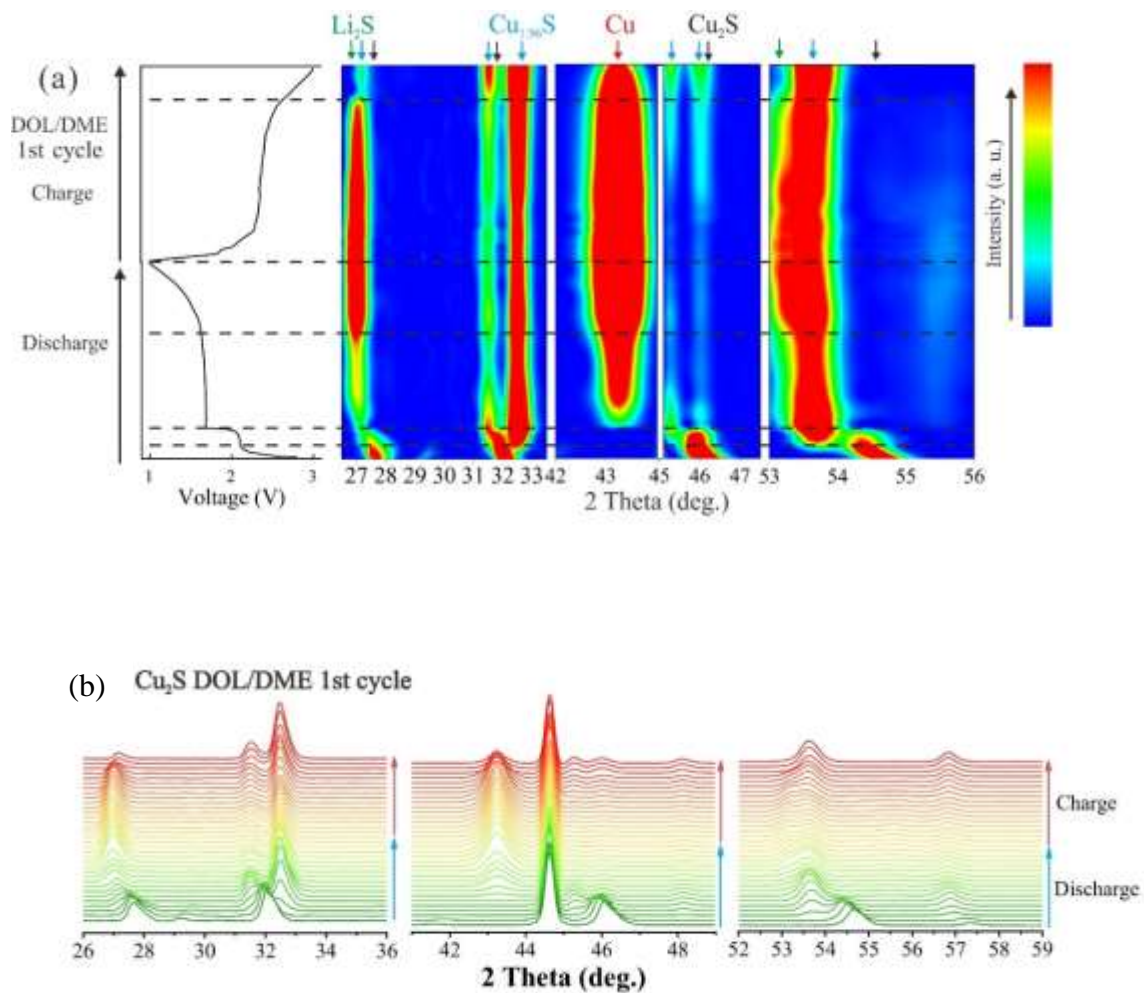


Figure 3-28. *Operando* XRD measurements and corresponding initial (dis)charge curves of Cu_2S in DOL/DME 1M LiPF_6 at 0.2 C. (a) contour plot, and (b) waterfall Plot

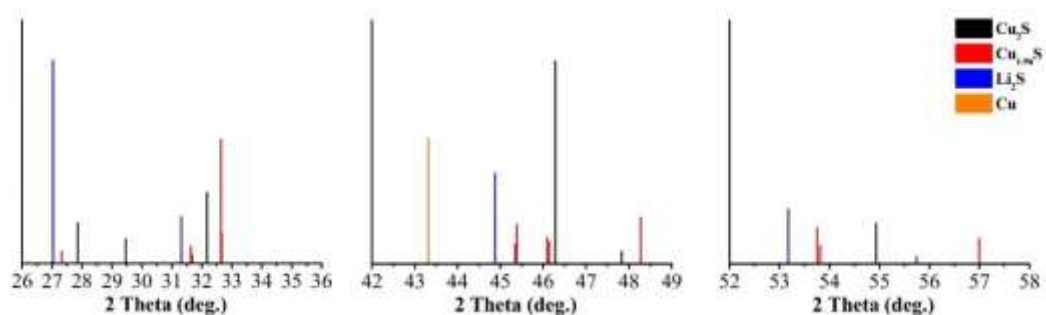


Figure 3-29. Standard patterns of Cu_2S (PDF 00-003-1071), $\text{Cu}_{1.96}\text{S}$ (PDF 00-012-0224), Li_2S (PDF 01-077-2145) and Cu.

To further verify the presence of $\text{Cu}_{1.96}\text{S}$, the Rietveld refinement analysis was performed on the fully charged Cu_2S in the DOL/DME electrolyte. The result is shown in Figure 30-3. The peaks associated with Al current collector and Cu residual were labeled with stars. It clearly shows that $\text{Cu}_{1.96}\text{S}$ is the final product in the DOL/DME electrolyte.

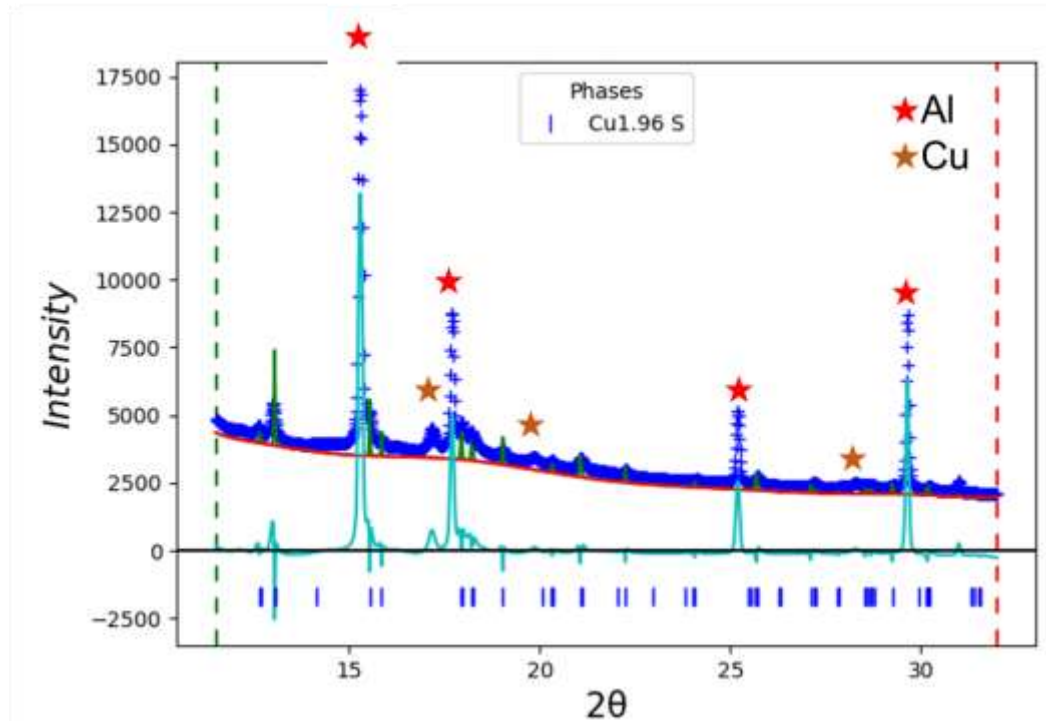


Figure 3-30. Rietveld refinement of the fully recharged copper sulfide in DOL/DME electrolyte. The XRD pattern was taken at an incident energy of 19.82 keV ($\lambda = 0.6246 \text{ \AA}$)

Previous publications have stated that the valence state of Cu in $\text{Cu}_{1.96}\text{S}$ is +1.⁴⁰⁻⁴¹ This statement was proved by XPS measurement of Cu 2p and S 2p binding energies. It was also stated that the valence state of Cu is +1 in all Cu_xS when $1.8 \leq x \leq 2$. The difference in Cu/S ratio between $\text{Cu}_{1.96}\text{S}$ and Cu_2S is due to their crystal structures: $\text{Cu}_{1.96}\text{S}$ has 8 $[\text{Cu}_{31}\text{S}_{16}]$ in the one-unit cell, and Cu_2S has 48 $[\text{Cu}_2\text{S}]$. Thus, even though $\text{Cu}_{1.96}\text{S}$ was formed in DOL/DME electrolyte, the reaction mechanism proposed here is charge and mass balanced. The Cu signal at 43.2° is detected at the beginning of the 1.7 V discharge plateau, and those of Li_2S (27° and 53.1°) are observed in the second half of the 1.7 V flat plateau, indicating the displacement

reaction of $\text{Cu}_{1.96}\text{S}$. During the charging process, the reverse reaction occurs, judging from the signals of Cu and Li_2S . Interestingly, at the fully charged state, the tetragonal $\text{Cu}_{1.96}\text{S}$ phase is regenerated instead of the pristine cubic Cu_2S phase. After 10 cycles, the electrochemical reactions between $\text{Cu}_{1.96}\text{S}$ and $\text{Li}_2\text{S}/\text{Cu}$ occur reversibly (Fig. 3-31).

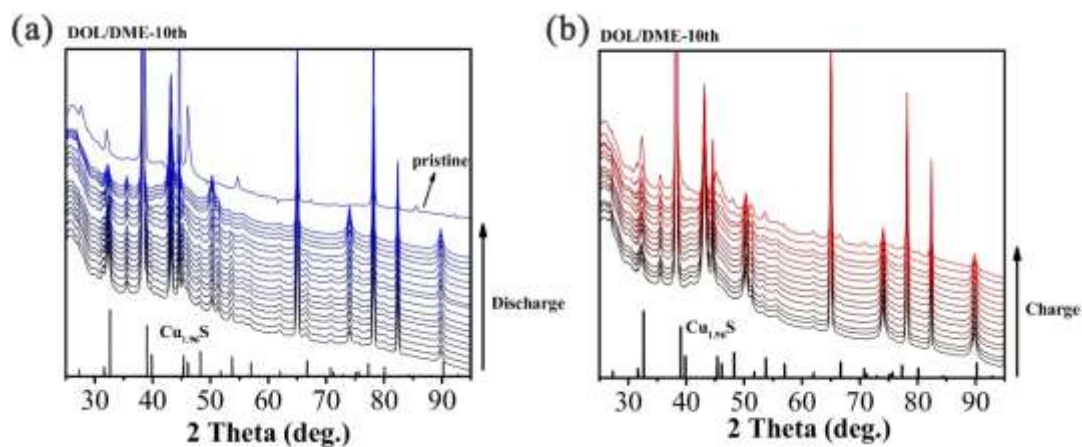


Figure 3-31. Waterfall operando XRD plots of Cu_2S in the 10th cycle in DOL/DME: (a) discharge and (b) charge processes.

During the initial discharge process in EC/DEC (Fig. 3-32), the Cu_2S experiences a similar discharge as DOL/DME, with the peak shifts and phase transformation to $\text{Cu}_{1.96}\text{S}$ discussed above. Nevertheless, when the battery was recharged to 2.5 V, both $\text{Cu}_{1.96}\text{S}$ and the cubic phase Cu_2S were observed, which is different from the behavior in DOL/DME. The weaker signals indicate a smaller amount of regenerated Cu_2S . In the 2nd cycle (Fig. 3-33), the transformation from cubic Cu_2S to tetragonal $\text{Cu}_{1.96}\text{S}$ continues, followed by reduction to Li_2S and Cu. In the fully recharged state, Cu_2S is again regenerated. This could result from side reactions of sulfide with the carbonate-

based electrolyte, which reduces the amount of sulfur participating in the recharge process. The XRD pattern of the Cu_2S electrode from the fully charged 'dead' cell (after 10 cycles, charged to 3 V, the ED/DEC electrolyte) (Fig. 3-34) exhibited the presence of Li_2S , Cu, and $\text{Cu}_{1.96}\text{S}$. Cu_2S peaks are missing in the pattern, ascribed to the higher energy barrier of the Cu_2S reformation processes in EC/DEC. Thus, with subsequent cycling, the amount of Cu_2S is regenerated reduced gradually. Though Li_2S , Cu, and $\text{Cu}_{1.96}\text{S}$ are electrochemically active, the cell cannot deliver any reversible capacity. The previous publications had studied the reactions of Cu_2S with carbonate-based electrolytes²¹⁻²². In the case of Cu_2S , the Cu_2S electrode from a 'dead' cell could still deliver some capacity after being rinsed with dimethyl sulfoxide (DMSO). This indicated that the activity of Cu_2S was hindered by the presence of side products on the surface, which was also shown by X-ray photoelectron spectroscopy (XPS) results.

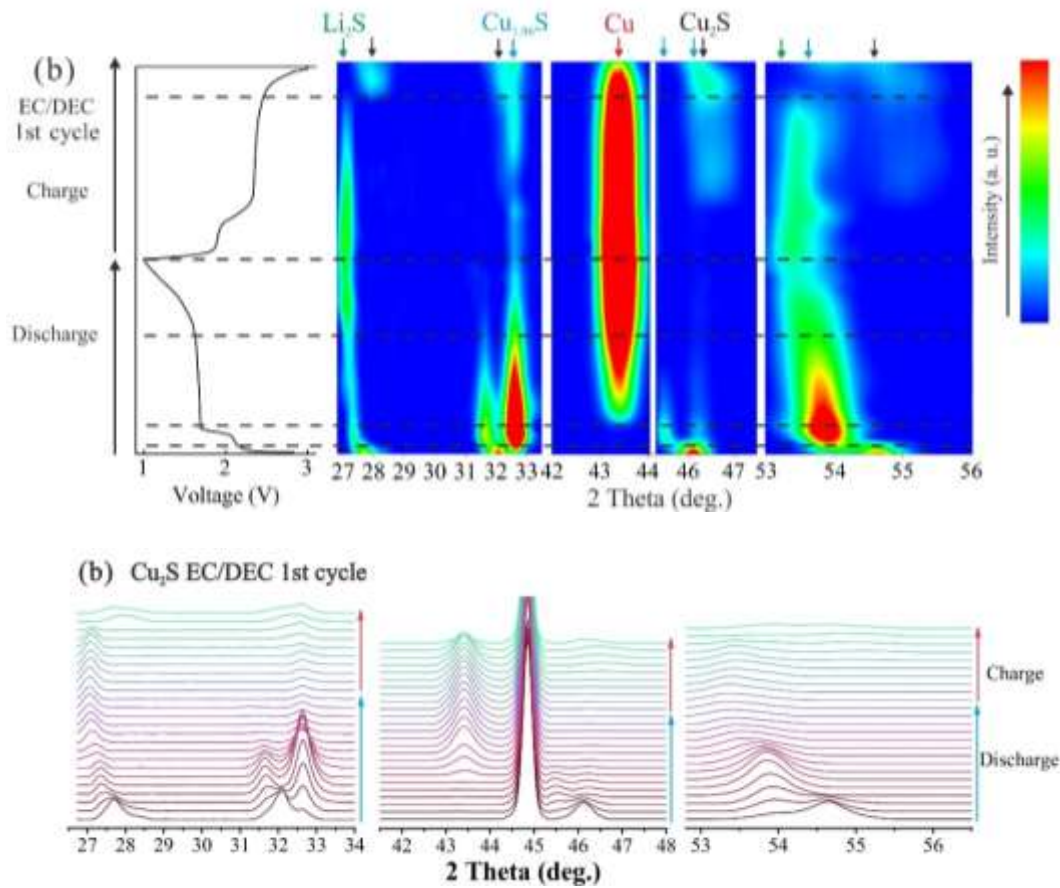


Figure 3-32. *Operando* XRD measurements and corresponding initial (dis)charge curves of Cu₂S in DOL/DME 1M LiPF₆ at 0.2 C. (a) contour plot, and (b) waterfall plot

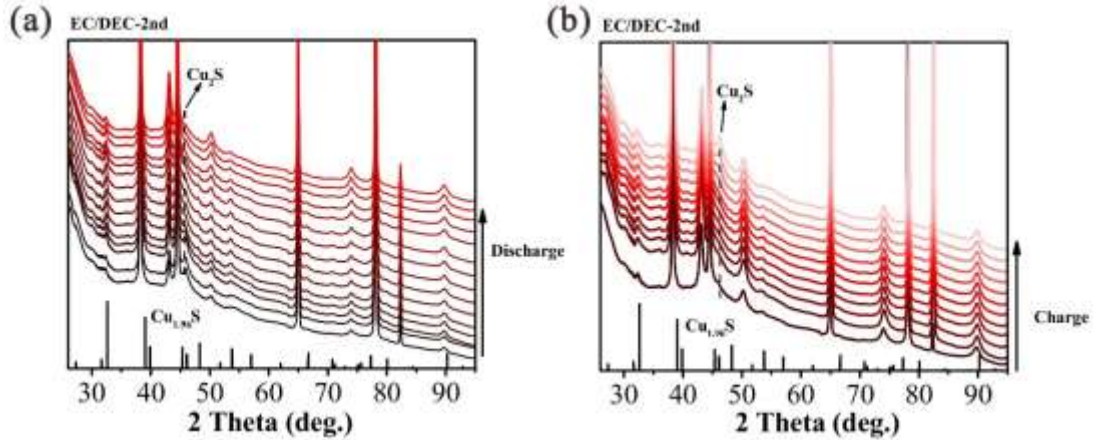


Figure 3-33. Waterfall operando XRD plots of Cu_2S in the 2nd cycle in EC/DEC: (a) discharge and (b) charge processes.

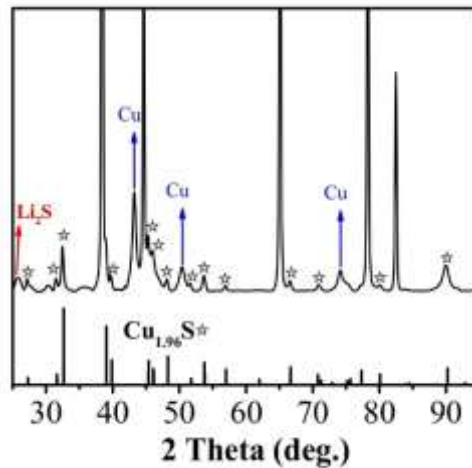


Figure 3-34. XRD pattern of the Cu_2S electrode from the 'dead' cell (after 10 cycles, fully charged to 3V, EC/DEC electrolyte).

To analyze the surface conditions of the Cu_2S electrode, *in situ* EIS tests were carried out. In DOL/DME (Fig. 3-35), the EIS profile is divided into two parts during discharge (Figs. 3-35 a-c). At the 2.1 V discharge plateau, the higher impedance is related to the lithiation process. The 1.7 V discharge plateau exhibits a smaller impedance, coinciding with the displacement reaction of the tetragonal $\text{Cu}_{1.96}\text{S}$.

During the recharge process, the impedance increases slightly. After 10 cycles (Figs. 3-35 d-f), although the impedance increases at certain stages, the 1.7 V plateau still exhibits a smaller impedance. When the cell is fully recharged, the spectrum recovered to that at the OCV in the 10th cycle.

In EC/DEC (Fig. 3-36), the spectra are dramatically different. The 2.1 V discharge plateau shows a lower impedance, while the impedances at the 1.7 V discharge plateau increase. When the cell is fully charged, the impedance is more significant, and after 10 cycles, it became more substantial.

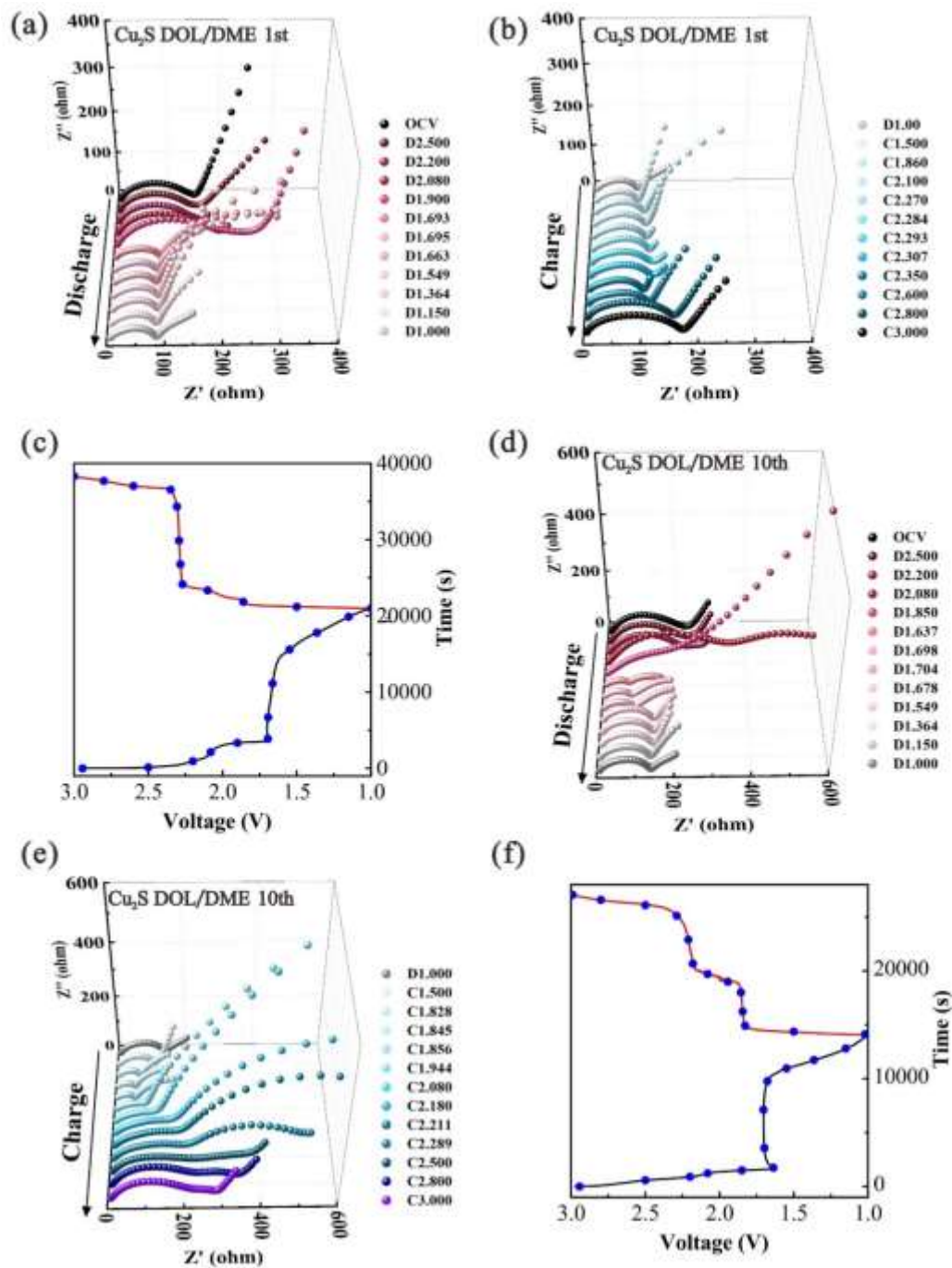


Figure 3-35. *In situ* EIS measurements and the corresponding (dis)charge profiles of Cu_2S in (a-c) the 1st and (d-f) the 10th cycle in DOL/DME.

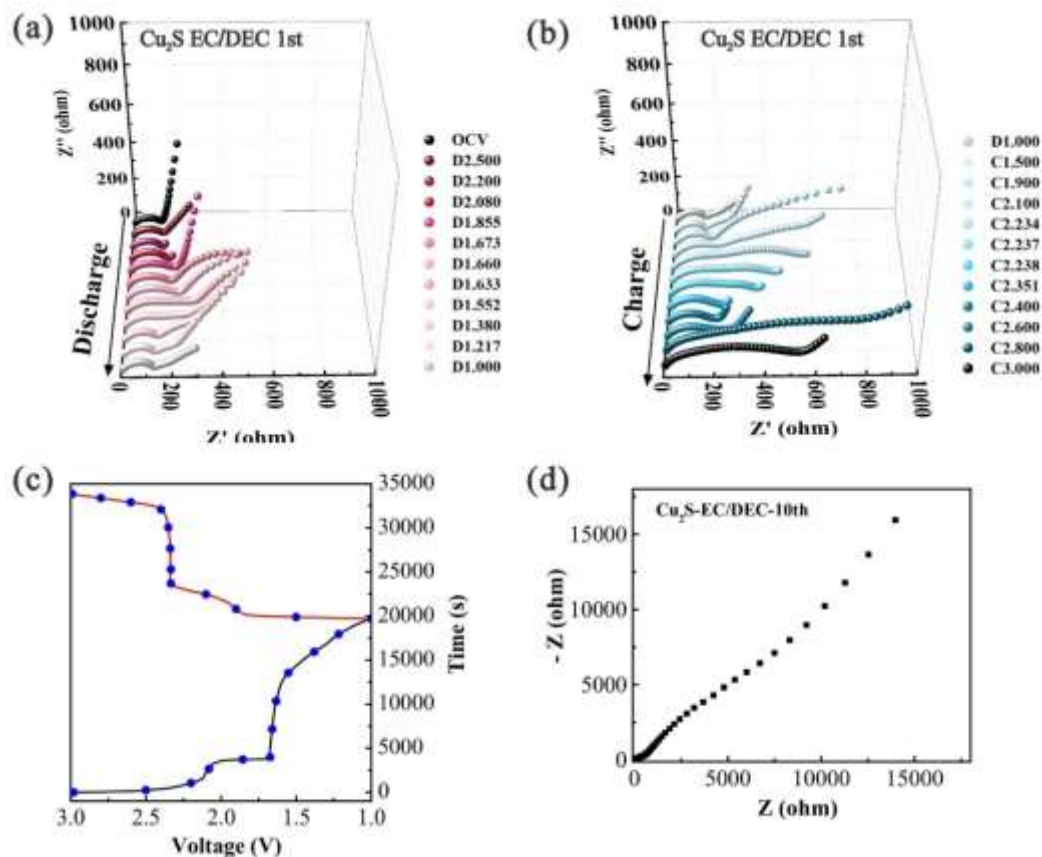


Figure 3-36. *In situ* EIS measurements and the corresponding (dis)charge profiles of Cu_2S in (a-c) the 1st and (d) the 10th cycle in EC/DEC.

Table 3-2. Apparent Li^+ diffusion coefficients (D_{Li^+}) of Cu_2S calculated from EIS (at fully charged state).

Cu_2S	$\text{Cu}_2\text{S}/\text{C}$			
	Slope	D_{Li^+} ($\text{cm}^2 \text{s}^{-1}$)	Slope	D_{Li^+} ($\text{cm}^2 \text{s}^{-1}$)
1st-DOL/DME	69.8	2.73 E-16	71.0	2.64 E-16
1st-EC/DEC	114	1.02 E-16	88.3	1.71 E-16
10th-DOL/DME	53.7	4.61 E-16	92.8	1.54 E-16
10th-EC/DEC	4.22E3	7.49 E-20	208	3.07 E-17

Based on the EIS results, the apparent lithium ions diffusion coefficients were calculated (Table 3-2)⁴²⁻⁴⁴. For Cu₂S, the diffusion coefficient barely changed in DOL/DME after 10 cycles, while it experienced a 10⁴-fold decrease in EC/DEC under otherwise identical conditions. These results also explain the failure of the cell. Based on previous and present results, it can be concluded that both side reactions and reaction pathways dramatically affect the reversibility of Cu₂S in ether- and carbonate-based electrolytes. In EC/DEC, Li₂S and Cu follow a more difficult reaction pathway to reform the cubic Cu₂S. Thus, it is difficult to maintain the sulfur array, leading to a loss in capacity. The side (decomposition) products cover the surface of the electrode, preventing further reaction. In DOL/DME, the structural similarity between the tetragonal Cu_{1.96}S and Li₂S ensures an excellent reaction reversibility.

3-3-4 Structural evolution and activation processes of $\text{Cu}_2\text{S}/\text{C}$ in EC/DEC electrolyte

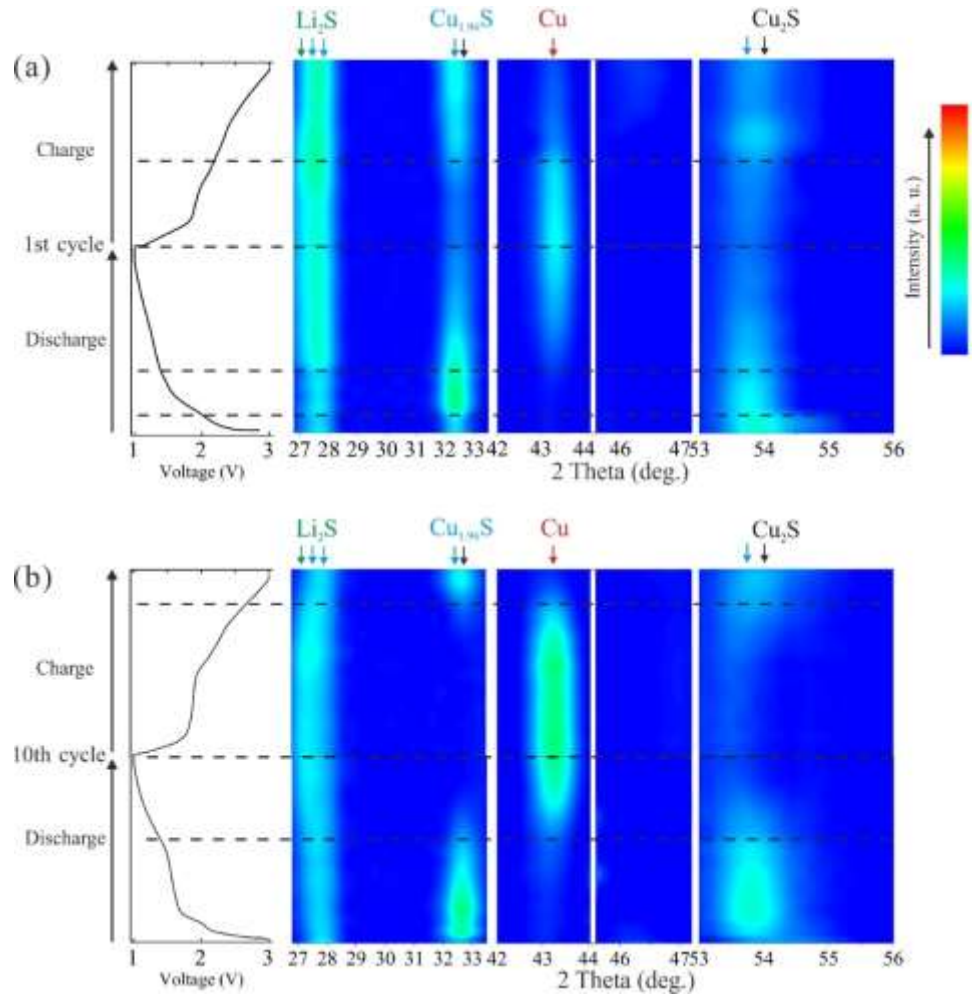


Figure 3-36. *Operando* XRD measurements and corresponding (dis)charge curves of $\text{Cu}_2\text{S}/\text{C}$ in the (a) 1st cycle and (b) 10th cycle in EC/DEC electrolytes with 1M LiPF_6 .

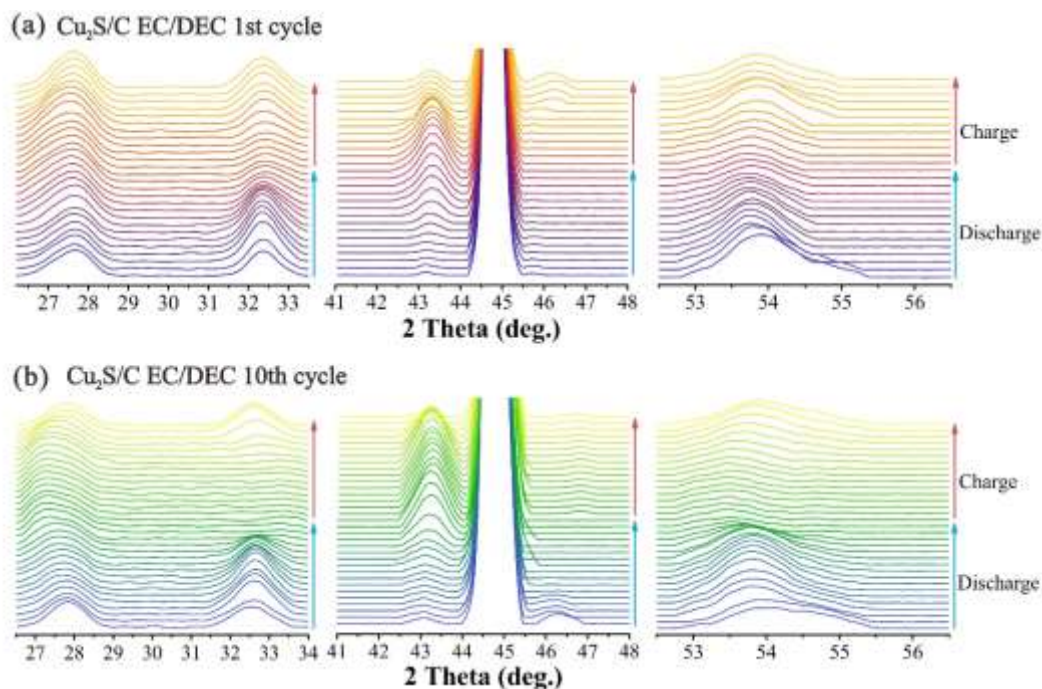


Figure 3-37. *Operando* XRD of Cu₂S/C in (a) the 1st and (b) the 10th cycle in the EC/DEC electrolyte.

Figs. 3-36 and 37 show the structural evolution of Cu₂S/C in the 1st and 10th cycles, respectively, in EC/DEC. During the initial discharge process, the peak at 32.1° intensifies. As discussed before, this peak is related to the emergence of the hexagonal phase Cu_{1.96}S. During continuous discharge, the peaks at 27.1° and 43.3°, ascribed to Li₂S and Cu respectively, indicate the displacement reaction ($\text{Cu}_{1.96}\text{S} + \text{Li} \rightarrow \text{Cu} + \text{Li}_2\text{S}$). During the initial charge process, the peaks associated with Cu and Li₂S lose intensity, while the peaks ascribed to Cu_{1.96}S intensify. However, closer inspection of the XRD profile indicated that not all the Cu_{1.96}S reacted in the first cycle, as suggested by the residual peak at 32.1° and the minimal peak shift at 43.3°. It may indicate that, in addition to the redox reaction of Cu₂S, side reactions, such as the lithiation of carbon, may also contribute to the battery's capacity.

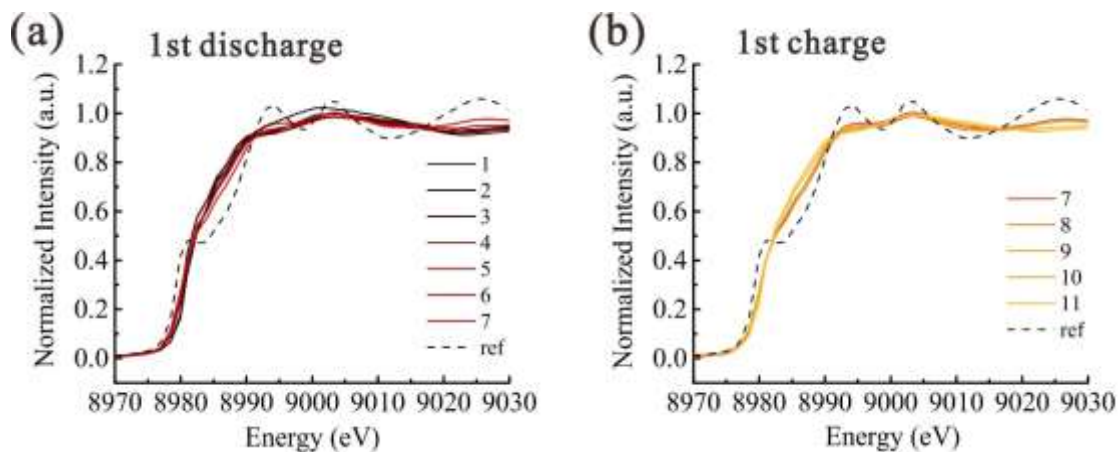


Figure 3-38. Operando XANES spectra of Cu₂S/C (a) discharge and (b) charge in EC/DEC.

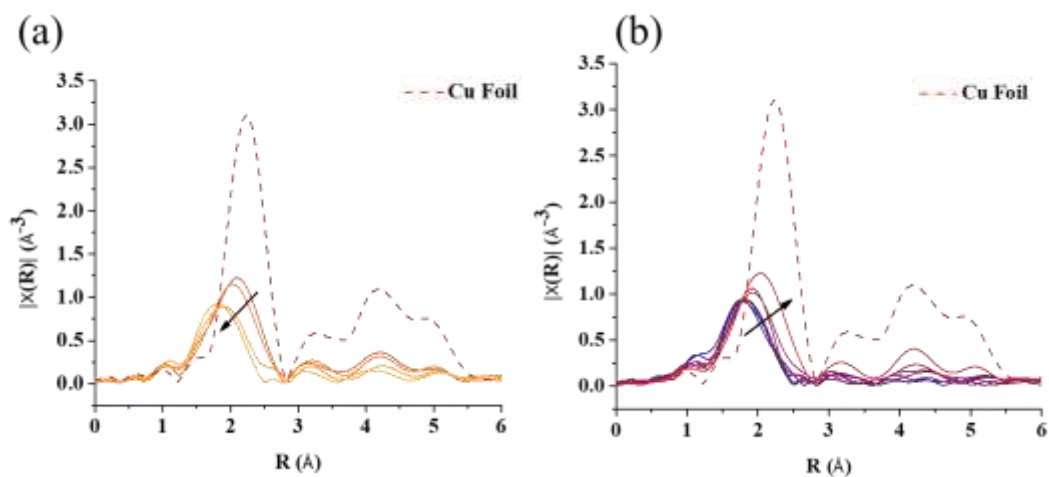


Figure 3-39. Operando EXAFS spectra of Cu₂S/C (a) discharge and (b) charge in EC/DEC.

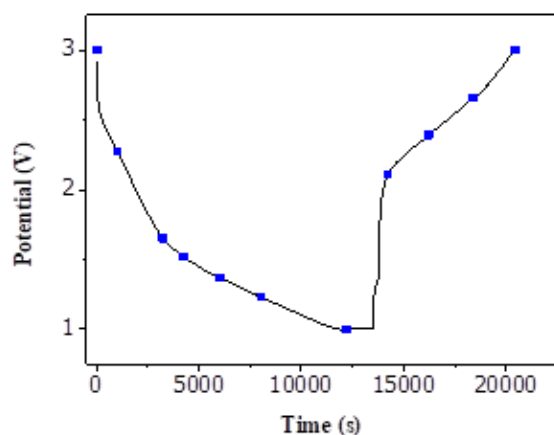


Figure 3-40. Charge/discharge profile of $\text{Cu}_2\text{S}/\text{C}$ in EC/DEC

This observation coincides with the slanted (dis)charge plateaus and the *operando* XAS spectra (Fig. 3-38 and 39), which suggest an incomplete reduction of Cu and is consistent with the apparent absence of isosbestic points. After 10 cycles (Fig. 3-36b), the increase in the peak intensity at 43.2° indicates the activation of $\text{Cu}_2\text{S}/\text{C}$, which can also be observed from the TEM images (Fig. 3-41).

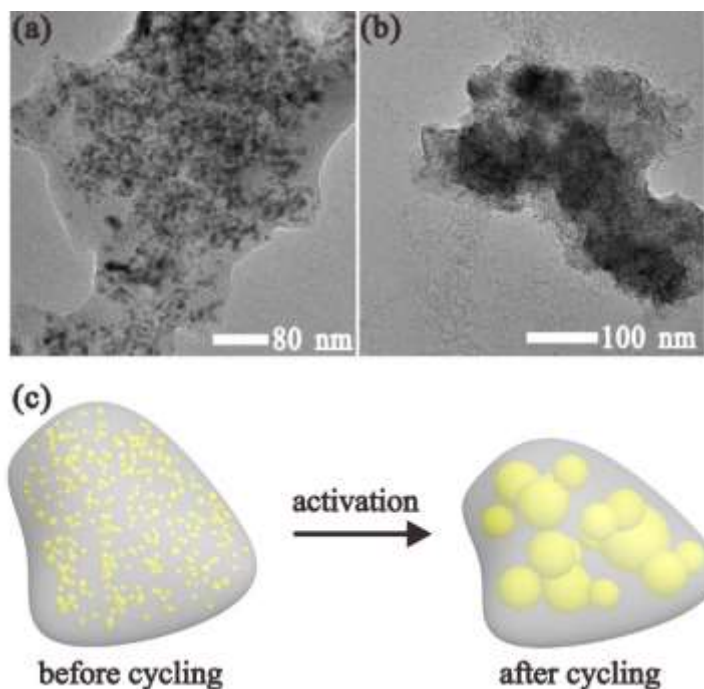


Figure 3-41. TEM images of $\text{Cu}_2\text{S}/\text{C}$ (a) before cycling, (b) after cycling, and (c) corresponding schematic.

When the cell is fully recharged, the emergence of peaks indexed to $\text{Cu}_{1.96}\text{S}$ demonstrates the reversible reaction of $\text{Cu}/\text{Li}_2\text{S}$ to $\text{Cu}_{1.96}\text{S}$. The behavior of $\text{Cu}_2\text{S}/\text{C}$ in EC/DEC is similar to that of Cu_2S in DOL/DME electrolytes. Additionally, the peak at 32.1° , associated with $\text{Cu}_{1.96}\text{S}$, disappears during discharge and reemerges at the end of the recharge, indicating a complete reaction of the active material at the 10th cycle. This, together with the more defined voltage plateaus and CV profiles (Fig. 3-42), demonstrates that $\text{Cu}_{1.96}\text{S}$ is the sole active material contributing to the battery capacity; hence the activation process of $\text{Cu}_2\text{S}/\text{C}$ is demonstrated. *Operando* XRD indicated that the amorphous carbon wrapping successfully hindered the structural decomposition and the loss of active material in EC/DEC electrolytes.

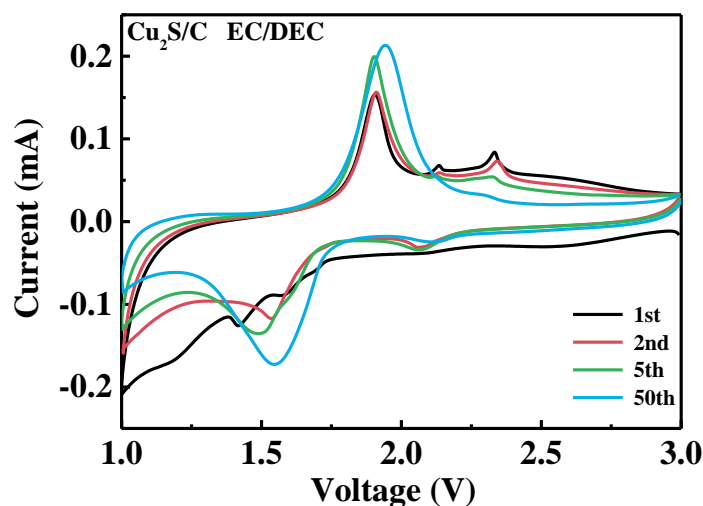


Figure 3-42. CV profiles of Cu₂S/C in EC/DEC.

In situ EIS measurements were also performed on Cu₂S/C. In DOL/DME (Fig. 3-43), the variation in the 1st cycle was similar to that in Cu₂S in DOL/DME (Fig. 3-35). After 10 cycles, the impedance decreased, in accordance with the activation process observed. It is noted that, in EC/DEC (Fig. 3-44), the change in the impedance in the 1st cycle was also similar to the stable impedance changes in DOL/DME (Fig. 3-43). At the fully charged stage, a dramatic increase in impedance, similar to the case of Cu₂S in EC/DEC (Fig. 3-36), was not observed. After 10 cycles, only minimal changes were noted in the EIS spectra suggesting a stable surface for the Cu₂S/C electrode, validating the effectiveness of the carbon coating. The lithium-ion diffusion coefficient was also determined for the Cu₂S/C composite showing an only 6-fold decrease in EC/DEC after 10 cycles when compared with the 10⁴-fold drop for Cu₂S without carbon protection (Table 3-2). The results, again, demonstrate the compatibility between Cu₂S/C and EC/DEC electrolytes, in which the carbon matrix

effectively hinders the surface reactions and helps retain the same reversible reaction pathways exhibited in DOL/DME electrolytes.

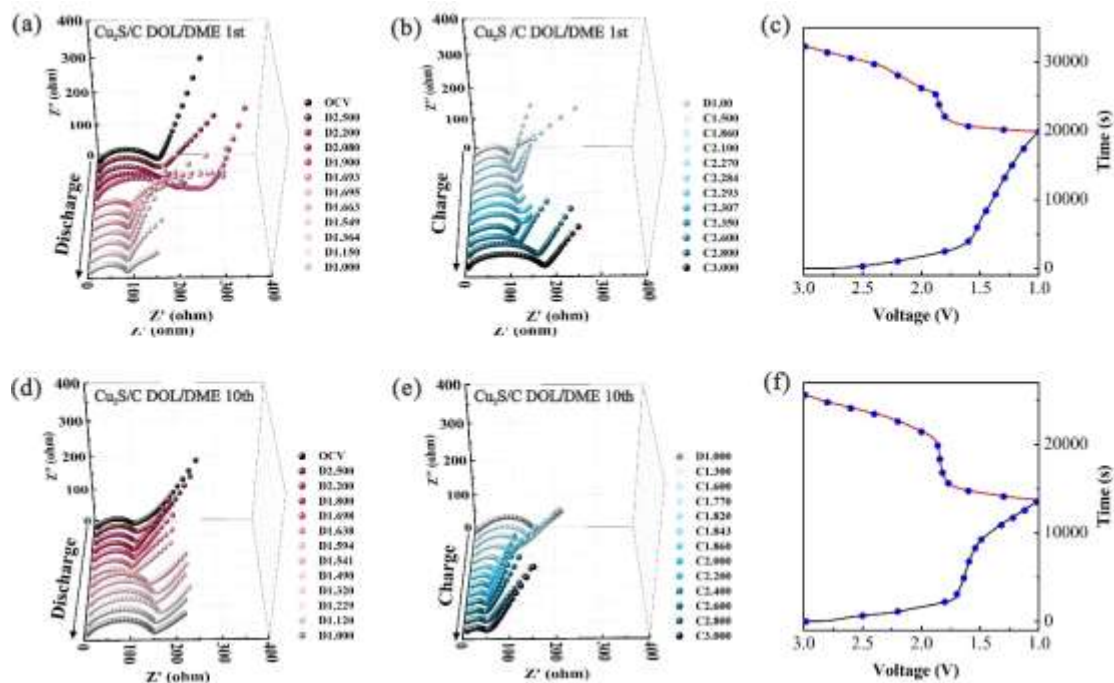


Figure 3-43. *In situ* EIS measurements and the corresponding (dis)charge profiles of $\text{Cu}_2\text{S}/\text{C}$ in (a-c) the 1st and (d-f) the 10th cycle in DOL/DME.

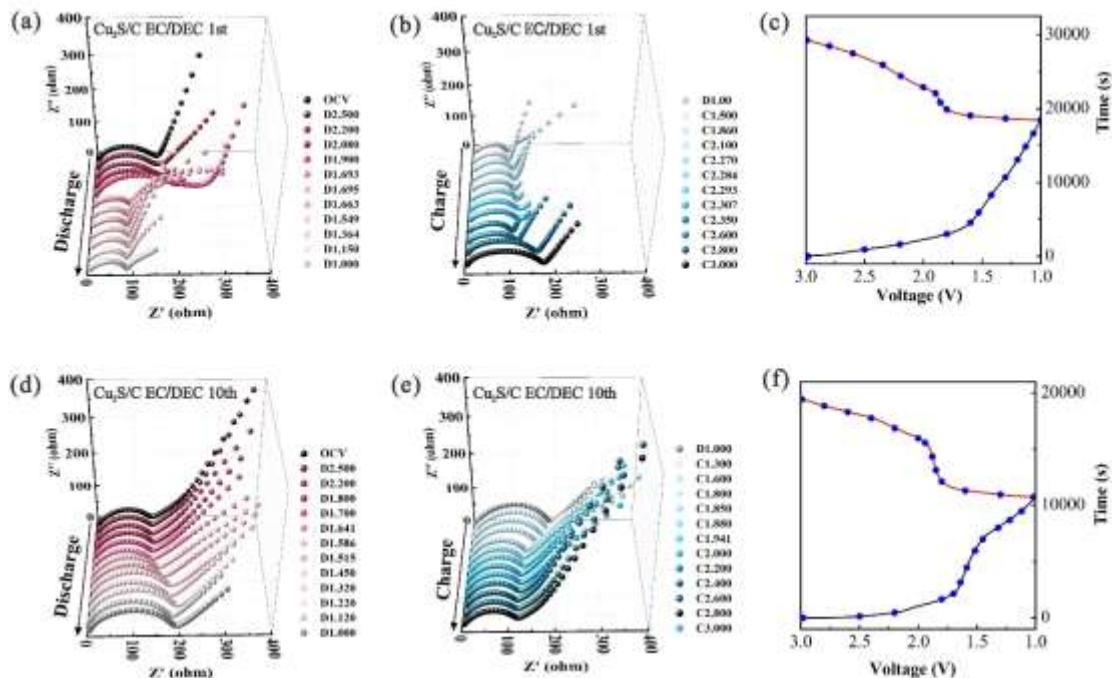


Figure 3-45. In situ EIS measurements and the corresponding (dis)charge profiles of $\text{Cu}_2\text{S}/\text{C}$ in (a-c) the 1st and (d-f) the 10th cycle in EC/DEC.

3-3-5 Electrochemical performance of a (-) $\text{Cu}_2\text{S}/\text{C}$ |1 M LiPF_6 in EC/DEC| LiCoO_2 (+) pouch cell

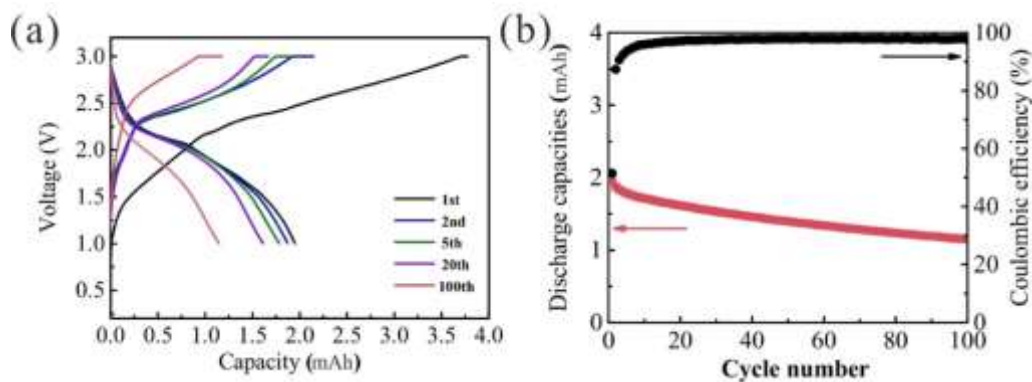


Figure 3-46. (a) Charge and discharge profiles and (b) cycling performance of the LiCoO_2 - $\text{Cu}_2\text{S}/\text{C}$ full cell at 100 mA g^{-1} (the capacity was calculated based on the mass of Cu_2S).

The *in-operando* X-ray analysis has provided a detailed understanding of the difference in the electrochemical performance of Cu_2S in the ether- and carbonate-based electrolytes. It provided a deeper and more fundamental understanding of the electrochemical behavior and provided insights for solving the mismatch between the Cu_2S and carbonate electrolytes, moving in a step forward towards a practical battery system. The strategy of forming $\text{Cu}_2\text{S}/\text{C}$ composite materials effectively hindered the loss of structural integrity and the side reactions between Cu_2S and carbonate-based electrolytes and thus maintained the highly reversible displacement reaction mechanism, which yielded excellent cycling performance. To further illustrate the viability of $\text{Cu}_2\text{S}/\text{C}$ composites in practical use, LiCoO_2 - $\text{Cu}_2\text{S}/\text{C}$ pouch full cells were assembled with EC/DEC as the electrolyte (Fig. 3-46). To the best of our knowledge, this is the first time that a full cell has been made by coupling Cu_2S as the anode with

a commercial LiCoO_2 cathode. It provided the basis for the industrial-scale applications of this material and battery systems. The initial charge capacity and initial coulombic efficiency (CE) were 3.79 mAh and 51%. The low initial CE is related to the properties of the amorphous carbon in $\text{Cu}_2\text{S}/\text{C}$, which can also be seen in the CE of $\text{Cu}_2\text{S}/\text{C}$ in half cells being only 68% (Fig. 3-8). The CE then quickly increased in the initial cycles and eventually stabilized at over 98%. The discharge capacities in the 2nd and 20th cycles were 1.87 and 1.61 mAh, respectively. After 100 cycles, a reversible capacity of 1.15 mAh was achieved, accompanied by a decay rate of 0.68% per cycle. Although the performance of the full cell should be further optimized, it has opened up a promising direction for a new lithium-ion battery system exhibiting low cost and good cyclability with high energy density for large-scale energy storage and sustainable energy conversion.

3-4. Conclusions

By employing *operando* synchrotron XRD and XAS techniques, the electrochemical reactions of Cu_2S in EC/DEC were more irreversible than in an ether-based electrolyte system (DOL/DME). This critical problem could be solved by an *in situ* carbon coating approach, in which a carbon matrix effectively hinders the deleterious surface reactions and retains the same reaction pathways in DOL/DME. These key findings provide deep insights into the different behaviors in different electrolyte systems and make the cuprous sulfide, or even other metal sulfides, potentially viable for commercial lithium-ion batteries. Based on these findings, we have, for the first time, successfully coupled a $\text{Cu}_2\text{S}/\text{C}$ composite anode with a LiCoO_2 cathode in a commercial carbonate-based electrolyte system (EC/DEC).

References:

- (1) Tarascon, J. M.; Armand, M. Issues and Challenges Facing Rechargeable Lithium Batteries. *Nature* 2001, 414, 359-367.
- (2) Schmuck, R.; Wagner, R.; Hörpel, G.; Placke, T.; Winter, M. Performance and Cost of Materials for Lithium-based Rechargeable Automotive Batteries. *Nat. Energy* 2018, 3, 267-278.
- (3) Kwade, A.; Haselrieder, W.; Leithoff, R.; Modlinger, A.; Dietrich, F.; Droeder, K. Current Status and Challenges for Automotive Battery Production Technologies. *Nat. Energy* 2018, 3, 290-300.
- (4) Cabana, J.; Monconduit, L.; Larcher, D.; Palacin, M. R. Beyond Intercalation-based Li-ion Batteries: The State of the Art and Challenges of Electrode Materials Reacting through Conversion Reactions. *Adv. Mater.* 2010, 22, E170-192.
- (5) Coughlan, C.; Ibanez, M.; Dobrozhan, O.; Singh, A.; Cabot, A.; Ryan, K. M. Compound Copper Chalcogenide Nanocrystals. *Chem. Rev.* 2017, 117, 5865-6109.
- (6) Li, X.; He, X.; Shi, C.; Liu, B.; Zhang, Y.; Wu, S.; Zhu, Z.; Zhao, J. Synthesis of One-Dimensional Copper Sulfide Nanorods as High-Performance Anode in Lithium Ion Batteries. *ChemSusChem* 2014, 7, 3328-3333.
- (7) Débart, A.; Dupont, L.; Patrice, R.; Tarascon, J. M. Reactivity of Transition Metal (Co, Ni, Cu) Sulphides Versus Lithium: The Intriguing Case of the Copper Sulphide. *Solid State Sci.* 2006, 8 (6), 640-651.
- (8) Jache, B.; Mogwitz, B.; Klein, F.; Adelhelm, P. Copper Sulfides for Rechargeable Lithium Batteries: Linking Cycling Stability to Electrolyte Composition. *J. Power Sources* 2014, 247, 703-711.

- (9) McDowell, M. T.; Lu, Z.; Koski, K. J.; Yu, J. H.; Zheng, G.; Cui, Y. In Situ Observation of Divergent Phase Transformations in Individual Sulfide Nanocrystals. *Nano Lett.* 2015, *15*, 1264-1271.
- (10) Han F.; Li W.; Li D.; Lu A. In Situ Electrochemical Generation of Mesoporous Cu₂S/C Composite for Enhanced Lithium Storage: Mechanism and Material Properties. *ChemElectroChem* 2014, *1*, 733-740.
- (11) Yuan T.; Tan, Z. P.; Ma, C. R.; Yang, J. H.; Ma, Z. F.; Zheng, S. Y. Challenges of Spinel Li₄Ti₅O₁₂ for Lithium-Ion Battery Industrial Applications. *Adv. Energy Mater.* 2017, *7*, 1601625(1)-1601625(25).
- (12) Shi, C.; Li, X.; He, X.; Zhao, J. New Insight into the Interaction between Carbonate-based Electrolyte and Cuprous Sulfide Electrode Material for Lithium Ion Batteries. *Electrochim. Acta* 2015, *174*, 1079-1087.
- (13) Meng X.; Riha S. C.; Libera J. A.; Wu Q.; Wang, H.-H.; Martinson, A. B. F.; Elam, J. W. Tunable Core-shell Single-walled Carbon Nanotube-Cu₂S Networked Nanocomposites as High-performance Cathodes for Lithium-ion Batteries. *J. Power Sources* 2015, *280*, 621-629.
- (14) Kalimuldina G.; Taniguchi, I. Synthesis and Electrochemical Characterization of Stoichiometric Cu₂S as Cathode Material with High Rate Capability for Rechargeable Lithium Batteries. *J. Power Sources* 2016, *331*, 258-266.
- (15) Kalimuldina, G.; Taniguchi, I. High Performance Stoichiometric Cu₂S Cathode on Carbon Fiber Current Collector for Lithium Batteries. *Electrochimica Acta.* 2017, *224*, 329-336.
- (16) Yu, S. H.; Feng, X.; Zhang, N.; Seok, J.; Abruna, H. D. Understanding

- Conversion-Type Electrodes for Lithium Rechargeable Batteries. *Acc. Chem. Res.* 2018, *51*, 2, 273-281.
- (17) Wang, Y.; Zhang, Y.; Li, H.; Peng, Y.; Li, J.; Wang, J.; Hwang, B. J.; Zhao, J. Realizing High Reversible Capacity: 3D Intertwined CNTs Inherently Conductive Network for CuS as an Anode for Lithium Ion Batteries. *Chem. Eng. J.* 2018, *332*, 49-56.
- (18) Ravel, B.; Newville, M. ATHENA, ARTEMIS, HEPHAESTUS: Data Analysis for X-ray Absorption Spectroscopy Using IFEFFIT. *J. Synchrotron Radiat.* 2005, *12*, 537-541.
- (19) Toby, B. H.; Von Dreele, R. B. GSAS-II: the Genesis of a Modern Open-source All Purpose Crystallography Software Package. *J. Appl. Crystallogr.* 2013, *46*, 544-549.
- (20) Carne-Sanchez, A.; Imaz, I.; Cano-Sarabia, M.; Maspoeh, D. A Spray-drying Strategy for Synthesis of Nanoscale Metal-organic Frameworks and Their Assembly into Hollow Superstructures. *Nat. Chem.* 2013, *5*, 203-211.
- (21) Li, H.; Wang, Y.; Huang, J.; Zhang, Y.; Zhao, J. Microwave-assisted Synthesis of CuS/Graphene Composite for Enhanced Lithium Storage Properties. *Electrochim. Acta.* 2017, *225*, 443-451.
- (22) Hu, H.; Cheng, H.; Liu, Z.; Li, G.; Zhu, Q.; Yu, Y. In Situ Polymerized PAN-Assisted S/C Nanosphere with Enhanced High-Power Performance as Cathode for Lithium/Sulfur Batteries. *Nano Lett.* 2015, *15*, 8, 5116-5123.
- (23) Zhang, Y.; Li, K.; Huang, J.; Wang, Y.; Peng, Y.; Li, H.; Wang, J.; Zhao, J. Preparation of Monodispersed Sulfur Nanoparticles-partly Reduced Graphene

- Oxide-polydopamine Composite for Superior Performance Lithium-sulfur Battery. *Carbon* 2017, *114*, 8-14.
- (24) Hurma, T.; Kose, S. XRD Raman Analysis and Optical Properties of CuS Nanostructured Film. *Opt.-Int. J. Light & Electron Opt.* 2016, *127*,15, 6000-6006.
- (25) He, S.; Wang, G.-S.; Lu, C.; Luo, X.; Wen, B.; Guo, L.; Cao, M.-S. Controllable Fabrication of CuS Hierarchical Nanostructures and Their Optical, Photocatalytic, and Wave Absorption Properties. *ChemPlusChem* 2013, *78*, 3, 250-258.
- (26) Gao, J.; Lowe, M. A.; Kiya, Y.; Abruña, H. D. Effects of Liquid Electrolytes on the Charge–Discharge Performance of Rechargeable Lithium/Sulfur Batteries: Electrochemical and in-Situ X-ray Absorption Spectroscopic Studies. *J. Phys. Chem. C* 2011, *115*,50, 25132-25137.
- (27) Yim, T.; Park, M.-S.; Yu, J.-S.; Kim, K. J.; Im, K. Y.; Kim, J.-H.; Jeong, G.; Jo; Y. N.; Woo, S.-G.; Kang; K. S.; Lee, I.; Kim, Y.-J. Effect of Chemical Reactivity of Polysulfide Toward Carbonate-based Electrolyte on the Electrochemical Performance of Li–S Batteries. *Electrochim. Acta.* 2013, *107*, 454-460.
- (28) Li, X.; He, X.; Shi, C.; Liu, B.; Zhang, Y.; Wu, S.; Zhu, Z.; Zhao, J. Synthesis of One-Dimensional Copper Sulfide Nanorods as High-Performance Anode in Lithium Ion Batteries. *ChemSusChem* 2014, *7*, 3328-3333.
- (29) Yang, Y.; Zheng, G.; Misra, S.; Nelson, J.; Toney, M. F.; Cui, Y. High-capacity Micrometer-sized Li₂S Particles as Cathode Materials for Advanced Rechargeable Lithium-ion Batteries. *J. Am. Chem. Soc.* 2012, *134*,37, 15387-15394.
- (30) Wang, X.; Wang, Y.; Li, X.; Liu, B.; Zhao, J. A Facile Synthesis of Copper Sulfides Composite with Lithium-storage Properties. *J. Power Sources* 2015, *281*,

185-191.

- (31) Cheng, J.; Pan, Y.; Zhu, J.; Li, Z.; Pan, J.; Ma, Z. Hybrid Network CuS Monolith Cathode Materials Synthesized via Facile in Situ Melt-diffusion for Li-ion Batteries. *J. Power Sources* 2014, *257*, 192-197.
- (32) Kumar, P.; Nagarajan, R.; Sarangi, R. Quantitative X-ray Absorption and Emission Spectroscopies: Electronic Structure Elucidation of Cu₂S and CuS. *J. Mater. Chem.* 2013, *1*, 2448-2454.
- (33) Wang, Q.; Hanson, J. C.; Frenkel, A. I. Solving the Structure of Reaction Intermediates by Time-resolved Synchrotron X-ray Absorption Spectroscopy. *J. Chem. Phys.* 2008, *129*, 234502-234507.
- (34) Klysubun, W.; Thongkam, Y.; Pongkrapan, S.; Won-in, K.; T-Thienprasert, J.; Dararutana, P. XAS Study on Copper Red in Ancient Glass Beads from Thailand. *Anal Bioanal Chem* 2011, *399*, 9, 3033-3040.
- (35) Greaves, G. N.; Durham, P. J.; Diakun, G.; Quinn, P. Near-edge X-ray Absorption Spectra for Metallic Cu and Mn. *Nature* 1981, *294*, 139-142.
- (36) Rothe, J.; Hormes, J.; Bönemann, H.; Brijoux, W.; Siepen, K. In Situ X-ray Absorption Spectroscopy Investigation during the Formation of Colloidal Copper. *J. Am. Chem. Soc.* 1998, *120*, 24, 6019-6023.
- (37) Chung, J. S.; Sohn, H. J. Electrochemical Behaviors of CuS as a Cathode Material for Lithium Secondary Batteries. *J. Power Sources* 2002, *108*, 1, 226-231.
- (38) Yamakawa; N.; Jiang, M.; Grey, C. P. Investigation of the Conversion Reaction Mechanisms for Binary Copper (II) Compounds by Solid-State NMR Spectroscopy and X-ray Diffraction. *Chem. Mater.* 2009, *21*, 14, 3162-3176.

- (39) Kalimuldina, G.; Taniguchi, I. Electrochemical Properties of Stoichiometric CuS Coated on Carbon Fiber Paper and Cu Foil Current Collectors as Cathode Material for Lithium batteries. *J. Mater. Chem. A* 2017, 5, 15, 6937-6946.
- (40) Patel, T. A.; Panda, E. Copper Deficiency Induced Varying Electronic Structure and Optoelectronic Properties of Cu_{2-x}S Thin Films. *Appl. Surf. Sci.* 2019, 488, 477-484.
- (41) Qiu, P.; Zhu, Y.; Qin, Y.; Shi, X.; Chen, L. Electrical and Thermal Transports of Binary Copper Sulfides Cu_xS with X from 1.8 to 1.96. *APL Materials* 2016, 4, 10, 104805(1)-104805(8).
- (42) You, Y.; Yao, H. R.; Xin, S.; Yin, Y. X.; Zuo, T. T.; Yang, C. P.; Guo, Y. G.; Cui, Y.; Wan, L. J.; Goodenough, J. B. Subzero-Temperature Cathode for a Sodium-Ion Battery. *Adv. Mater.* 2016, 28, 33, 7243-7248.
- (43) Yuan, Z.; Peng, H. J.; Hou, T. Z.; Huang, J. Q.; Chen, C. M.; Wang, D. W.; Cheng, X. B.; Wei, F.; Zhang, Q. Powering Lithium-Sulfur Battery Performance by Propelling Polysulfide Redox at Sulfiphilic Hosts. *Nano Lett.* 2016, 16, 1, 519-527.
- (44) Wang, X.; Hao, H.; Liu, J.; Huang, T.; Yu, A. A Novel Method for Preparation of Macroporous Lithium Nickel Manganese Oxygen as Cathode Material for Lithium Ion Batteries. *Electrochim. Acta* 2011, 56, 11, 4065-4069.

CHAPTER 4

AN OPERANDO X-RAY ABSORPTION SPECTROMETRY STUDY OF THE INTERACTION BETWEEN COS₂ HOST AND SULFUR CATHODE IN LITHIUM-SULFUR BATTERIES

4-1 Introduction

Lithium-sulfur batteries are among the most promising electrical energy storage systems for the next generation high capacity batteries. Their high theoretical capacity of 1675 mAh/g and energy density of 2600 Wh/kg are more than ten times higher than current lithium-ion batteries.^{1,2} Moreover, sulfur is highly affordable, as it is one of the most abundant elements on earth and a main byproduct of the oil industry. Last year, a ton of pure sulfur cost only \$40. As a cathode material this represents a great advantage, especially considering that the price of cobalt was about \$51,000/ton.

However, several drawbacks are hindering the commercialization of lithium-sulfur batteries. First, sulfur has a very low conductivity of 5×10^{-30} S/cm, which significantly increases the electrical resistance of the battery system. Second, reducing sulfur to lithium sulfide involves a significant volumetric expansion of 80% that can damage the electrode structure and the cell configuration overall. Third, the reaction intermediates of lithium-sulfur batteries, lithium polysulfides, are highly soluble in the electrolyte. The dissolved polysulfides shuttle between the cathode and the anode, react with the electrolytes and form a passivation layer on both electrodes. This causes

a loss of active materials and increases overall cell impedance. This phenomenon is called the polysulfide shuttling effect.¹⁻⁵

To mitigate the severeness of the polysulfide shuttling, polar materials such as metal oxides and metal sulfides have been used as the sulfur host in the cathode for their ability to adsorb polysulfides through polar-polar interactions. Our group has previously developed a MOF-derived CoS₂ host to capture the sulfur within a conductive hybrid framework, preventing the lithium polysulfides from diffusing into the electrolyte while facilitating the redox reactions. The following section represents a continuation of work of the MOF-CoS₂ project, for which operando X-ray absorption spectroscopy was used to investigate the interaction between the sulfur and the CoS₂ host.

4-2 Experimental Methods

4-2-1. Li-S battery preparation with MOF-derived CoS₂/S composite

The electrode film was provided by Dr. Na Zhang. The electrode contained 80% active material (MOF-CoS₂/S composite), 15% Super P, and 5% polyvinylidene fluoride (PVDF). The sulfur content in the composite was about 40%. The X-ray coin cell was assembled in an Ar-filled glovebox with lithium metal as the anode and Celgard 2325 as the separator. 1.0 M lithium bis(trifluoromethane)sulfonamide (LiTFSI) in a mixed solvent of 1,3-dioxolane (DOL) and 1,2-dimethoxyethane (DME) (1:1, v:v) was used as the electrolyte.

4-2-2. Electrochemical methods

The operando battery was galvanostatically discharged/charged at a C-rate of 0.1C from 3V to 1.7 V (vs. Li/Li⁺), using a Biologics SP-200 potentiostat, when the operando X-ray measurements were carried out. The pristine cell was allowed to rest for 3 hours before each operando measurement. The 5-cycled sample was pre-cycled in our lab using the same current density and potential range. The cell was then held at 3V (vs. Li/Li⁺) after four cycles and before being brought to the synchrotron for operando measurements. The exhausted battery was cycled 50 times in our lab, held at 3V (vs. Li/Li⁺), and tested ex-situ at the synchrotron.

4-2-3. Operando X-ray absorption spectroscopy measurements.

Co K-edge X-ray absorption spectroscopy (XAS) was performed at beamline C-1 of the Cornell High Energy Synchrotron Source (CHESS). The spectra were collected in transmission mode from 100 eV below the edge to $k=12$ above the edge. A Co foil was placed between ion chambers, and its spectrum was collected concurrently with the battery cell. This foil spectrum was then used to calibrate the energy and served as the metal standard. XANES (X-ray Absorption Near-Edge Structure) spectra were calibrated and normalized with the ATHENA software package.⁶ Fourier transformed EXAFS (Extended X-ray Absorption Fine Structure) spectra were obtained by applying a Hanning window from 2.5 to 11 \AA^{-1} with k^2 -weighting in ATHENA and fitted with standard CoS_2 standard crystal structure from 1.25 to 5 \AA using the ARTEMIS package.

4-3. Results And Discussion

The MOF-derived CoS₂/S developed in our group has shown excellent battery performance.⁷ It can achieve a reversible capacity of 800 mAh/g over 150 cycles at 0.2C and 600 mAh/g over 1000 cycles at 1C. It was clear that incorporating CoS₂ in the composite successfully alleviated the shuttling effects of lithium polysulfides.

Using operando X-ray methods, we were able to further investigate the interaction between the lithium polysulfides and CoS₂ host by tracking the atomic movement in CoS₂ during charging and discharging of the battery.

Operando X-ray absorption spectroscopy measurements were conducted on a freshly assembled MOF-CoS₂/S cell, the cell after five cycles, and the cell after 50 cycles. The results from the fresh cell are presented first.

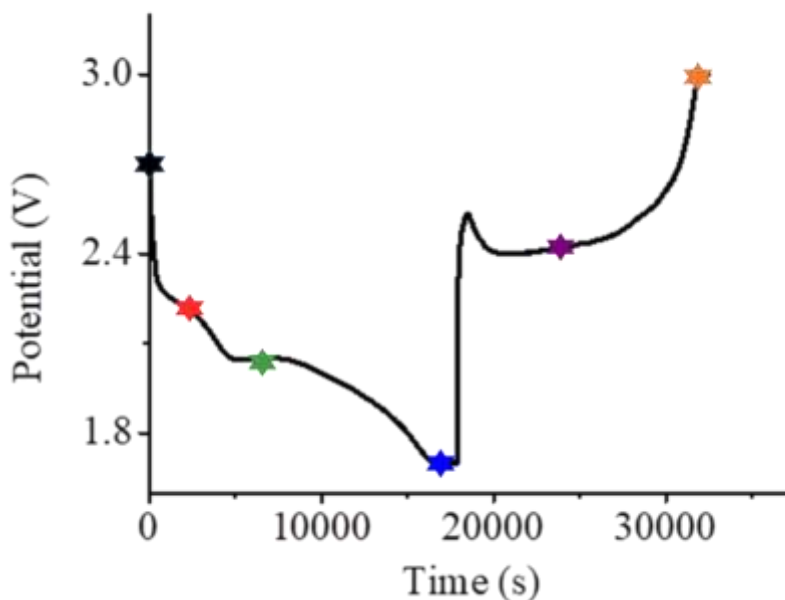


Figure 4-1. The 1st charge/discharge profile for the pristine cell. XAS spectra used in the EXAFS analysis were chosen at the stated state of charge.

As shown in figure 4-1, the cell has two discharge plateaus, 2.2 V and 2V, corresponding to the reduction from solid S₈ to liquid long-chain lithium polysulfides and from long-chain polysulfides to short-chain polysulfides, respectively. At 1.7V, solid lithium sulfide was formed. In the recharge process, the large potential spike indicates an activation barrier from lithium sulfide to short-chain lithium polysulfides, followed by the formation of long-chain lithium polysulfides and eventually elemental sulfur.⁸

Five XAS spectra at different states of charge were chosen for the EXAFS analysis. We did not observe any changes in the XANES spectra, which was expected as CoS₂ was not involved in the Li-S redox reactions. Each spectrum was fitted using CoS₂ as the standard (ICSD 86351). An example of a fitted spectrum is shown in fig. 4-2

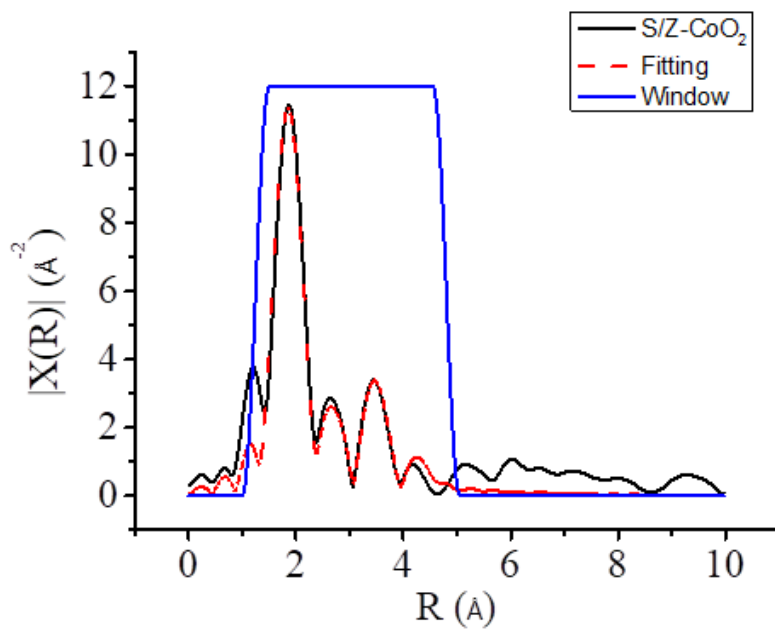


Figure 4-2, EXAFS profile and fitting results for S/Z-CoO₂ electrode in the pristine state. The fitting was performed within a Hanning window between 1.25 and 4.8 Å.

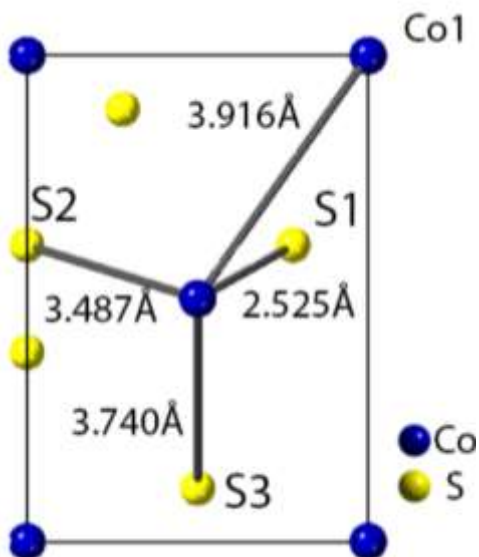


Figure 4-3. Crystal structure of CoS₂. The theoretical atomic distances between the core Co atom and its neighboring atom are listed next to the corresponding bonds.

Table 4-1. EXAFS fitting results of the pristine MOF-CoS₂/S in DOL/DME electrolyte

Scattering path	R	Debye-Waller factor
S1.1	2.2632	0.0074
S1.2	3.51043	0.00873
S1.3	3.76469	0.00873
Co1.1	3.87841	0.01954

*Atomic distances shown here are before phase correction.

The R-values in table 4-1 are bond distance estimations between a core Co atom and the neighboring atoms listed under the scattering path column, illustrated in figure 4-3.

The same EXAFS analysis was conducted for all five operando spectra. The fitting

results from each spectrum were then plotted over the battery charge and discharge profile, shown in figure 4-4, to relate the changes in Co bond distances with the battery potentials.

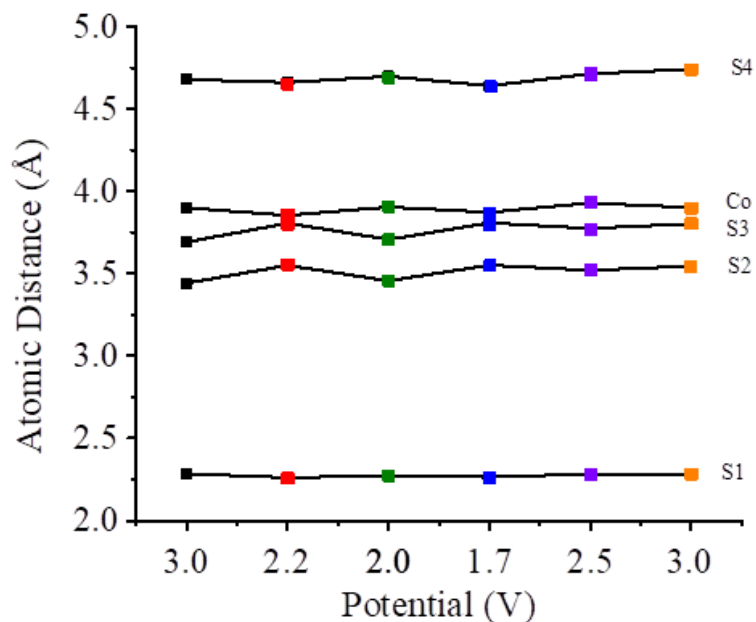


Figure 4-4. Changes in atomic distances between core Co atom and the specified neighboring atom at different states of charge.

As presented in Fig. 4-4, the changes in the bond distance between the core Co atoms and their surrounding atoms was minimal in the first cycle, across all states of charges. This suggested that the interaction between the CoS_2 host and the L-S compounds was relatively weak. The cyclability testing of this composite using normal coin cells was presented in our previous publication.⁷ The results are presented in figure 4-5. It was observed that the cell capacity of this S/Z- CoS_2 composite (red) decreased

significantly from the first cycle to the second cycle, at both 0.2C and 1C. This suggested that an activation process occurred in cycle 1 to initiate the interaction between CoS_2 and lithium polysulfides.

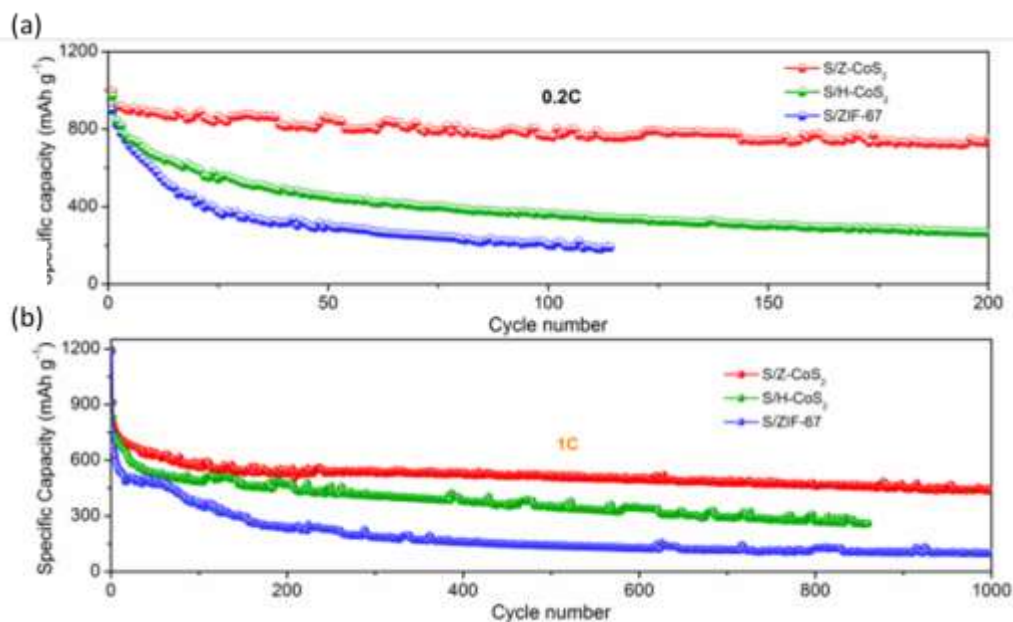


Figure 4-5, (a) Cycling performance of S/Z-CoS₂, S/H-CoS₂, and S/ZIF-67 at 0.2 C for 200 cycles. (b) Long-term cycling of S/Z-CoS₂, S/H-CoS₂, and S/ZIF-67 at 1 C for 1000 cycles.⁷

The cell performance was stabilized after cycle 2. To ensure CoS_2 was fully activated during the time of operando measurements, a new coin cell was pre-cycled in the lab for four cycles before bringing it to the synchrotron for the fifth cycle. The charge/discharge profile and the band distance plot are shown in figures 4-6 and 4-7

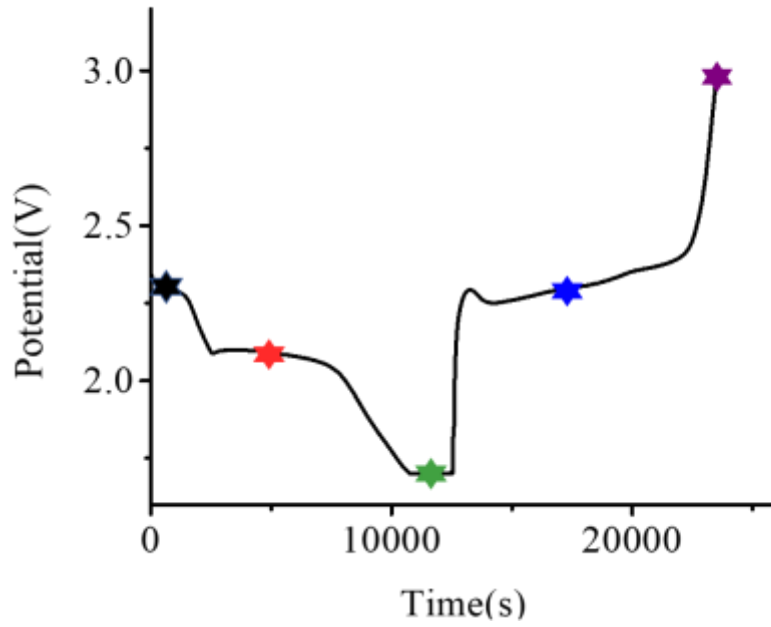


Figure 4-6. The 5th charge/discharge profile from the S/Z-CoS₂ cell. XAS spectra used in the EXAFS analysis were chosen at the stated state of charge.

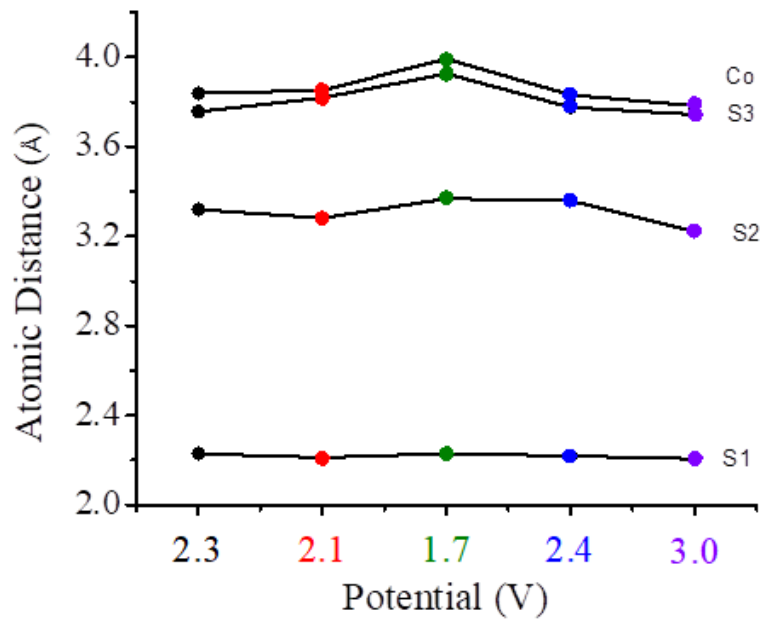


Figure 4-7. The changes in atomic distances between the core Co atom and the specified neighboring atoms, at different states of charge after 5 cycles at 0.1C.

Unlike the first cycle results (Fig. 4-5), a distinct trend of bond distance variations was observed. When the battery was discharged from 2.3 V to 1.7V, the bond distance Co-S3 and Co-Co increased by approximately 0.2 Å. This increase in bond distance was accompanied by the sulfur reduction from elemental S to long-chain polysulfides, short-chain polysulfides, and, eventually, lithium sulfide, as suggested by the discharge/charge profile. Chen et al. had employed density functional theory (DFT) calculations to investigate the interaction of various Li_xS_n species with a MnO_2 (100) surface.⁹ Their calculations shows that elemental S_8 has the weakest binding energy with the MnO_2 surface. The binding energy increased as the S was reduced to polysulfides and reached a maximum with Li_2S . Their DFT calculations explained the observation illustrated in figure 4-7. When the cell was discharged from 2.3V to 1.7V, the binding energy between Li-S species and CoS_2 increased. This enhanced binding energy elongated the bond distance of Co and S within CoS_2 . When the battery was recharged, the Li_2S was re-oxidized to S, the binding energy decreased, and thus the bond distances between Co and its neighboring atoms relaxed to their original state. It was also noticed that the bond length between the core Co and its closest S atoms (Co-S1) did not vary as a function of potential. This may be due to the fact that the Co-S1 bond is very strong and the interaction from the Li-S complex was not robust enough to affect it. Overall, our operando XAS measurement successfully described the interaction between lithium polysulfide and CoS_2 , demonstrating its effectiveness as a sulfur host and alleviating the polysulfide shuttling phenomena.

The ex-situ spectrum of the S/Z- CoS_2 cell, after 50 cycles, was also collected. The obtained spectrum was plotted together with that of the pristine cell and the cell after 5

cycles. As presented in Fig. 4-8, the edge energy after 50 cycles was slightly lower than those of the pristine state, and after 5 cycles, indicating a drop in Co oxidation state. The whiteline feature of the 50-cycle cell was also smeared, possibly due to structural damage of the MOF morphology after extensive cycling. These may be the two main causes that lower the effectiveness of CoS_2 over time.

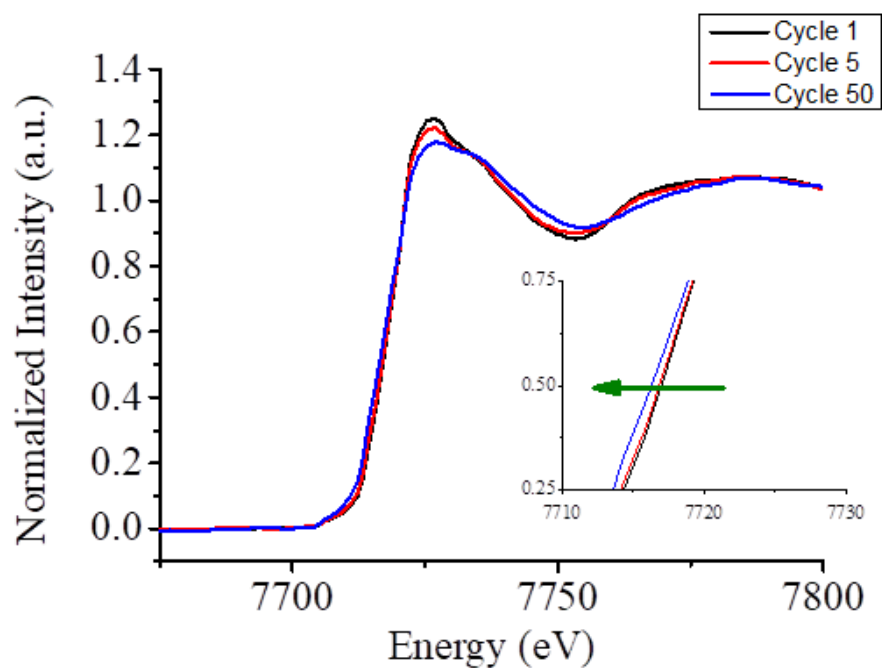


Figure 4-8. XANES spectra of the MOF- CoS_2 /S cell at Co k-edge, at the pristine state, after 5 cycles and after 50 cycles.

4-4 Conclusions

A MOF-derived CoS_2/S composite has been shown to be an excellent cathode material for lithium-sulfur batteries. CoS_2 , acting as the host for elemental sulfur, mitigated the effects of the polysulfide shuttling effects and enhanced the cyclability of the sulfur cathode. The interactions between/among the CoS_2 and Li-S species were characterized by operando X-ray absorption spectroscopy. Using EXAFS analysis, the interactions between the lithium polysulfides and CoS_2 were captured. The strong binding energy between the short-chain lithium polysulfides and CoS_2 elongated the bond distance between Co and its neighboring atoms as the battery was discharged. When the cell was recharged, the Co-S bond returned to its original value. As the battery was continuously cycled, Co was reduced, and the MOF-derived CoS_2 gradually lost its morphology, resulting in a diminution in its ability to attract and bind polysulfides.

References

- (1) Manthiram, A.; Fu, Y.; Chung, S. H.; Zu, C.; Su, Y. S. Rechargeable Lithium-Sulfur Batteries. *Chemical Reviews*. 2014, pp 11751–11787.
- (2) Eftekhari, A.; Li, X.; Mai, L.; Wang, C.; Miao, L.; Zhu, K.; Chi, Z.; Ke, F.; Yang, Y.; Wang, A.; Wang, W. How Far Away Are Lithium-Sulfur Batteries From Commercialization? *Frontiers in Energy Research* | www.frontiersin.org **2019**, 7 (123), 123.
- (3) Seh, Z. W.; Sun, Y.; Zhang, Q.; Cui, Y. Designing High-Energy Lithium-Sulfur Batteries. *Chemical Society Reviews* **2016**, 45 (20), 5605–5634.
- (4) Bruce, P. G.; Freunberger, S. A.; Hardwick, L. J.; Tarascon, J. M. LiO₂ and LiS Batteries with High Energy Storage. *Nature Materials* **2012**, 11 (1), 19–29.
- (5) Evers, S.; Nazar, L. F. New Approaches for High Energy Density Lithium Sulfur Battery Cathodes. *Accounts of Chemical Research* **2012**, 46 (5), 1135–1343.
- (6) Ravel, B.; Newville, M. ATHENA, ARTEMIS, HEPHAESTUS: Data Analysis for X-Ray Absorption Spectroscopy Using IFEFFIT. *Journal of Synchrotron Radiation* **2005**, 12 (4), 537–541.
- (7) Zhang, N.; Yang, Y.; Feng, X.; Yu, S. H.; Seok, J.; Muller, D. A.; Abruña, H. D. Sulfur Encapsulation by MOF-Derived CoS₂ Embedded in Carbon Hosts for High-Performance Li-S Batteries. *Journal of Materials Chemistry A* **2019**, 7 (37), 21128–21139.
- (8) Lim, W. G.; Kim, S.; Jo, C.; Lee, J. A Comprehensive Review of Materials with Catalytic Effects in Li–S Batteries: Enhanced Redox Kinetics. *Angewandte Chemie - International Edition* **2019**, 58 (52), 18746–18757.

(9) Wang, X.; Li, G.; Li, J.; Zhang, Y.; Wook, A.; Yu, A.; Chen, Z. Structural and Chemical Synergistic Encapsulation of Polysulfides Enables Ultralong-Life Lithium-Sulfur Batteries. *Energy and Environmental Science* **2016**, 9 (8), 2533–2538.

CHAPTER 5

A COIN-CELL BASED DIFFERENTIAL ELECTROCHEMICAL MASS SPECTROMETRY (DEMS) CELL FOR GAS GENERATION EVALUATION OF LITHIUM-ION BATTERIES

5-1. Introduction

Since its first introduction in 1991 by Sony, lithium-ion batteries (LIB) are considered the most promising energy storage devices on the market and have been widely applied in numerous electronic devices such as cell phones, laptops, and others. LIBs outperform other battery systems for its volumetric energy and power densities, ideal operation voltage, good cyclability, low self-discharge rate, and low maintenance.¹⁻⁴ In the past decade, due to the excessive consumption of fossil fuels and the requirement of CO₂ emissions reduction, the main application of lithium-ion batteries has changed from small electronic devices to electric vehicles (EVs). To meet the EVs' long driving range demand, many high-capacity LIB electrode materials have been developed, including nickel-rich lithium nickel manganese cobalt oxide (NMC) and lithium nickel cobalt aluminum oxide (NCA).⁵⁻⁸ Compared to traditional lithium cobalt oxide, these new nickel-rich cathode materials have a higher energy density, higher operating voltage, and longer cycle life. Though we have seen promising performance from these high-capacity electrode materials, the challenging battery

operating conditions in EVs require higher safety standards for newly developed battery materials. This is a particular challenge to nickel-rich cathode materials, as lithium nickel oxide is notorious for its thermal instability.⁹

Thermal runaway and gassing are the two major contributors to the safety concerns in lithium-ion batteries, especially under abusive operation conditions like overcharge, high temperature, or cell deformation.¹⁰ Gas evolution in lithium-ion batteries is generally caused by the decomposition of electrolyte solvent, side reactions between solvent and the lithium salt, and the phase/structure transformations from the cathode material. Hydrogen, oxygen, and flammable organic products such as ethylene are among the gaseous species generated from the abovementioned reactions and increase the chances to onset thermal runaway reactions in some cases.¹¹⁻¹³ In addition, the cell volume expansion, caused by gassing behavior, increases the pressure accumulated within the battery and negatively impacts the electrode stability and electrolyte displacement, reducing battery cycle life and shelf life. Therefore, it is essential for all newly designed battery materials for us to understand their gassing mechanisms under normal and abusive operation conditions.

Differential electrochemical mass spectrometry (DEMS) is an excellent technique for identifying and quantifying gaseous evolution. It combines an electrochemical cell with a mass spectrometer and allows for the *operando* measurement of volatile gaseous products generated by electrochemical reactions. The intensity change in mass fragment signals is measured as a function of time and potential. DEMS has been

widely applied to investigate the gassing behavior of lithium-ion battery materials.^{14–}
¹⁷ Our group has previously used DEMS to examine the CO₂ and O₂ evolution of high
voltage cathode materials.¹⁸ The Novak group has studied oxygen, hydrogen,
ethylene, and CO₂ evolution in batteries.¹⁹ Brezesinski et al. also used DEMS to
identify the role of lithium nitrate in gas evolution in lithium-sulfur batteries.²⁰ All of
these studies have revealed valuable insights into the gas evolution reactions from
various battery systems. However, the DEMS battery cell used in virtually all of these
studies is far from the natural operation conditions of batteries. Brezesinski's group
used a modified Swagelok cell, while Novak used a modified cell based on headspace
analysis. They all require a carrier gas and the utilization of a free-standing electrode
or having the electrode cast directly on the DEMS cell body.

This study introduces our newly developed coin cell-based DEMS cell, using our
three-electrode DEMS cell as the base. It greatly approximates the actual battery
operation conditions and provides more accurate information about electrode redox
reactions and electrolyte decomposition. Moreover, this new DEMS cell enables the
measurement of gas evolution at elevated temperatures, providing more significant
insights into the battery materials employed in EVs.

5-2. Experimental Section

5-2-1 Chemicals

Lithium cobalt (III) oxide (99.8%), lithium titanate (battery grade), lithium acetate dihydrate (BioUltra, >99.0%), manganese (II) acetate tetrahydrate (99+%), nickel(II)acetate tetrahydrate ($\geq 99.0\%$), Brij®58 (Mn~1124), 1-methyl-2-pyrrolidinone (anhydrous, 99.5%), and lithium hexafluorophosphate solution in ethylene carbonate and diethyl carbonate (1M LiPF₆ in EC/DEC=50/50 (v/v), battery grade) were purchased from Aldrich Chemical Company. Cobalt (II) acetate tetrahydrate (98%) was from Alfa Aesar Chemicals. Nitric acid (GR ACS) was from EMD Millipore Corporation. Citric acid anhydrous (Certified ACS) was from Fisher Scientific. Super P Li conductive carbon black was from TIMCAL. Kynar polyvinylidene fluoride (PVDF) was from Arkema.

5-2-2 Synthesis of LiNi_{0.6}Mn_{0.2}Co_{0.2}O₂ (NMC622)

NMC622 was prepared following a previous publication.²¹ Stoichiometric amounts of lithium acetate dihydrate (10% extra), cobalt acetate tetrahydrate, manganese acetate tetrahydrate, and nickel acetate tetrahydrate were dissolved in 50ml distilled water, resulting in a 0.03 mol of NMC solution. 50ml of Brij®58 in ethanol (0.02M) were then added to the NMC solution. The resulting solution was mixed drop-wisely with 100 ml of 0.006M citric acid ethanol solution. Nitric acid was used to adjust the pH of the final solution to 1. The mixture was then aged at 150C for 2hr, dried in an oven at 120C until a foamed gel was formed. The gel was then heated to 250C for 6hrs followed by 6 hrs at 300C, resulting in an NMC622 precursor. The final NMC622

particles were obtained by heating the precursor in an oven using the following

temperature program: room temperature $\xrightarrow{2\text{ }^\circ\text{C}/\text{min}}$ 400°C (150 min) $\xrightarrow{2\text{ }^\circ\text{C}/\text{min}}$ 750°C (600 min) $\xrightarrow{2\text{ }^\circ\text{C}/\text{min}}$ 950°C $\xrightarrow{-6\text{ }^\circ\text{C}/\text{min}}$ 600°C $\xrightarrow{\text{furnace cooling}}$ Room temperature. The resulting

NMC622 material was confirmed to be single phase by powder XRD using a Rigaku Ultima IV diffractometer at a scan rate of 2° /min at 0.02° steps from 10° to 80°.

5-2-3 Battery preparation

LiCoO₂ (LCO) and NMC 622 electrodes were made by casting a slurry of 85 wt.% of active material, 10 wt.% super P conductive carbon, and 5 wt.% PVDF in 1-methyl-2-pyrrolidinone (NMP) on a porous Al current collector (TOB New Energy Technology). The Li₄Ti₅O₁₂ (LTO) electrode was prepared using a slurry that was 80 wt.% active material, 15 wt.% super P, and 5wt. % PVDF in NMP and cast on a porous Cu current collector. The prepared electrode films were dried in a vacuum oven overnight at 120°C to remove NMP solvent. 200uL of 1M LiPF₆ in EC/DEC electrolyte were added to each coin cell. Glass fiber filter paper GF/F (Whatman) was used as the separator.

5-2-4 Differential Electrochemical Mass Spectrometry

A quadrupole differential electrochemical mass system (HiQuad quadrupole mass spectrometer system, Pfeiffer Vacuum) with two differentially pumped chambers, an RF generator (QMH 400-1, Pfeiffer Vacuum), a controller (QMS 700, Pfeiffer Vacuum), and a secondary electron multiplier SEM detector (EP422, Pfeiffer

Vacuum) were used in this work. The main and mass spectrometric analysis chambers were pumped by two turbopumps (TMU 261, TMU071, Pfeiffer), controlled by two turbopump controllers (TC600, TC100, Pfeiffer), respectively. A rotary vane vacuum pump (DUO 10M, Pfeiffer) connected the two turbopumps served as a backup vacuum system.

5-2-5. The design of coin cell battery-based DEMS electrochemical cell

As illustrated in Fig. 5-1, the coin cell battery-based DEMS cell consists of a Kel-F (Polychlorotrifluoroethylene) top, a rubber gasket, two layers of Teflon film, one layer of FEP film, and a stainless-steel base with a frit. Two pieces of copper tape were used as the current collectors. The Kel-F top secured the coin cell against the stainless-steel base while supporting the current collector. The rubber gasket was used to seal the gap between the Kel-F body and the coin cell. The Teflon and the FEP membranes were used to prevent potential liquid electrolytes from leaking into the mass spectrometer. The stainless-steel base, together with the frit, allowed the gas generated/evolved within the battery to enter the mass spectrometer. The entire set-up was placed under an argon environment and allowed to rest for 1 hour before each DEMS experiment. In the case of measurements at elevated temperatures, a heating belt (OMEGA) and a voltage controller were used to adjust/control the temperature.

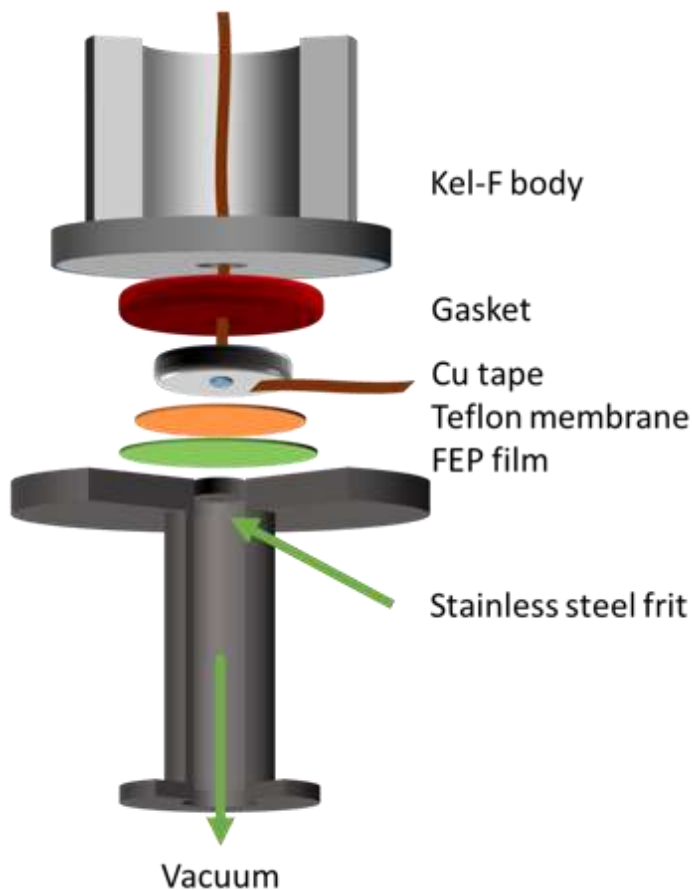


Figure 5-1. Schematic diagram of the coin cell-based DEMS measurement cell. The cell was placed in an argon environment. For measurements at 45°C, a heating tape was used to wrap the cell, and a voltage controller was used to control the temperature.

5-2-6 Design of DEMS modified coin cell case

The DEMS coin cell was modified from commercial CR2032 cases from MTI instruments. As shown in figure 5-2a, a 3-mm diameter hole was drilled in the center of the cathode casing. A nickel foam disk with a thickness of 1 mm was firmly pressed against the inner side of the cathode casing using a hydraulic press to cover the hole, achieving a flat surface at the outside of the case. (fig. 5-3) The porous nickel foam

was further sealed by a Teflon membrane and torr seal epoxy from the inside, and left overnight before using, allowing the epoxy to cure.

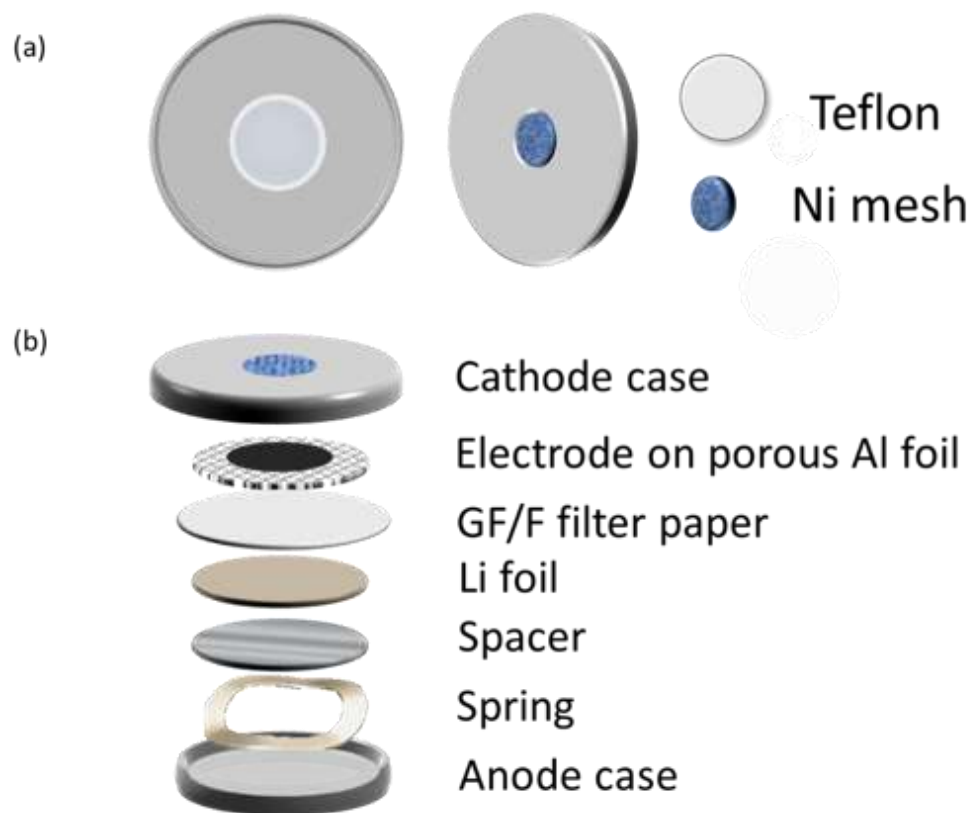


Figure 5-2. (a) Schematic diagram of the modified coin cell cathode case. (b) Diagram of cell components in the DEMS coin cell.



Figure 5-3. Picture of the DEMS coin cell cathode case

5-2-7 Electrochemical measurements:

Cyclic voltammetry tests were conducted with a potentiostat (EG&G Princeton Applied Research, Model 173) and a universal programmer (EG&G PARC, model 175). A scan rate of 0.5mV/s was applied from 3 to 5V.

5-3. Results and Discussion

5-3-1. Choice of electrode materials

To examine the validity of this coin cell configuration, we chose three electrode materials, lithium cobalt oxide (LCO), lithium nickel manganese cobalt oxide (NMC622), and lithium titanate (LTO) pairing with metallic lithium as the counter electrode and 1 M LiPF₆ in EC/DEC (50:50, v:v) as electrolyte. These three electrode materials are commercialized and widely used in current lithium-ion battery

applications. During lithium-ion battery operation, the evolution of gaseous products generated at cathode, anode, and electrolyte decomposition were measured simultaneously while a cyclic voltammetry test was run on the battery.

The lithium cobalt oxide and lithium titanate were used as received without further purification. NMC 622 was synthesized using the sol-gel method following a sintering process. The XRD pattern of the synthesized NMC622 materials in a range of 10 – 80° is presented in Fig. 5-4. It matched well to the NMC622 reference (ICSD:104731) with the α -NaFeO₂ structure and R-3m space group. The splitting of the (006)/(102) and (108)/(110) reflections at 38° and 65°, respectively, indicated that the synthesized NMC622 had a highly crystallized layered structure.²² The ratio of I(003)/I(104) serves as an indication of cation mixing in the lattice of NMC materials, and a ratio >1.2 reflects a low level of cation mixing.²³ The I(003)/I (104) ratio of this sample was 1.32. The SEM image (Fig. 5-5) showed that the synthesized NMC 622 particles had a smooth particle surface with a 0.2-0.5 μ m size distribution.

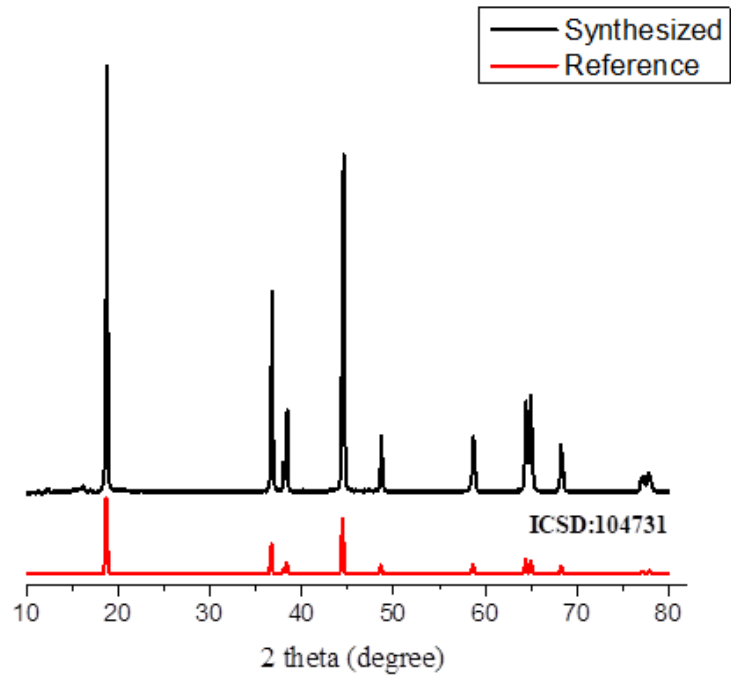


Figure 5-4. XRD pattern of the synthesized NMC 622 cathode and the corresponding reference

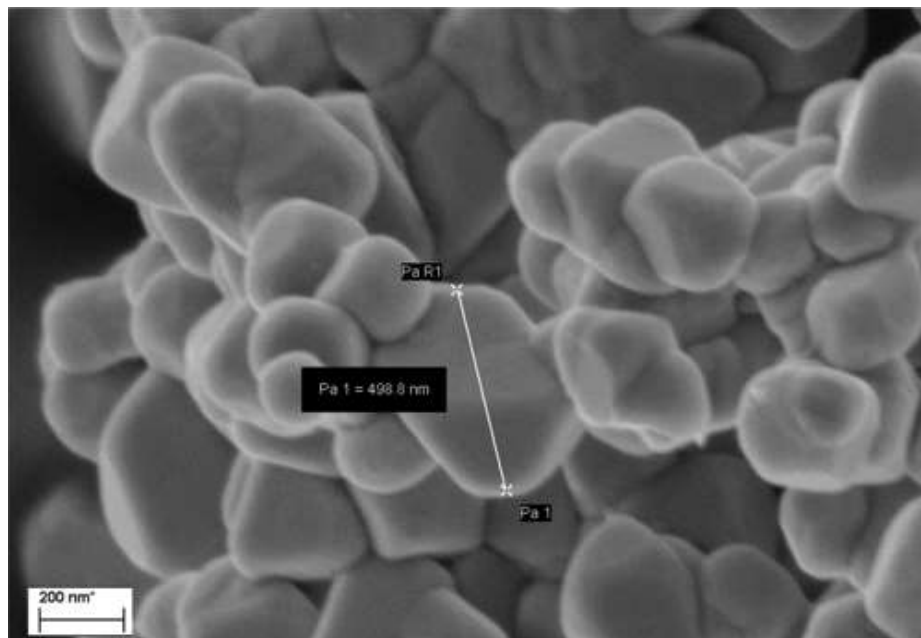


Figure 5-5. SEM image of the synthesized NMC622 particles with a size distribution of 0.2-0.5 μm size.

5-3-2 Test Conditions

The EC/DEC electrolyte decomposition pathways have been widely studied.^{11-13,24}

Both solvents undergo either one or two-electron reactions, generating gaseous species such as CO₂, CO, and C₂H₄. A summary of the gas evolution mechanism is shown

below:

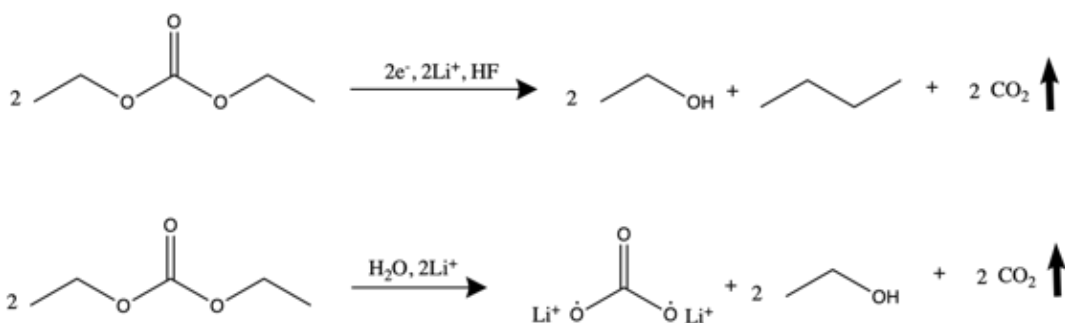


Figure 5-6. Decomposition mechanism of DEC in lithium-ion batteries

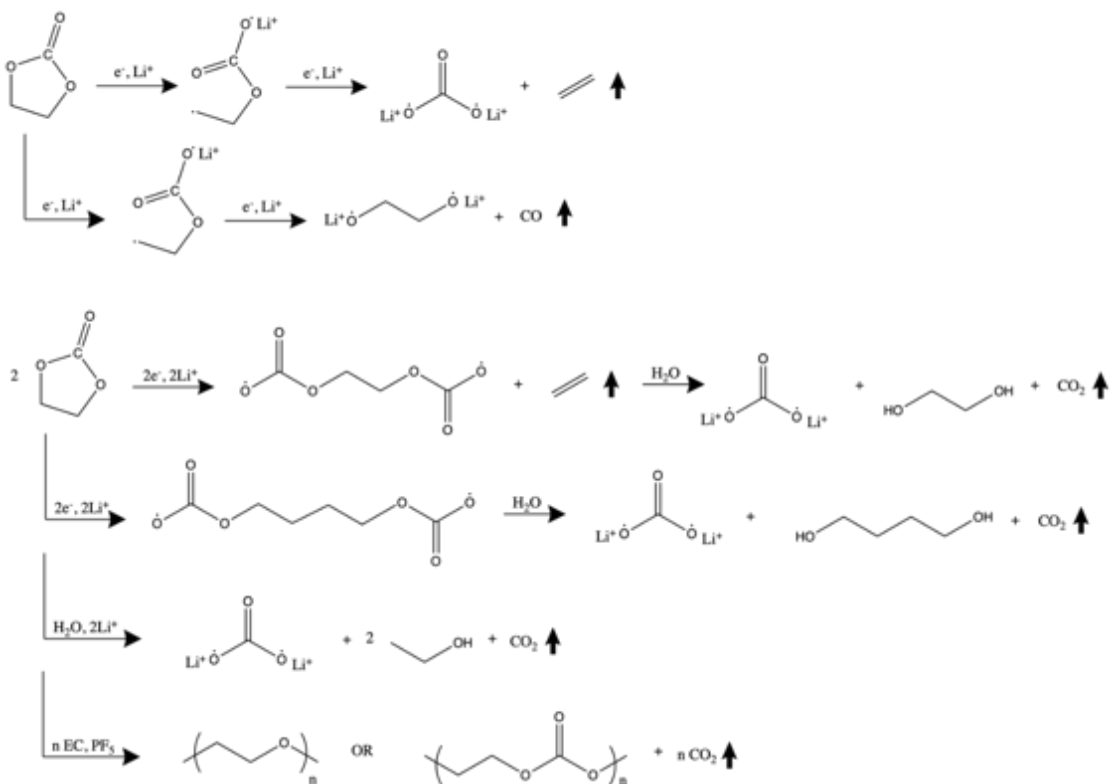


Figure 5-7. Decomposition mechanism of EC in lithium-ion batteries

The reaction mechanisms shown in Figures 5-6 and 5-7 indicate that CO₂ and ethylene are the major gaseous species from EC/DEC electrolyte decomposition. The HF and PF₅ in the above reactions are from the hydrolysis of LiPF₆ lithium salt in the electrolytes.

In addition, O₂ and H₂ evolution have also been previously reported. Oxygen evolution occurs at the cathode, when the LCO or NMC were overcharged, due to the overlap between the O 2p orbital and Co 3d orbitals or to the phase transformation from spinel to rock salt at the cathode surface, respectively.^{15,19,25-30} On the other hand, hydrogen evolution mainly occurs at the Li metal anode and is mainly due to SEI formation and water contamination.^{30,31} Since these four gaseous species are the most crucial products in the decomposition processes of battery materials, we decided to monitor the gas evolution patterns from these four gases to validate our new DEMS cell. The mass fragment signals from m/z=2, 26, 32, and 44 were employed in the following work, which were assumed to represent the gassing behaviors from H₂, C₂H₄, O₂, and CO₂. CO is another gas generated from the electrolyte decomposition reactions. Its mass fragment at m/z=28, overlaps significantly with the mass fragment from ethylene and makes it less ideal for our purposes. However, a previous study has shown that LTO can catalyze the reduction of linear carbonate, generating a decent amount of CO gas as byproduct.³² Thus, we only include m/z=28 results from the anode measurement.

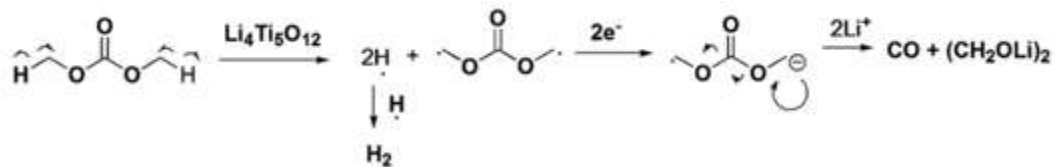


Figure 5-8. Decomposition mechanism of linear carbonate catalyzed by lithium titanate.

In summary, the following measurement conditions were employed in all experiments:

Cyclic voltammetry scan rate: 0.5mV/s

Electrolytes: 1M LiPF₆ in EC/DEC (1:1), 200 μL

Optimized DEMS internal pressure: 2.0-5.0×10⁻⁶ mbar

Separator: Whatman glass fiber filter paper, G/F-F

Five mass spectrometric currents, generated from mass fragments, were monitored for cathode materials. These were:

m/z=2, hydrogen

m/z=26, ethylene

m/z=28, carbon monoxide/ethylene

m/z=32, oxygen

m/z=44, carbon dioxide

5-3-2. Gas evolution at room temperature

The cyclic voltammetric profiles for LCO and NMC 622 are shown in Figures 5-9 and 5-10, respectively. Both cells were cycled from 3V to 5V for three cycles at a scan rate of 0.5mV/s. The regular operation voltage window for a lithium-ion battery is 3V-4.2V. The relatively high upper cut-off voltage in this experiment ensures a full delithiation of the cathode material, which provides more insights over the entire span of the oxidation of the cathode. This extended voltage window also promotes more intense gassing reactions from the electrolyte decomposition and enables us to collect more information on potential-induced gas evolution originating from electrolyte decomposition.

In the LCO CV profile (Fig 5-9), there are two oxidative peaks. The primary oxidation peak at around 4.2V is attributed to the oxidation of Co^{3+} to Co^{4+} . The second peak at 4.7V is the order/disorder transformation from the O3 to the O1 structure, driven by the over delithiation.³³ The reductive peak at 3.8V represents the reduction of Co ions. The peak intensity decreased quickly within three cycles, indicating a fast capacity fade. This is expected for an LCO cell repeatedly charged to 5V.

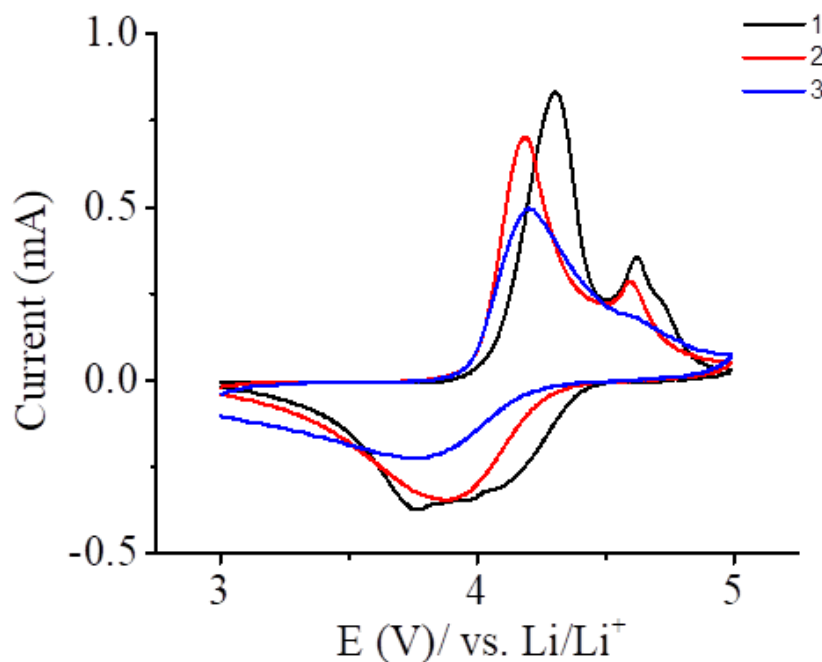


Figure 5-9. CV profile of LiCoO₂ measured using a coin cell-based DEMS cell. The cell voltage was scanned from 3V to 5V at a scan rate of 0.5mV/s.

Unlike the CV for LCO, NMC 622 only had one broad oxidation peak, corresponding to the Co^{3+/4+} and Ni^{2+/4+} oxidation reactions, whose oxidation peaks overlap. In the reverse process, the reductive current at around 4.5V may come from the H3→H2 phase transition or from an oxygen redox feature, as suggested by Tarascon's group using Li₂Ru_{1-y}Sn_yO₃ and Li₂IrO₃ as models.^{34,35} The second reductive peak at 3.5V is ascribed to the reduction of Ni and Co ions.

Compared with figure 5-9, the NMC 622 also had better cyclability and benefited from the Mn ion, which provides stability at high potentials.³⁶ Compared to CVs from a conventional coin cell, the redox reactions in the DEMS cell had slightly higher

overpotentials. This may result, at least in part, from the relatively faster scan rate of 0.5 mV/s and the extremely low pressure within the mass spectrometer system.

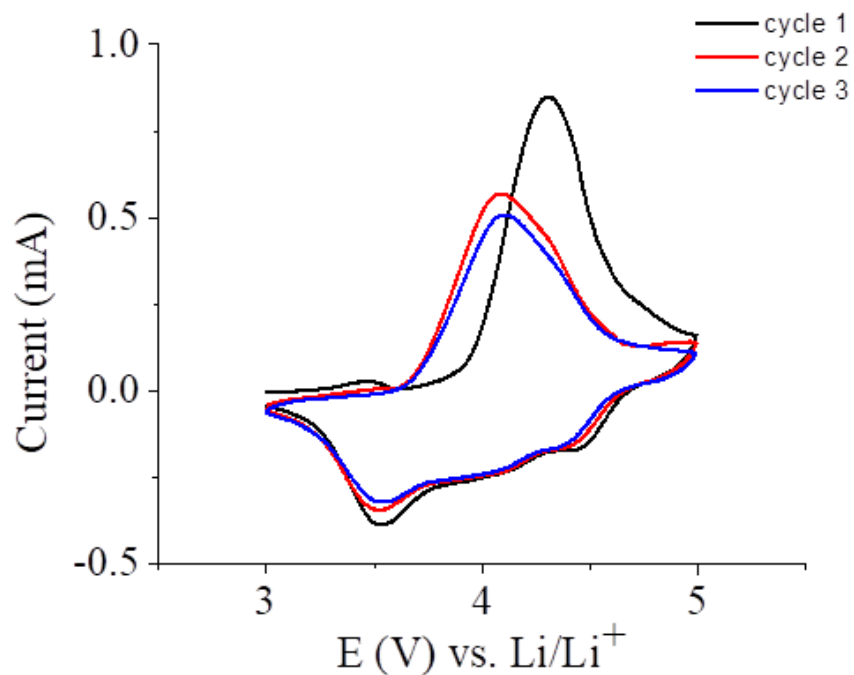


Figure 5-10. CV profile of NMC 622 measured using a coin cell-based DEMS cell.

The cell was scanned from 3V to 5V at a scan rate of 0.5mV/s.

Figures 5-11 and 5-12 present the hydrogen responses of the DEMS cell from LiCoO_2 and NMC622 electrodes, respectively, collected concurrently with the CV.

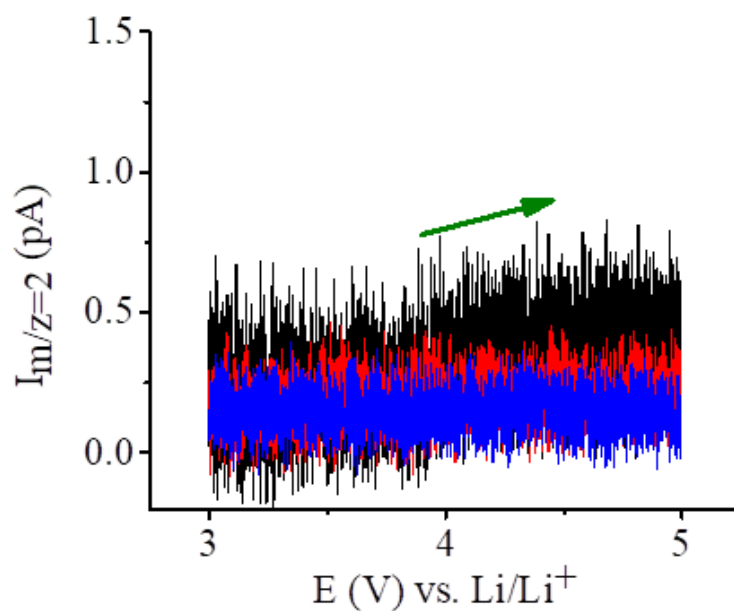


Figure 5-11. Hydrogen evolution data for LiCoO₂ electrode in 1 M LiPF₆ EC/DEC at a scan rate of 0.5 mV/s.

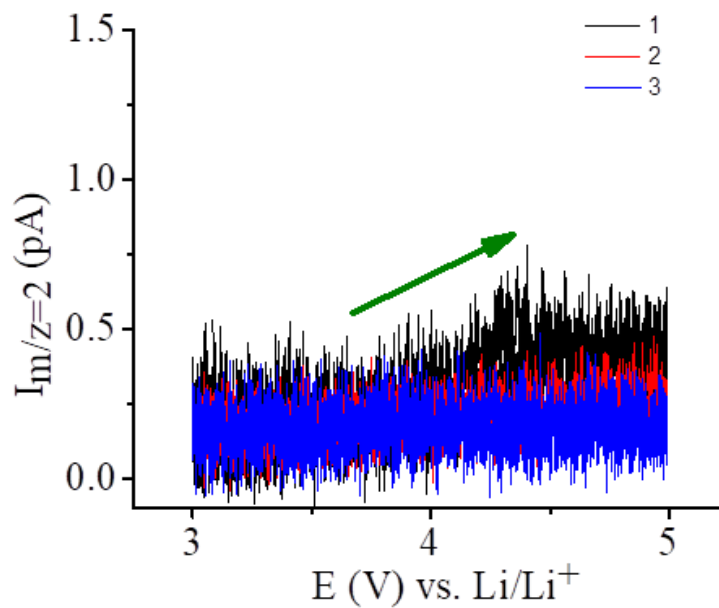


Figure 5-12. Hydrogen evolution data for NMC622 electrode in 1 M LiPF₆ EC/DEC at a scan rate of 0.5 mV/s.

As shown in the figures, hydrogen evolution started at 4V vs. Li/Li⁺ in both cells. The H₂ released from the cathode cells is from the trace amounts of water contamination in the electrolytes. Bernhard et al. have previously shown that about 80% of the hydrogen generated from LIBs was from water reduction.^{37,38} Galushkin et al. proposed that the EC decomposition at the graphite anode may also generate hydrogen, as shown in figure 5-13.¹² This reaction was further promoted by the presence of the metallic lithium anode.

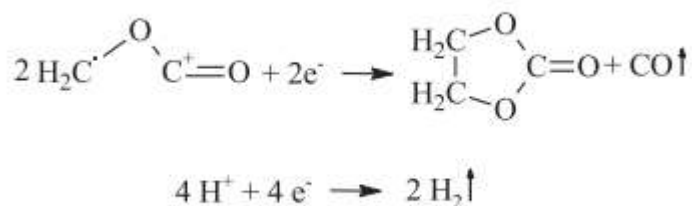


Figure 5-13. Reaction mechanisms of EC decomposition occurring at the anode.

The hydrogen current in both cells was about 0.7pA, suggesting that the hydrogen gas released was approximately the same, which was expected as the amount of electrolyte added to each coin cell was fixed.

The evolution of CO₂ from the LCO and NMC622 cells is shown in Figures 5-14 and 5-15. In contrast with H₂ evolution, the CO₂ mass fragment current from the NMC 622 cell was much greater than in the LCO cell. This is consistent with previous studies.⁵⁻⁷ High nickel content NMC cathode materials are known for their vigorous gas evolution, and our results are consistent with this. The evolution of carbon dioxide

started at around 4.5V, reached a maximum shortly after the cell hit the cut-off voltage of 5V, and then decreased throughout the reduction reaction.

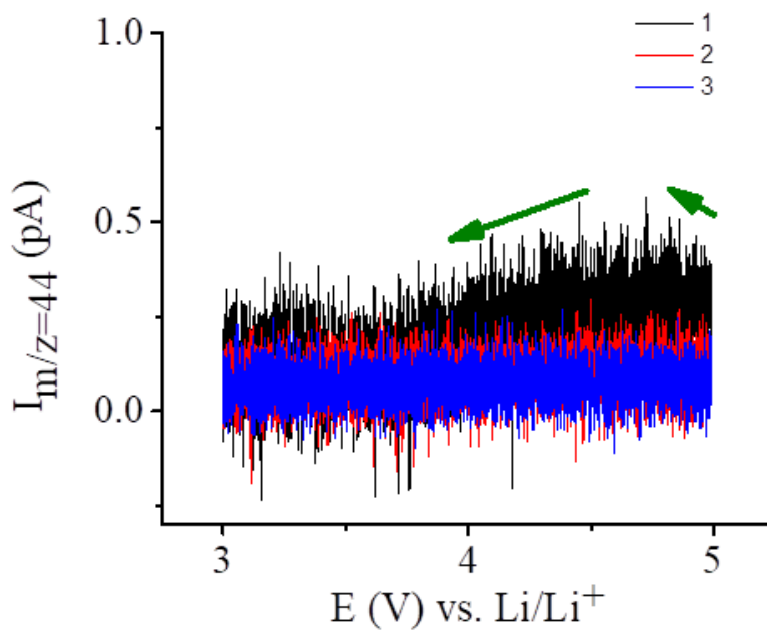


Figure 5-14. CO₂ evolution data for a LiCoO₂ electrode in 1 M LiPF₆ EC/DEC at a scan rate of 0.5 mV/s.

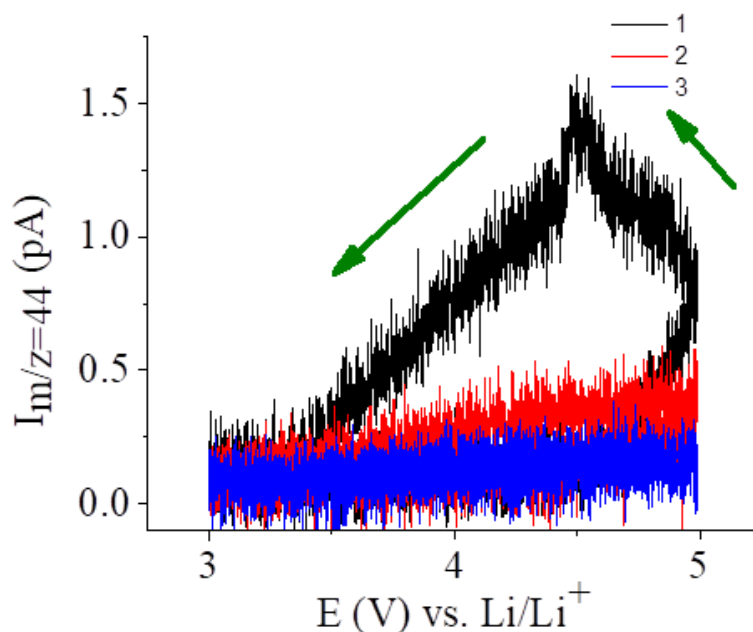


Figure 5-15. CO_2 evolution data for NMC622 electrode in 1 M LiPF_6 EC/DEC at a scan rate of 0.5 mV/s.

Figures 5-16 to 5-19 present the evolution of ethylene and oxygen from LCO and NMC622 cells. In Fig 5-16 and 18, LCO showed no oxygen nor ethylene evolution in the first cycle, while NMC 622 (Fig. 5-17) generated a small amount of oxygen in the first cycle at the first oxidative potential.

Numerous previous studies have reported on the release of oxygen from LCO batteries at high potential, resulting from electron migration from cobalt 3d to the oxygen 2sp orbital. There are also reports that minimal O_2 was observed during the LCO delithiation process, even at 5V, especially when the CV was measured. Papp et al. used constant current constant voltage (CCCV) and carbonate titration measurements, in combination with DEMS, to show that no oxygen participates in the charge

compensation during over-delithiation of LCO. They also showed that oxygen release was not a byproduct of electrolyte degradation at the cathode surfaces.⁶ Oxygen release may also not also have been observed because it was below the detection limit of our DEMS system.

Unlike LCO, a small amount of O₂ was detected from the NMC622 cell with our system. As shown in Figure 5-17, the O₂ evolution was directly related to the oxidation peak. This small amount of oxygen may be attributed to the Ni redox reaction and phase changes from layered structure to the disordered spinel structure. O₂ evolution began at around 4V, which corresponds to the onset potential of Ni oxidation.³⁹ Ethylene was not detected in neither LCO nor NMC, likely due to the amount of ethylene released being below the detection limit of our instrument.

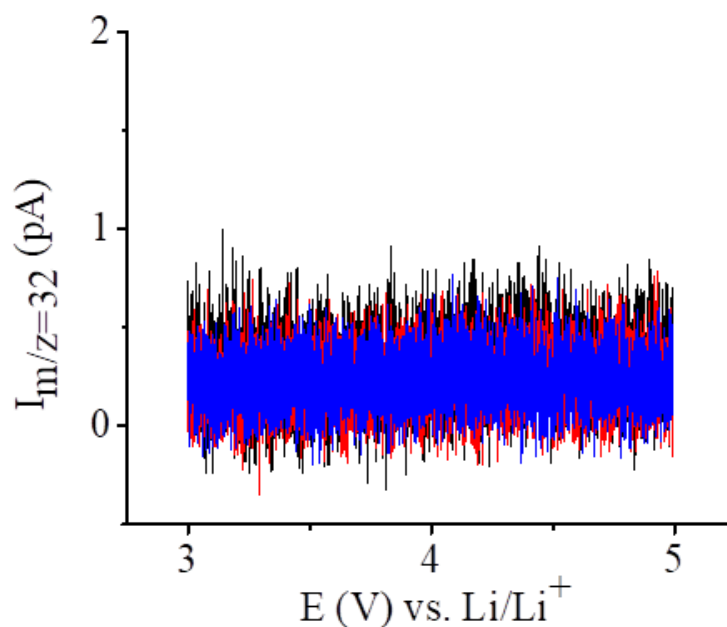


Figure 5-16. O₂ evolution data for LiCoO₂ electrode in 1 M LiPF₆ EC/DEC at a scan rate of 0.5 mV/s.

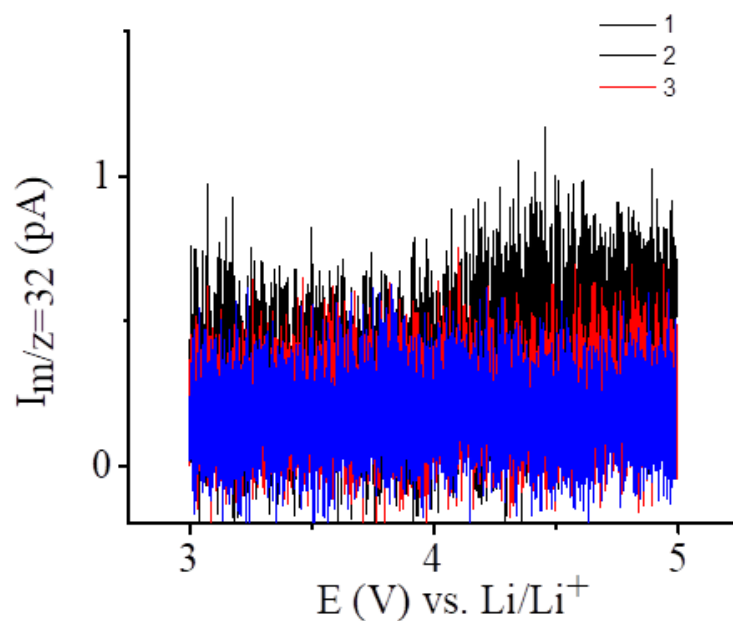


Figure 5-17. O₂ evolution data for NMC622 electrode in 1 M LiPF₆ EC/DEC at a scan rate of 0.5 mV/s.

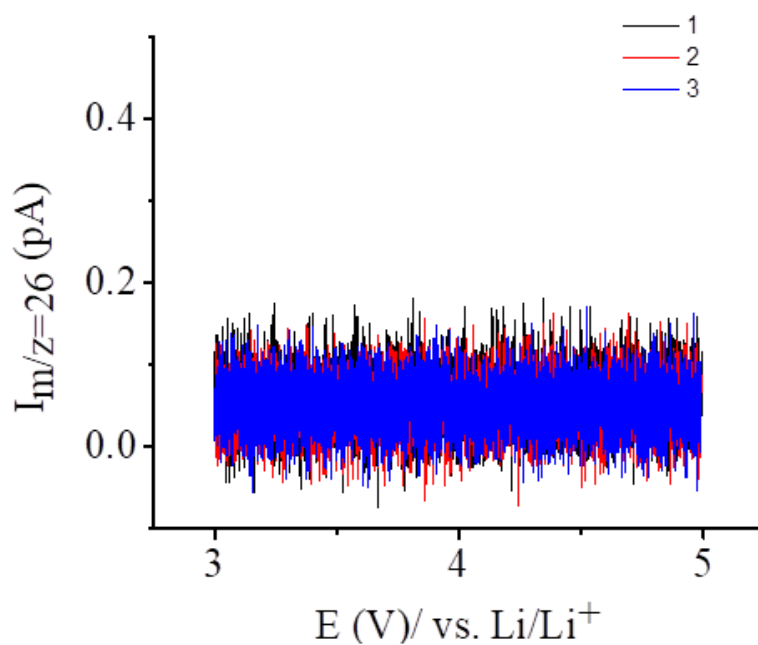


Figure 5-18. Ethylene evolution data for LiCoO₂ electrode in 1 M LiPF₆ EC/DEC at a scan rate of 0.5 mV/s.

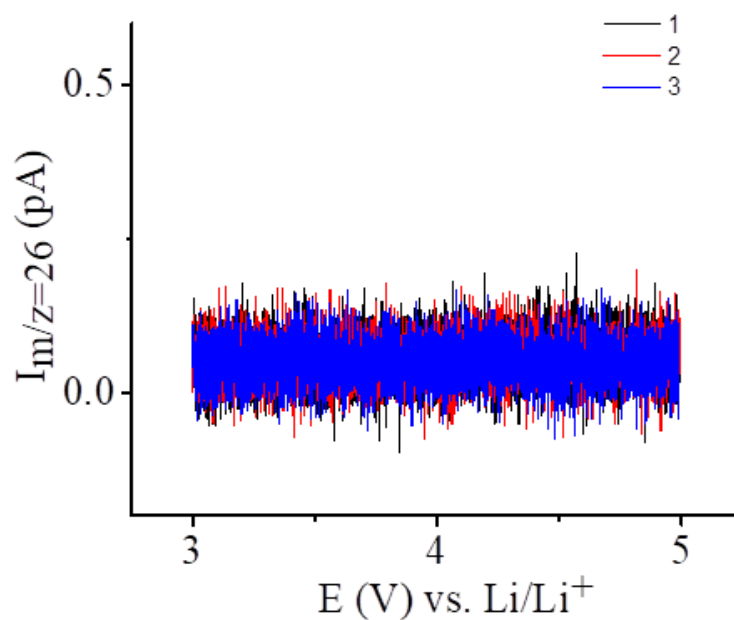


Figure 5-19. Ethylene evolution data for NMC622 electrode in 1 M LiPF_6 EC/DEC at a scan rate of 0.5 mV/s.

Gas evolution from the lithium titanate (LTO) anodes are shown in the following section. Lithium titanate anodes outperform graphite anodes for its zero-strain property, leading to minimal volume changes and excellent rate performance at low temperatures.^{32,40,41} However, LTO suffers from severe gassing issues, which while a drawback for battery operation, it makes it a good candidate for our purposes.

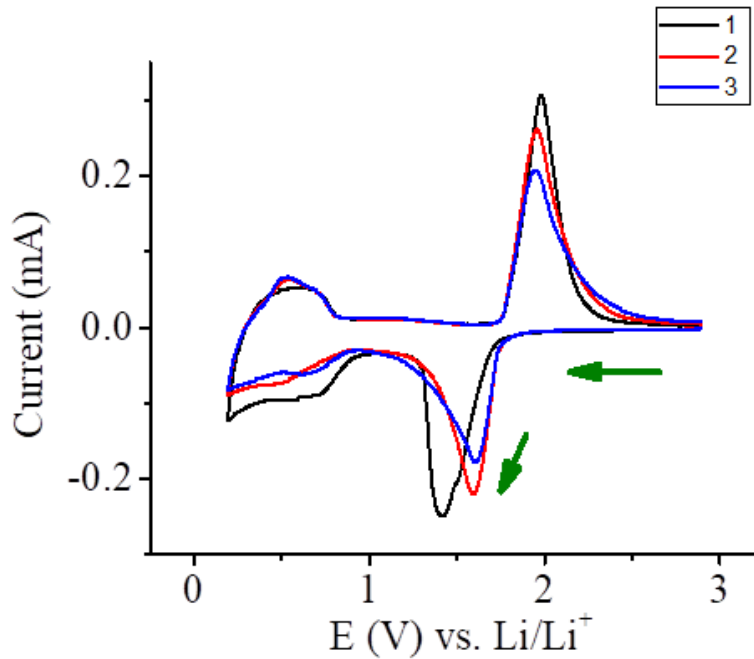


Figure 5-20. CV profile from $\text{Li}_4\text{Ti}_5\text{O}_{12}$ measured using a coin cell-based DEMS cell.

The cell was scanned from 3V to 0.2V with a scan rate of 0.5mV/s.

CV profile of LTO measured in our new DEMS cell. As it is an anode material, the CV was scanned negatively from 3V to 0.2V. The primary redox couple represents the redox of $\text{Ti}^{3+/5+}$, while the signals below 0.8V were ascribed to electrolyte decomposition.

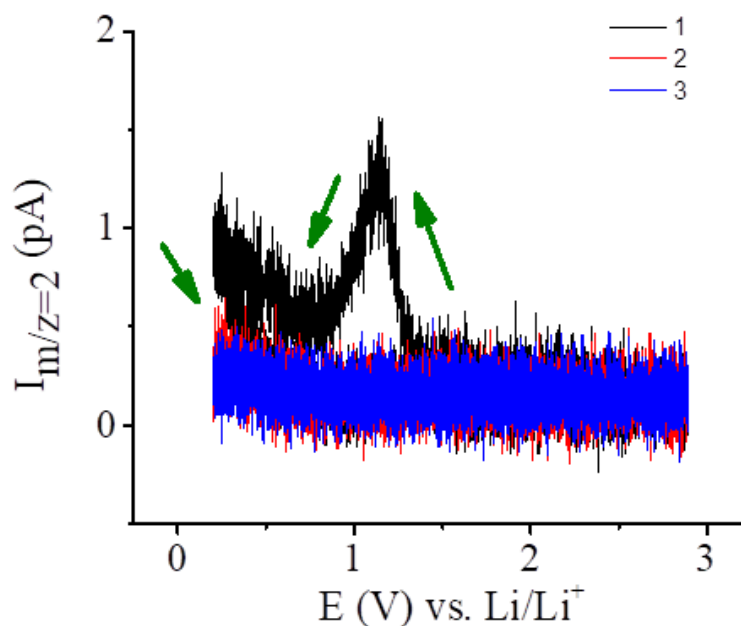


Figure 5-21. Hydrogen evolution data for $\text{Li}_4\text{Ti}_5\text{O}_{12}$ electrode in 1 M LiPF_6 EC/DEC at a scan rate of 0.5 mV/s.

The hydrogen evolution pattern for the LTO cell is shown in figure 5-21. The hydrogen signal from the first cycle peaked at around 1.2V, coinciding with the first $\text{Ti}^{5+} \rightarrow \text{Ti}^{3+}$ reduction peak in the CV. It was well-known that LTO and TiO_2 , the most common impurity in LTO, can catalyze hydrogen evolution via the dehydrogenation reaction of the alkoxy group.⁴² The distinct peak from the $m/z=2$ response is consistent with this reaction and illustrates the effectiveness of our cell design. The second hydrogen peak below 1V arises from the potential induced hydrogen evolution reaction from the trace amount of water present in the electrolyte, as the voltage range of LTO based batteries is low enough to generate H_2 gas.

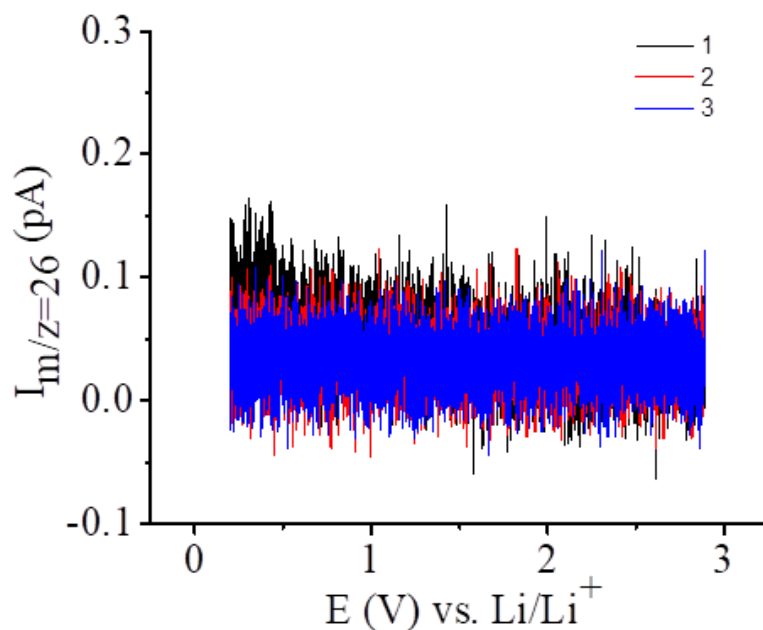
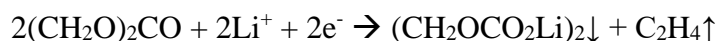


Figure 5-22. Ethylene evolution data for $\text{Li}_4\text{Ti}_5\text{O}_{12}$ electrode in 1 M LiPF_6 EC/DEC at a scan rate of 0.5 mV/s.

C_2H_4 evolution was also observed in the LTO cell, which was caused by the reductive decomposition of the EC solvent at low potentials.



In addition to hydrogen and ethylene, carbon monoxide is also a key gas component in the gaseous evolution from LTO. Unfortunately, the major mass fragment of CO is $m/z=28$, which severely overlapped with the mass fragment of ethylene. To illustrate the carbon monoxide evolution patterns and remove/mitigate the interference from ethylene, we multiplied the ethylene gas signal at $m/z=26$ by a factor of 1.7, calculated from the standard mass spectrum of ethylene, and subtracted it from the $m/z=28$ current to estimate the CO contribution at $m/z=28$. ($\text{ICO} = I_{m/z=28} - (I_{m/z=26} \times 1.7)$) The resulting plot is shown in Figure 5-23

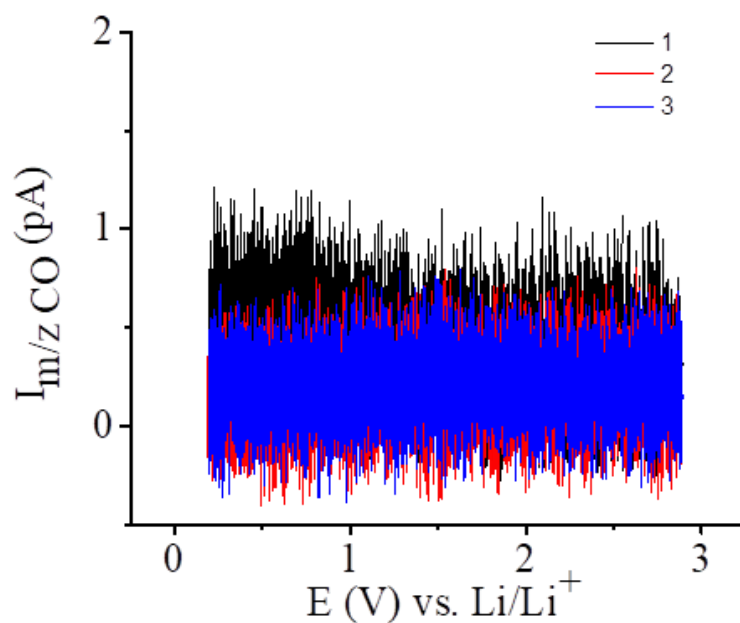
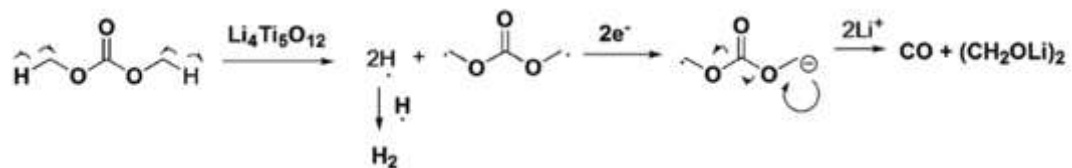


Figure 5-23. CO evolution data for $\text{Li}_4\text{Ti}_5\text{O}_{12}$ electrode in 1 M LiPF_6 EC/DEC at a scan rate of 0.5 mV/s.

The CO started releasing at around 1.2V, again coinciding with the onset potential of the $\text{Ti}^{3+/4+}$ redox reaction. 1.2 V was also the potential where H_2 evolution occurred. This agreed with the gas generation reactions proposed by He et al., that CO evolution is a subsequent reaction of H_2 evolution promoted by LTO, as shown in the following reaction.³²



5-3-4. Gas evolution at elevated temperature

All of the above-mentioned gas evolution patterns have shown the effectiveness of our newly designed coin cell-based DEMS cell set-up at room temperature. However, due to the extensive battery use in electric vehicles, it is essential to gain insights into the gassing behavior of lithium-ion batteries at elevated temperatures under operating conditions. Thus, we decided to evaluate this new cell at 45 °C. As LTO is not widely used in EVs, only two cathode materials, LCO and NMC622, were tested.

The CV profiles of LCO and NMC 622 are shown in figure 5-24 and 5-25

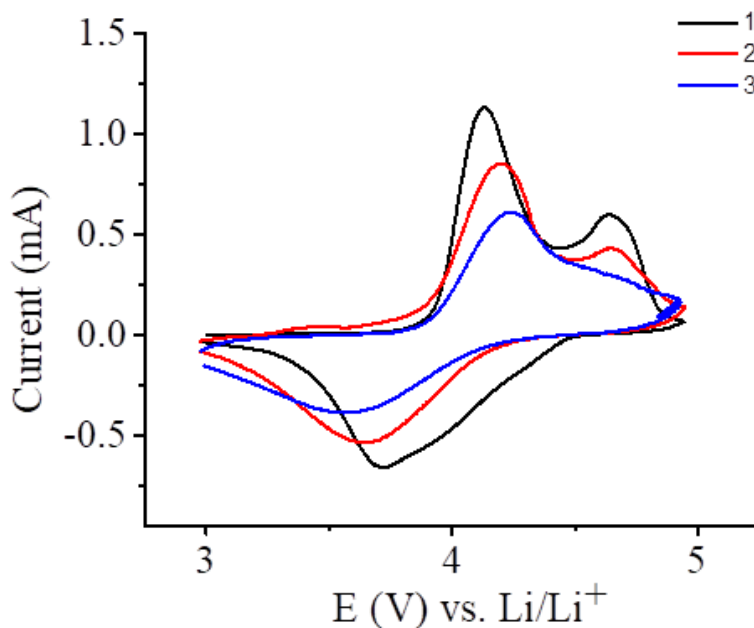


Figure 5-24. CV profile of LiCoO₂ measured using a coin cell-based DEMS cell. The cell was scanned from 3V to 5V with a scan rate of 0.5mV/s at a temperature of 45°C.

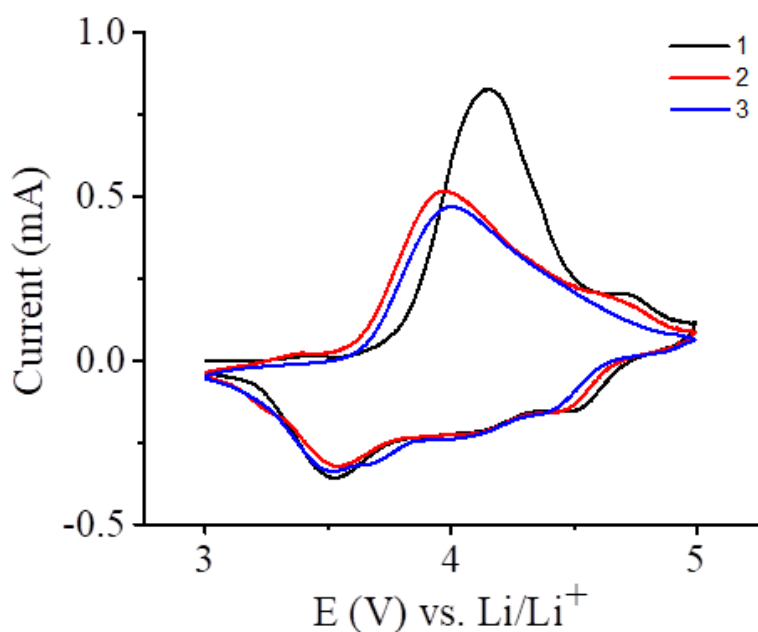


Figure 5-25. CV profile from NMC measured using a coin cell-based DEMS cell. The cell was scanned from 3V to 5V with a scan rate of 0.5mV/s, at a temperature of 45°C

Like the CVs at room temperature, LCO exhibited two distinct oxidation peaks, from the $\text{Co}^{3+/4+}$ redox couple and the O3-O1 phase transition. The reduction peak was again from the reduction of cobalt ions. Comparing the LCO CV profiles at both room temperature and 45°C (Fig 5-9 and 5-24, respectively), the capacity degradation at 45°C was more severe, which was expected given the high temperature and extended potential range. The CV of the NMC 622 cell also matched well with the one at room temperature. It again showed better capacity retention because of the addition of Mn ions providing thermal and structural stability.

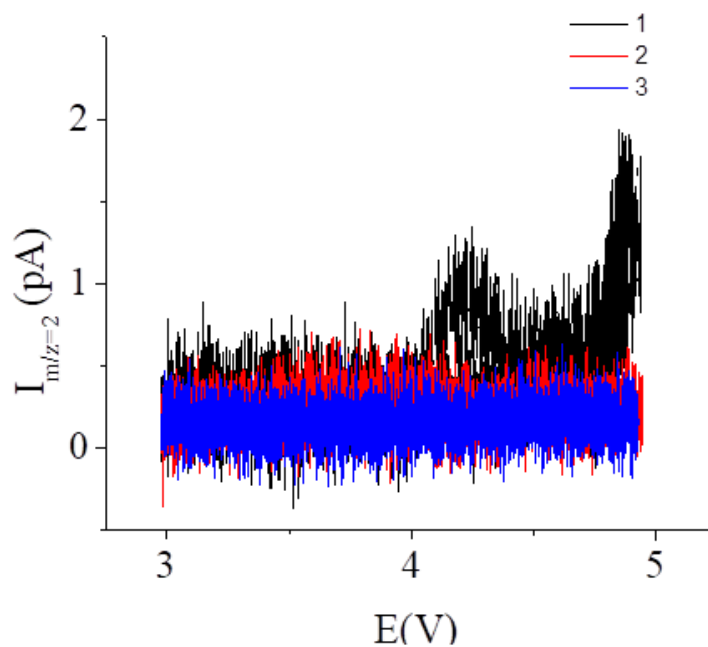


Figure 5-26. Hydrogen evolution data for LiCoO₂ electrode in 1 M LiPF₆ EC/DEC at a scan rate of 0.5 mV/s, at a temperature of 45°C

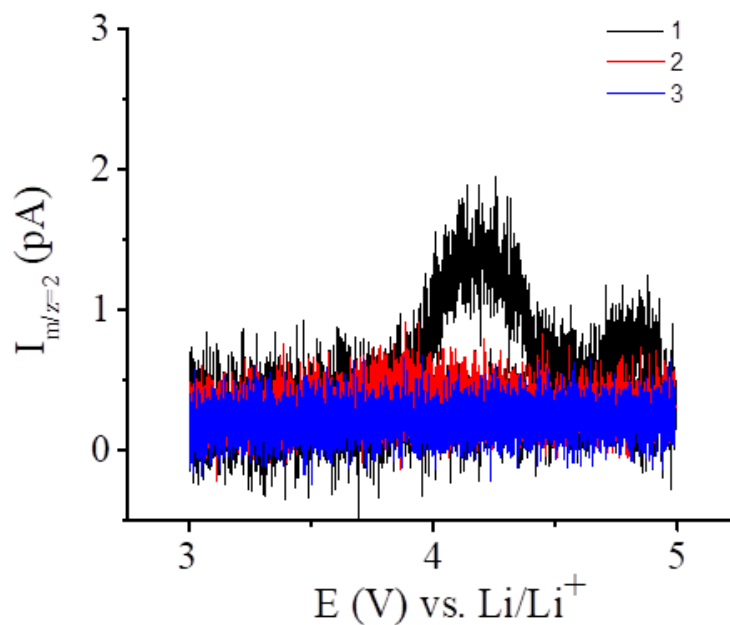
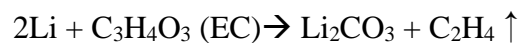


Figure 5-27. Hydrogen evolution data for NMC622 electrode in 1 M LiPF₆ EC/DEC at a scan rate of 0.5 mV/s, at a temperature of 45°C

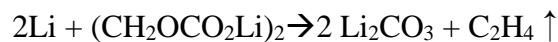
The H₂ evolution patterns were significantly different from the ones at room temperature. The amount of H₂ produced in each cell was significantly increased as the elevated temperature accelerated the redox reaction kinetics and electrolyte decomposition. In addition to the increased amount of H₂ generated at 45°C, the gas evolution pattern was also different. Both cells showed a gassing peak that started at the onset potential of the first oxidation peak (4V and 3.8V for LCO and NMC 622, respectively). This directly links the H₂ evolution to the redox reaction of the cathode material, possibly resulting from the accelerated SEI formation process, which was also supported by the increased amount of the C₂H₄ signal as shown in Figures 5-28,29, whose gas release started at the onset potential of oxidation peak as well.

Ethylene is a byproduct of EC reduction during SEI layer formation and the decomposition on the anode as described in the equations presented below¹²

SEI formation:



SEI decomposition:



Recalling the results obtained at room temperature, while observation of the ethylene signal limited due to the mass spectrometer detection limit; the evolution of ethylene at 45°C was much more significant. This increase in the amount of gas evolved showed that not only was the speed of SEI formation enhanced, but also the amount of SEI formed during the first charge was also increased, assisted by the oxidation

reaction. The increased signal at 45°C agreed with previous studies and again demonstrated the effectiveness of this new cell design.

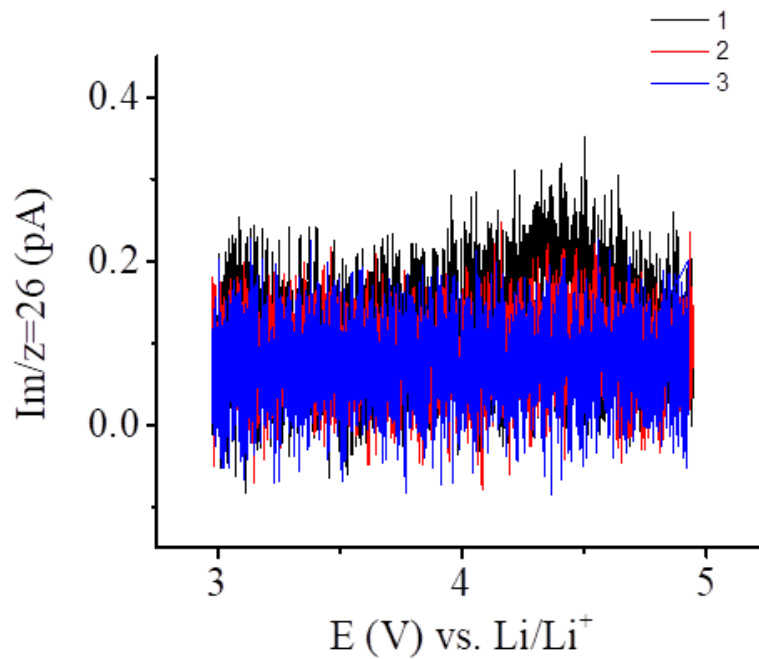


Figure 5-28. Ethylene evolution data for LiCoO_2 electrode in 1 M LiPF_6 EC/DEC at a scan rate of 0.5 mV/s, at a temperature of 45°C

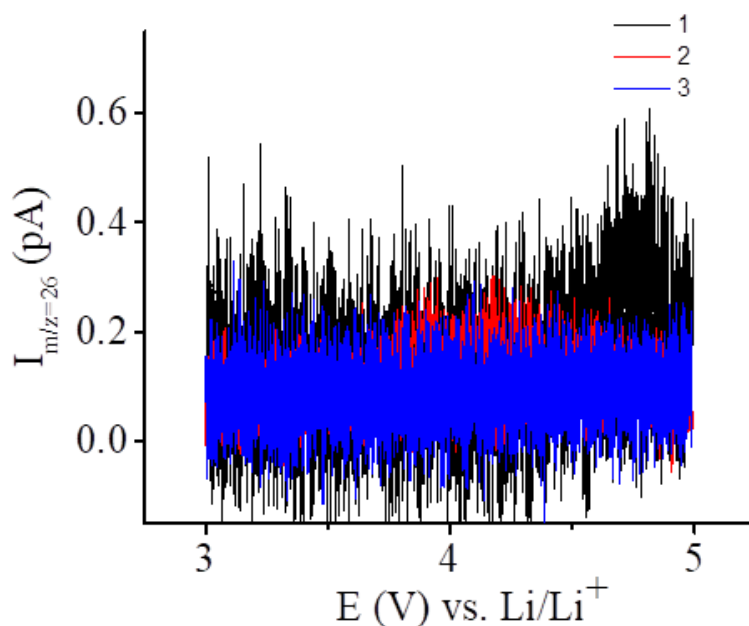


Figure 5-29. Ethylene evolution data for NMC622 electrode in 1 M LiPF₆ EC/DEC at a scan rate of 0.5 mV/s, at a temperature of 45°C

In addition to hydrogen and ethylene, we also monitored the oxygen and carbon dioxide gassing patterns, and the results are presented in Figures 5-30 to 5-33. Both cells released more gas at elevated temperatures. It has been reported that at 40°C, as the electrolyte decomposition accelerated, more compact lithium precipitates were formed rather than soft organics. This increased the amount of inorganic byproducts formed at high temperatures leading to an enhanced CO₂ and O₂ formation, following the equations below.⁴³



Gasteiger et al. have examined the temperature dependence gas evolution of NMC 622. In their studies, O₂ evolution in NMC 622 occurs after 4.41V.⁴⁴, in excellent agreement with our observations from the coin cell-based DEMS cell. (Fig. 5-31)

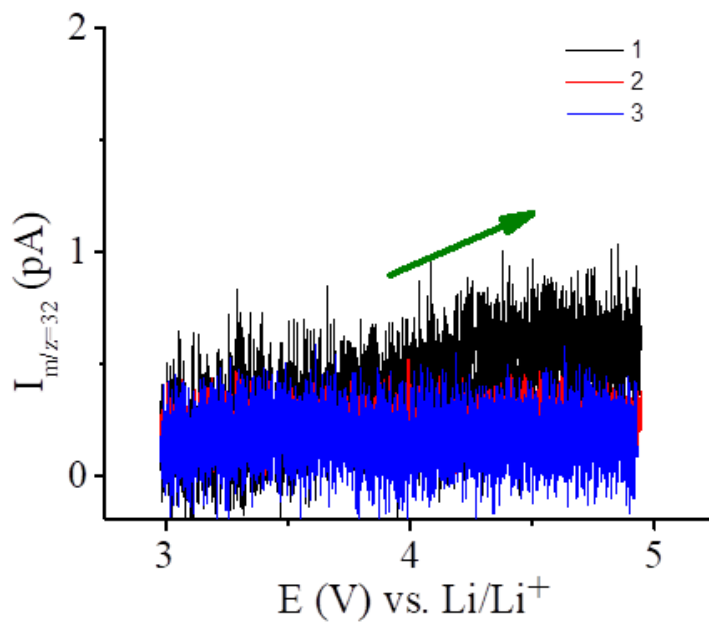


Figure 5-30. Oxygen evolution data for LiCoO₂ electrode in 1 M LiPF₆ EC/DEC at a scan rate of 0.5 mV/s, at a temperature of 45°C

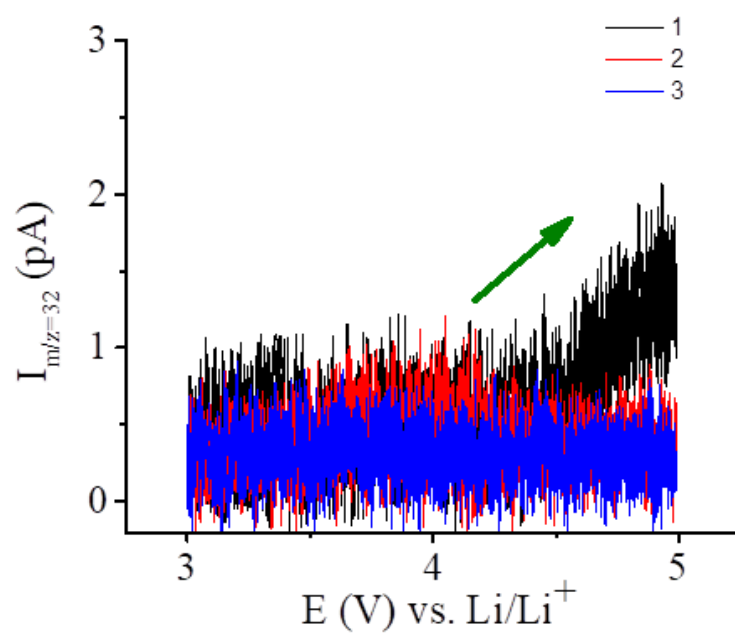


Figure 5-31. oxygen evolution data for NMC622 electrode in 1 M LiPF₆ EC/DEC at a scan rate of 0.5 mV/s, at a temperature of 45°C

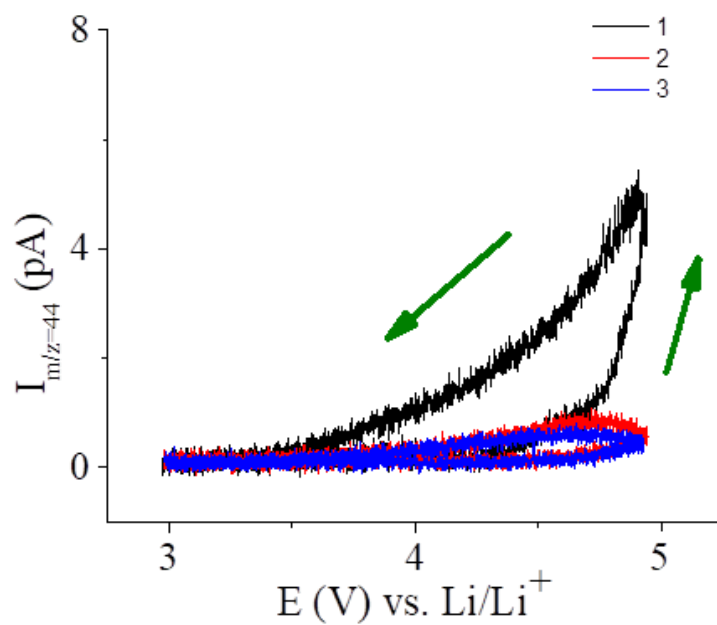


Figure 5-32. CO₂ evolution data for LiCoO₂ electrode in 1 M LiPF₆ EC/DEC at a scan rate of 0.5 mV/s, at a temperature of 45°C

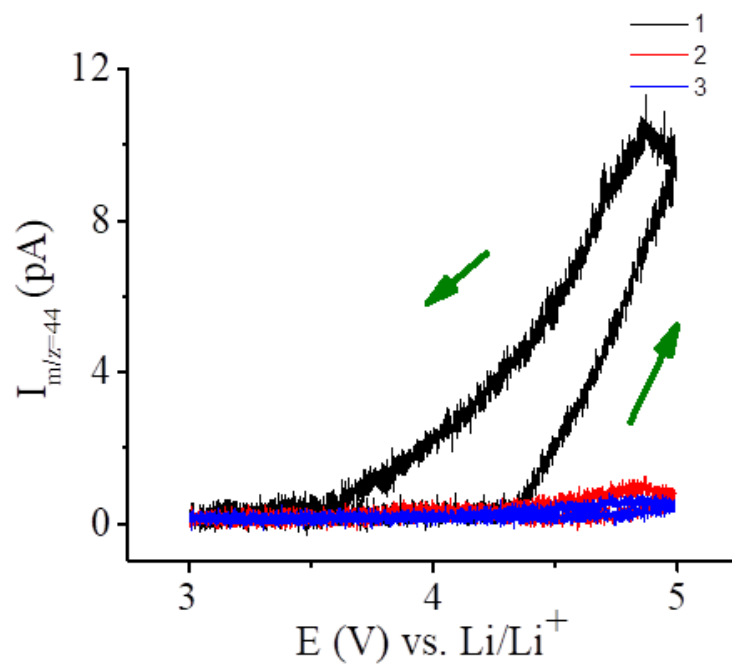


Figure 5-33. CO_2 evolution data for NMC622 electrode in 1 M LiPF_6 EC/DEC at a scan rate of 0.5 mV/s, at a temperature of 45°C

5-4. Conclusions

In this work, a new coin cell-based DEMS cell was designed to study, *in operando*, the gas evolution from lithium-ion batteries. Three electrode materials, lithium cobalt oxide, $\text{LiNi}_{0.6}\text{Mn}_{0.2}\text{Co}_{0.2}\text{O}_2$ (NMC622), and lithium titanate, were used to validate the effectiveness of this new coin cell-based DEMS cell. We observed the evolution of hydrogen and CO_2 associated with electrolyte decomposition and SEI formation in both LCO and NMC 622 and the oxygen evolution from Ni-rich NMC622 when pairing with the metallic lithium anode and EC/DEC electrolyte. We also detected the evolution of hydrogen and carbon monoxide from the lithium titanate.

This newly designed cell was further tested at 45 °C. Gas evolution at high temperatures is essential for evaluating battery materials, and the ability of our system to operate at high temperatures adds more value to our design. Using our new cell, we observed significantly enhanced hydrogen and carbon dioxide gassing as 45 °C, resulting from the increased temperature. Moreover, we also observed the evolution ethylene and oxygen from both LCO and NMC cathodes, which we could not observe at room temperature.

We believe that this new cell design will provide valuable insights into degradation pathways of battery materials at both room and elevated temperatures, which in turn, will help in the rational design of next-generation high performance battery materials.

Acknowledgements:

This work was supported by Arkema Inc. and by the Air Force Office of Scientific Research under the MURI Program through award number FA9550-18-1-0420.

References

- (1) Scrosati, B.; Hassoun, J.; Sun, Y.-K. Lithium-Ion Batteries. A Look into the Future. *Energy & Environmental Science* **2011**, *4* (9), 3287.
- (2) van Noorden, R. The Rechargeable Revolution: A Better Battery. *Nature* **2014**, *507* (7490), 26–28.
- (3) Bukhari, S. M. A. S.; Maqsood, J.; Baig, M. Q.; Ashraf, S.; Khan, T. A. Comparison of Characteristics-Lead Acid, Nickel Based, Lead Crystal and Lithium Based Batteries. *Proceedings - UKSim-AMSS 17th International Conference on Computer Modelling and Simulation, UKSim 2015* **2016**, 444–450.
- (4) Kim, T.; Song, W.; Son, D. Y.; Ono, L. K.; Qi, Y. Lithium-Ion Batteries: Outlook on Present, Future, and Hybridized Technologies. *Journal of Materials Chemistry A*. 2019, pp 2942–2964.
- (5) Myung, S.-T.; Maglia, F.; Park, K.-J.; Yoon, C. S.; Lamp, P.; Kim, S.-J.; Sun, Y.-K. Nickel-Rich Layered Cathode Materials for Automotive Lithium-Ion Batteries: Achievements and Perspectives. *ACS Energy Letters* **2016**, *2* (1), 196–223.
- (6) Papp, J. K.; Li, N.; Kaufman, L. A.; Naylor, A. J.; Younesi, R.; Tong, W.; McCloskey, B. D. A Comparison of High Voltage Outgassing of LiCoO₂, LiNiO₂, and Li₂MnO₃ Layered Li-Ion Cathode Materials. *Electrochimica Acta* **2021**, *368*, 8–10.
- (7) Liu, W.; Oh, P.; Liu, X.; Lee, M.-J.; Cho, W.; Chae, S.; Kim, Y.; Cho, J. Nickel-Rich Layered Lithium Transition-Metal Oxide for High-Energy Lithium-Ion Batteries. *Angewandte Chemie* **2015**, *127* (15), 4518–4536.

- (8) Deng, J.; Bae, C.; Denlinger, A.; Miller, T. Electric Vehicles Batteries : Requirements and Challenges. *Joule* **2020**, *4*, 1–5.
- (9) Guilmard, M.; Croguennec, L.; Denux, D.; Delmas, C. Thermal Stability of Lithium Nickel Oxide Derivatives. Part I: $\text{Li XNi}_{1.02}\text{O}_2$ and $\text{Li}_x\text{Ni}_{0.89}\text{Al}_{0.16}\text{O}_2$ ($x = 0.50$ and 0.30). *Chemistry of Materials* **2003**, *15* (23), 4476–4483.
- (10) Larsson, F.; Bertilsson, S.; Furlani, M.; Albinsson, I.; Mellander, B. E. Gas Explosions and Thermal Runaways during External Heating Abuse of Commercial Lithium-Ion Graphite-LiCoO₂ Cells at Different Levels of Ageing. *Journal of Power Sources* **2018**, *373* (September 2017), 220–231.
- (11) Zhang, S. S. Insight into the Gassing Problem of Li-Ion Battery. *Frontiers in Energy Research* **2014**, *2* (DEC), 2–5.
- (12) Galushkin, N. E.; Yazvinskaya, N. N.; Galushkin, D. N. Mechanism of Gases Generation during Lithium-Ion Batteries Cycling. *Journal of The Electrochemical Society* **2019**, *166* (6), A897–A908.
- (13) Rowden, B.; Garcia-Araez, N. A Review of Gas Evolution in Lithium Ion Batteries. In *Energy Reports*; Elsevier Ltd, 2020; Vol. 6, pp 10–18.
- (14) Bawol, P. P.; Reinsberg, P.; Bondue, C. J.; Abd-El-Latif, A. A.; Königshoven, P.; Baltruschat, H. A New Thin Layer Cell for Battery Related DEMS-Experiments: The Activity of Redox Mediators in the Li-O₂ Cell. *Physical Chemistry Chemical Physics* **2018**, *20* (33), 21447–21456.
- (15) Bondue, C. J.; Abd-El-Latif, A. A.; Hegemann, P.; Baltruschat, H. Quantitative Study for Oxygen Reduction and Evolution in Aprotic Organic Electrolytes at Gas

Diffusion Electrodes by DEMS. *Journal of the Electrochemical Society* **2015**, *162* (3), A479–A487.

(16) Jusys, Z.; Binder, M.; Schnaidt, J.; Behm, R. J. A Novel DEMS Approach for Studying Gas Evolution at Battery-Type Electrode|electrolyte Interfaces: High-Voltage LiNi_{0.5}Mn_{1.5}O₄ Cathode in Ethylene and Dimethyl Carbonate Electrolytes. *Electrochimica Acta* **2019**, *314*, 188–201.

(17) Klein, F.; Pinedo, R.; Berkes, B. B.; Janek, J.; Adelhelm, P. Kinetics and Degradation Processes of CuO as Conversion Electrode for Sodium-Ion Batteries: An Electrochemical Study Combined with Pressure Monitoring and DEMS. *Journal of Physical Chemistry C* **2017**, *121* (16), 8679–8691.

(18) Wang, H.; Rus, E.; Sakuraba, T.; Kikuchi, J.; Kiya, Y.; Abruña, H. D. CO₂ and O₂ Evolution at High Voltage Cathode Materials of Li-Ion Batteries: A Differential Electrochemical Mass Spectrometry Study. *Analytical Chemistry* **2014**, *86* (13), 6197–6201.

(19) Holzappel, M.; Würsig, A.; Scheifele, W.; Vetter, J.; Novák, P. Oxygen, Hydrogen, Ethylene and CO₂ Development in Lithium-Ion Batteries. *Journal of Power Sources* **2007**, *174* (2), 1156–1160.

(20) Jozwiuk, A.; Berkes, B. B.; Weiß, T.; Sommer, H.; Janek, J.; Brezesinski, T. The Critical Role of Lithium Nitrate in the Gas Evolution of Lithium-Sulfur Batteries. *Energy and Environmental Science* **2016**, *9* (8), 2603–2608.

(21) Huang, Z.-D. D.; Liu, X.-M. M.; Oh, S.-W. W.; Zhang, B.; Ma, P.-C. C.; Kim, J.-K. K. Microscopically Porous, Interconnected Single Crystal

LiNi_{1/3}Co_{1/3}Mn_{1/3}O₂ Cathode Material for Lithium Ion Batteries. *Journal of Materials Chemistry* **2011**, 21 (29), 10777.

(22) Li, T.; Yuan, X.-Z.; Zhang, L.; Song, D.; Shi, K.; Bock, C. Degradation Mechanisms and Mitigation Strategies of Nickel-Rich NMC-Based Lithium-Ion Batteries. *Electrochemical Energy Reviews* **2020**, 3 (1), 43–80.

(23) Zhang, X.; Jiang, W. J.; Mauger, A.; Qilu; Gendron, F.; Julien, C. M. Minimization of the Cation Mixing in Li_{1+x}(NMC)_{1-x}O₂ as Cathode Material. *Journal of Power Sources* **2010**, 195 (5), 1292–1301.

(24) Henschel, J.; Peschel, C.; Klein, S.; Horsthemke, F.; Winter, M.; Nowak, S. Clarification of Decomposition Pathways in a State-of-the-Art Lithium Ion Battery Electrolyte through ¹³C-Labeling of Electrolyte Components. *Angewandte Chemie - International Edition* **2020**, 59 (15), 6128–6137.

(25) Myeong, S.; Cho, W.; Jin, W.; Hwang, J.; Yoon, M.; Yoo, Y.; Nam, G.; Jang, H.; Han, J. G.; Choi, N. S.; Kim, M. G.; Cho, J. Understanding Voltage Decay in Lithium-Excess Layered Cathode Materials through Oxygen-Centred Structural Arrangement. *Nature Communications* **2018**, 9 (1).

(26) Petersburg, C. F.; Li, Z.; Chernova, N. a.; Whittingham, M. S.; Alamgir, F. M. Oxygen and Transition Metal Involvement in the Charge Compensation Mechanism of LiNi_{1/3}Mn_{1/3}Co_{1/3}O₂ Cathodes. *Journal of Materials Chemistry* **2012**, 22 (37), 19993.

(27) Jung, R.; Strobl, P.; Maglia, F.; Stinner, C.; Gasteiger, H. A. Temperature Dependence of Oxygen Release from LiNi_{0.6}Mn_{0.2}Co_{0.2}O₂ (NMC622) Cathode

- Materials for Li-Ion Batteries. *Journal of the Electrochemical Society* **2018**, *165* (11), A2869–A2879
- (28) Petersburg, C. F.; Li, Z.; Chernova, N. A.; Whittingham, M. S.; Alamgir, F. M. Oxygen and Transition Metal Involvement in the Charge Compensation Mechanism of $\text{LiNi}_{1/3}\text{Mn}_{1/3}\text{Co}_{1/3}\text{O}_2$ Cathodes. *Journal of Materials Chemistry* **2012**, *22* (37), 19993–20000.
- (29) Bondue, C. J.; Bawol, P. P.; Abd-El-Latif, A. A.; Reinsberg, P.; Baltruschat, H. Gaining Control over the Mechanism of Oxygen Reduction in Organic Electrolytes: The Effect of Solvent Properties. *Journal of Physical Chemistry C* **2017**, *121* (16), 8864–8872
- (30) Jung, R.; Metzger, M.; Maglia, F.; Stinner, C.; Gasteiger, H. A. Oxygen Release and Its Effect on the Cycling Stability of $\text{LiNi}_x\text{Mn}_y\text{Co}_z\text{O}_2$ (NMC) Cathode Materials for Li-Ion Batteries. *Journal of The Electrochemical Society* **2017**, *164* (7), A1361–A1377.
- (31) Metzger, M.; Strehle, B.; Solchenbach, S.; Gasteiger, H. A. Origin of H_2 Evolution in LIBs: H_2O Reduction vs. Electrolyte Oxidation. *Journal of The Electrochemical Society* **2016**, *163* (5), A798–A809.
- (32) He, Y. B.; Li, B.; Liu, M.; Zhang, C.; Lv, W.; Yang, C.; Li, J.; Du, H.; Zhang, B.; Yang, Q. H.; Kim, J. K.; Kang, F. Gassing in $\text{Li}_4\text{Ti}_5\text{O}_{12}$ -Based Batteries and Its Remedy. *Scientific Reports* **2012**, *2*.
- (33) Reimers, J. N.; Dahn, J. R. Electrochemical and In Situ X-Ray Diffraction Studies of Lithium Intercalation in Li . *Journal of The Electrochemical Society* **1992**, *139* (8), 2091.

- (34) Sathiya, M.; Rousse, G.; Ramesha, K.; Laisa, C. P.; Vezin, H.; Sougrati, M. T.; Doublet, M. L.; Foix, D.; Gonbeau, D.; Walker, W.; Prakash, A. S.; ben Hassine, M.; Dupont, L.; Tarascon, J. M. Reversible Anionic Redox Chemistry in High-Capacity Layered-Oxide Electrodes. *Nature Materials* **2013**, *12* (9), 827–835.
- (35) McCalla, E.; Abakumov, A. M.; Saubanere, M.; Foix, D.; Berg, E. J.; Rousse, G.; Doublet, M.-L.; Dominko, R.; Tara. Visualization Of O-O Peroxo-like Dimers in High-Capacity Layered Oxides for Li-Ion Batteries. *Science* **2015**, *350* (6267), 1516–1522.
- (36) Manthiram, A. A Reflection on Lithium-Ion Battery Cathode Chemistry. *Nature Communications* **2020**, *11* (1), 1–9.
- (37) On-Line Electrochemical Mass Spectrometry Investigations on the Gassing Behavior of $\text{Li}_4\text{Ti}_5\text{O}_{12}$ Electrodes and Its Origins. **2014**.
- (38) Bernhard, R.; Metzger, M.; Gasteiger, H. A. Gas Evolution at Graphite Anodes Depending on Electrolyte Water Content and SEI Quality Studied by On-Line Electrochemical Mass Spectrometry. *Journal of The Electrochemical Society* **2015**, *162* (10), A1984–A1989.
- (39) Bak, S. M.; Nam, K. W.; Chang, W.; Yu, X.; Hu, E.; Hwang, S.; Stach, E. A.; Kim, K. B.; Chung, K. Y.; Yang, X. Q. Correlating Structural Changes and Gas Evolution during the Thermal Decomposition of Charged $\text{Li}_x\text{Ni}_{0.8}\text{Co}_{0.15}\text{Al}_{0.05}\text{O}_2$ Cathode Materials. *Chemistry of Materials* **2013**, *25* (3), 337–351.
- (40) Bernhard, R.; Meini, S.; Gasteiger, H. A. On-Line Electrochemical Mass Spectrometry Investigations on the Gassing Behavior of $\text{Li}_4\text{Ti}_5\text{O}_{12}$ Electrodes and Its Origins. *Journal of The Electrochemical Society* **2014**, *161* (4), A497–A505.

- (41) Sandhya, C. P.; John, B.; Gouri, C. Lithium Titanate as Anode Material for Lithium-Ion Cells: A Review. *Ionics*. 2014, pp 601–620.
- (42) Han, C.; He, Y. B.; Liu, M.; Li, B.; Yang, Q. H.; Wong, C. P.; Kang, F. A Review of Gassing Behavior in Li₄Ti₅O₁₂-Based Lithium Ion Batteries. *Journal of Materials Chemistry A* **2017**, 5 (14), 6368–6381.
- (43) An, S. J.; Li, J.; Daniel, C.; Mohanty, D.; Nagpure, S.; Wood, D. L. The State of Understanding of the Lithium-Ion-Battery Graphite Solid Electrolyte Interphase (SEI) and Its Relationship to Formation Cycling. *Carbon* **2016**, 105, 52–76.
- (44) Hess, M. Temperature-Dependence of the Solid-Electrolyte Interphase Overpotential: Part i. Two Parallel Mechanisms, One Phase Transition. *Journal of the Electrochemical Society* **2018**, 165 (2), A323–A332.

CHAPTER 6.

CONCLUSIONS AND FUTURE OUTLOOK

6-1. Overview

The research presented in this dissertation stresses the importance of utilizing *operando* characterization methods in battery materials research. Monitoring the dynamic electrochemical systems in batteries under their native working environment is crucial to achieving a deeper understanding of their charge storage mechanism and dynamics. The specific projects presented in this dissertation demonstrate the utility of *operando* X-ray techniques for investigating the reaction mechanisms and failure pathways of battery electrodes (Chapter 3) and the interaction(s) between/among the electrode and its protection agents (Chapters 3 and 4). It also illustrates a way to analyze gas evolution from a coin cell with differential electrochemical mass spectrometry employing a new cell design (Chapter 5). In each case, real-time data collection is the key, establishing the connection between reaction mechanism and electrochemistry. Such information and level of detail simply cannot be achieved without the use of *operando* characterization methods.

6-2. Future Research Directions

The rapid expansion of the electric vehicle market has promoted unprecedented growth in battery-related research. In addition to electrode materials with high charge

capacity, the solid-state electrolyte is also heavily studied by scientists as an alternative to traditional organic liquid electrolytes. The superior safety performance of solid-state electrolytes will enable the utilization of lithium metal anodes, which will dramatically increase the charge capacity of the battery. There are two major classes of solid-state electrolytes: lithium-ion conductive polymers and lithium-ion conductive ceramic. The ceramic solid electrolyte has high ionic conductivity, thermal stability, and dendrite suppression capability. However, its high interfacial resistance caused by the poor electrode contact and interfacial reaction with lithium metal hinders the wide application of ceramic electrolytes in batteries. Polymer electrolytes do not have these issues, but their generally low ionic conductivity has precluded their application at room temperature. *Operando* synchrotron X-ray techniques represent excellent tools to investigate the interfacial reaction between the ceramic electrolyte and lithium electrode. The growth of the interface and the corresponding morphology changes can be imaged by *Operando* X-ray tomography, while the structural transformations and strain effects of the ceramic electrolyte can be investigated by operando X-ray diffraction.

On the other hand, the unique features of the coin cell-based DEMS cell enable the study of gas evolution of polymer electrolytes at elevated temperatures, which is not achievable by traditional DEMS measurements.

The results from these operando measurements will provide invaluable insights to drive the further development of solid-state batteries. In addition, it would be great for

fellow students to take advantage of the excellent synchrotron facilities at CHESS and the unique DEMS system in our lab, to investigate the reaction mechanism of solid-state electrolytes and future battery systems